Title

Deciphering Electrochemistry of Li-Excess, Cation-Disordered Rocksalt Cathode Materials

Author

Crafton, Matthew James

Publication Date

2023

Peer reviewed|Thesis/dissertation

Deciphering Electrochemistry of Li-Excess, Cation-Disordered Rocksalt Cathode Materials

By

Matthew J. Crafton

A dissertation submitted in partial satisfaction of the

requirements for the degree of

Doctor of Philosophy

in

Chemical Engineering

in the

Graduate Division

of the

University of California, Berkeley

Committee in charge:

Professor Bryan D. McCloskey, Chair
Professor Nitash Balsara
Professor Gerbrand Ceder

Summer 2023

Deciphering Electrochemistry of Li-Excess, Cation-Disordered Rocksalt Cathode Materials

Abstract

Deciphering Electrochemistry of Li-Excess, Cation-Disordered Rocksalt Cathode Materials

by

Matthew J. Crafton

Doctor of Philosophy in Chemical Engineering

University of California, Berkeley

Professor Bryan D. McCloskey, Chair

The rapid growth in demand for portable energy storage technologies, driven by the proliferation of electric vehicles and portable electronics, has created a tremendous need for low-cost, resource-friendly energy storage technologies with high energy densities. To date, lithium-ion (Li-ion) batteries have been the primary choice for these burgeoning applications, largely due to their favorable energy and power densities. To meet this ever-growing demand, low-cost, high energy density Li-ion batteries constructed from materials with resource-friendly compositions must be developed and mass-produced.

The cost, energy density, and resource footprint of modern commercial Li-ion batteries is largely determined by the electrode materials. Specifically, the layered transition metal oxide cathode that is commonly used in commercial Li-ion batteries comprises a large fraction of the cost, possesses a limiting capacity that significantly constrains the achievable energy density, and often contains scarce and expensive transition metals such as Co and Ni. Furthermore, from a humanitarian perspective, a large fraction of the Co that goes into the global Li-ion battery supply chain is sourced via 'artisinal' mining in the Democratic Republic of Congo, which commonly features horrible working conditions, low wages, and insufficient protection from occupational hazards. As such, there is an urgent need to develop low-cost, high-capacity, resource-friendly cathode materials.

One type of cathode material that has received significant attention in recent years is the lithium-excess, cation-disordered rocksalt (DRX) material. DRX materials are transition metal oxides/oxyfluorides that occupy the same crystal structure as traditional layered transition metal oxide cathode materials. In contrast to the layered materials, in which lithium and transition metals are arranged in alternating layers within the oxide lattice, the cations in DRX materials possess no long-range ordering and instead are distributed throughout the material in a disordered manner. Furthermore, as designated by the term 'Li-excess,' DRX materials contain more than one Li per formula unit. A few key consequences of the cation-disordered nature and Li-excess composition emerge as features which make DRX

materials attractive candidates for next-generation cathode materials. First, due to the lack of the requirement to form any sort of long-range ordering, a wide array of transition metals may be accommodated as electrochemically-active redox centers. This compositional flexibility enables the employment resource-friendly redox couples like $Mn^{3+/4+}$. Second, due to a reshuffling of the electronic structure caused by the broad distribution of local coordination environments, a secondary high-voltage bulk charge compensation process known as oxygen redox is activated. The additional charge compensation provided by oxygen redox allows for delithiation beyond what can be achieved relying on transition metal redox alone, thereby allowing DRX materials to achieve capacities as high as 300 mAh g^{-1}. These two features, compositional flexibility and high capacity, position DRX materials as a unique and promising candidate for the development of low-cost, resource-friendly, high-capacity cathode materials.

Despite these promising advantages, DRX materials suffer from a few key drawbacks that prevent their application in commercial Li-ion batteries. Perhaps the most significant of these drawbacks is high interfacial reactivity. The wide voltage window needed to achieve high capacities from DRX materials requires the electrode to depart the electrolyte stability window, driving extensive electrolyte degradation. This electrolyte degradation leads to depletion of the electrolyte and formation of various degradation products. The formation of these degradation products can cause numerous undesirable processes, including deposition of insulating species on electrode surfaces resulting in a rise in cell impedance, downstream reaction of degradation products with cell components causing additional degradation, and accumulation of gaseous degradation products leading to a rise in pressure within the cell. These deleterious processes lead to significant performance decay and limit the long-term cyclability of cells containing DRX cathodes.

This dissertation explores the bulk electrochemistry and interfacial reactivity that are characteristic of DRX materials during electrochemical cycling. A broad suite of characterization techniques, some traditional and others novel, are employed to obtain insights into the fundamental chemistry that underlies both the initial performance and the long-term stability of cells containing DRX cathodes. Principal among these techniques, gas evolution measurements conducted by differential electrochemical mass spectrometry provide crucial insights into the electrochemical conditions under which and the extent to which interfacial degradation processes occur.

In Chapter 1, the fundamentals of Li-ion batteries are presented. This introduction describes the basic principles of Li-ion batteries as well as the important factors that determine their promise as energy storage devices for use in applications such as electric vehicles and portable electronics. Chapter 2 investigates the effect of fluorine substitution on the bulk redox and interfacial degradation reactions that occur during electrochemical cycling of Mn/Nb-based DRX materials. The results of this investigation demonstrate that adding fluorine to the DRX material shifts the balance between $Mn^{3+/4+}$ and oxygen redox, suppresses oxygen loss, and causes dissolution of fluorine from the DRX surface. Chapter 3 examines the reactivity

of a set of highly fluorinated Mn/Nb-based DRX materials synthesized by high-energy ball milling. It is shown that the degree of fluorination can be used to tune the balance between $Mn^{2+/4+}$ and oxygen redox in these materials. This study also reveals that these materials possess extremely high interfacial reactivity that drives a variety of interfacial degradation processes, including fluorine dissolution and sustained electrolyte degradation that generates CO_2 and electrolyte-soluble acidic species. Chapter 4 explores the effect of voltage window on interfacial degradation and performance decay during cycling of Mn/Ti-based DRX cathodes. This work demonstrates that heightened interfacial degradation brought about by cycling to extreme ends of the voltage window leads to drastic performance decay during extended cycling. Finally, Chapter 5 summarizes the work presented throughout this dissertation and highlights its implications.

Contents

List of Figures

List of Tables

Acknowledgments

First and foremost, I would like to thank my advisor, Professor Bryan McCloskey, for his guidance, insight, and support throughout my time at Berkeley. Thank you, Bryan, for teaching me how to think, work, and conduct myself as a scientist. Your tireless and ever-patient counsel throughout the many challenges I have faced over the last five years has made me into the researcher I am today.

Thank you to Professor Nitash Balsara, Professor Gerbrand Ceder, and Professor Roya Maboudian for serving on my qualifying exam committee. Your insights at a pivotal phase in my academic career provided an invaluable opportunity to evaluate my trajectory. Thank you to Joseph Nolan and Carlet Altamirano for your administrative support and friendly encouragement.

I am grateful to my colleagues in the McCloskey Lab, who have provided a tremendous sense of camaraderie, support, and friendship over the years. Thank you to Sara, Joe, and Lori for mentoring me and laying the foundation on which I have built my work. Yang, thank you especially for being such a tremendous friend and collaborator over the last five years.

Thank you to my collaborators and coauthors, all of whom have have lent their assistance and expertise to help me in my graduate career. Thank you especially to Dr. Wei Tong, Dr. Yuan Yue, Professor Raphaële Clément, Dr. Raynald Giovine, Professor Gerbrand Ceder, and Dr. Zijian Cai - it has really been a privilege to work with you.

I am tremendously grateful to all of the friends that have made my time at Berkeley fun and memorable time. To my friends from before graduate school - Aidan, Ariel, Sam, Nate, Eric - thank you for staying in touch and supporting me through the ups and downs. To my housemates at Edwards House - Zach H., Zach L., Francis, Alec, Josh - thank you for helping form a home with countless fun times.

Finally, thank you to my family. To my older brother Brian - thank you for inspiring me to continue my academic journey at Berkeley. If it weren't for you, I'd never have gone to graduate school. To my parents, thank you for supporting me and giving me everything I could have ever asked for to get to where I am today. Mom, thank you for your endless encouragement and confidence in me. Dad, thank you for teaching me to understand, fix, and build the things around me - I never thought it would prove so useful.

Chapter 1

Introduction to Lithium-Ion Batteries

1.1 Basic Principles of Lithium-Ion Batteries

Lithium-ion (Li-ion) batteries have rapidly emerged in recent years as the predominant form of electrochemical energy storage technology for a wide array of applications, largely owing to their high energy- and power-densities.[1,2] A nominal Li-ion battery consists of an anode and a cathode separated by a Li-ion conducting electrolyte. During electrochemical cycling, Li-ions are shuffled back and forth between the two electrodes through the electrolyte while electrons move through an external circuit to provide charge compensation. By definition, the lithiation/delithiation process at the cathode operates at a higher potential than that at the anode. As such, on charge, lithium ions and electrons are moved from the cathode to the anode, storing energy by moving the charge carriers to a higher energy state. On discharge, lithium ions are moved from the anode to the cathode, releasing the energy stored on charge by allowing the charge carriers to return to a lower energy state.[3,4]

The cathode in modern commercial Li-ion batteries is generally a composite electrode consisting of active material, conductive carbon, binder, and a current collector.[5] The cathode active material, which is generally a layered transition metal oxide like $LiCoO_2$ (LCO) or $LiNi_xMn_yCo_zO_2$ (NMC), is the electrochemically-active component capable of energy storage by means of reversible intercalation of lithium into the oxide lattice. Charge compensation during lithiation/delithiation of these transition metal oxides is achieved by reduction/oxidation of the electrochemcially-active transition metal centers, such as Co and Ni.[6] The conductive carbon provides electrical conductivity to the electrode, allowing electrons to travel from the external circuit to the active material particles.[7] The binder, often poly(vinylidene)fluoride, provides mechanical robustness by maintaining cohesion between the different electrode components.[8] Finally, the current collector, which is typically aluminum foil, distributes the current throughout the footprint of the electrode.[9]

Similarly, the anode in modern commercial Li-ion batteries is generally a composite electrode containing graphite, conductive carbon, binder, and a current collector. Graphite serves as the anode active material, with which energy storage is achieved by reversible lithia-

tion/delithiation of the graphite structure. Charge compensation during lithiation/delithiation is provided by reduction/oxidation of the graphite.[10] The non-active cell components (conductive carbon, binder, current collector) perform the same functions and are mostly comprised of the same materials as those in composite cathodes, with the main difference being that copper foil is typically used as the current collector instead of aluminum foil.[7–9]

The electrolyte in commercial Li-ion batteries consists of lithium hexafluorophosphate ($LiPF_6$) dissolved in a mixture of organic carbonate solvents. The solvent mixture generally consists of the cyclic carbonate ethylene carbonate (EC) and one of several linear carbonates, including dimethyl carbonate (DMC), ethyl methyl carbonate (EMC), and diethyl carbonate (DEC).[11] The $LiPF_6$ salt provides appropriate conductivity and allows Li ions in the electrolyte to be consumed by lithiation of one electrode while they are simultaneously produced by delithiation of the other electrode. Another important feature of this electrolyte is that it possesses a relatively wide electrolyte stability window and forms adequate passivation layers on the surface of low-voltage anode materials like graphite. Specifically, ethylene carbonate is known to reduce at low voltages, evolving ethylene gas and depositing a passivating layer of solid carbonates. This passivation layer subsequently protects the electrode/electrolyte interface from further degradation.[12]

The schematic shown in Figure 1.1 depicts a nominal Li-ion battery as described in the preceding paragraphs. For simplicity, only the active material is shown for each composite electrode, omitting non-active electrode components including conductive carbon, binder, and current collectors. Li-ions are stored between the layers of graphite in the anode and between the layers of metal oxide in the cathode. The corresponding electrochemical reduction/oxidation reactions are included below each electrode. During electrochemcial cycling, oxidation at one electrode is paired with reduction at the other to shuttle Li-ions and electrons back and forth between the electrodes. The Li-ions travel through the ion conducting electrolyte, while the electrons travel through the external circuit. The arrows depict the direction of travel for each charge carrier during the charge/discharge processes.

Perhaps some of the most important metrics for Li-ion batteries are the gravimetric and volumetric energy densities, which determine the amount of energy that can be stored per battery mass and volume, respectively. These two values are especially important for energy storage applications in which the weight and size of the battery are important factors, such as electric vehicles and portable electronics. As shown in Equation 1.1, the energy stored or released by a battery is given by the time integral of the power during charge or discharge, respectively. This expression can be rewritten in a variety of ways using the definitions of terms like power and capacity.[3] The gravimetric and volumetric energy densities can then be obtained by dividing the energy by the battery mass and volume, respectively (Equations 1.2 and 1.3). As can be seen from these formulae, improving the energy density of Li-ion batteries requires an increase in the specific capacity (per weight or volume) or the cell voltage. Given that the cell voltage is relatively constrained by the electrolyte stability window, the most promising way to improve the energy density is by developing electrode

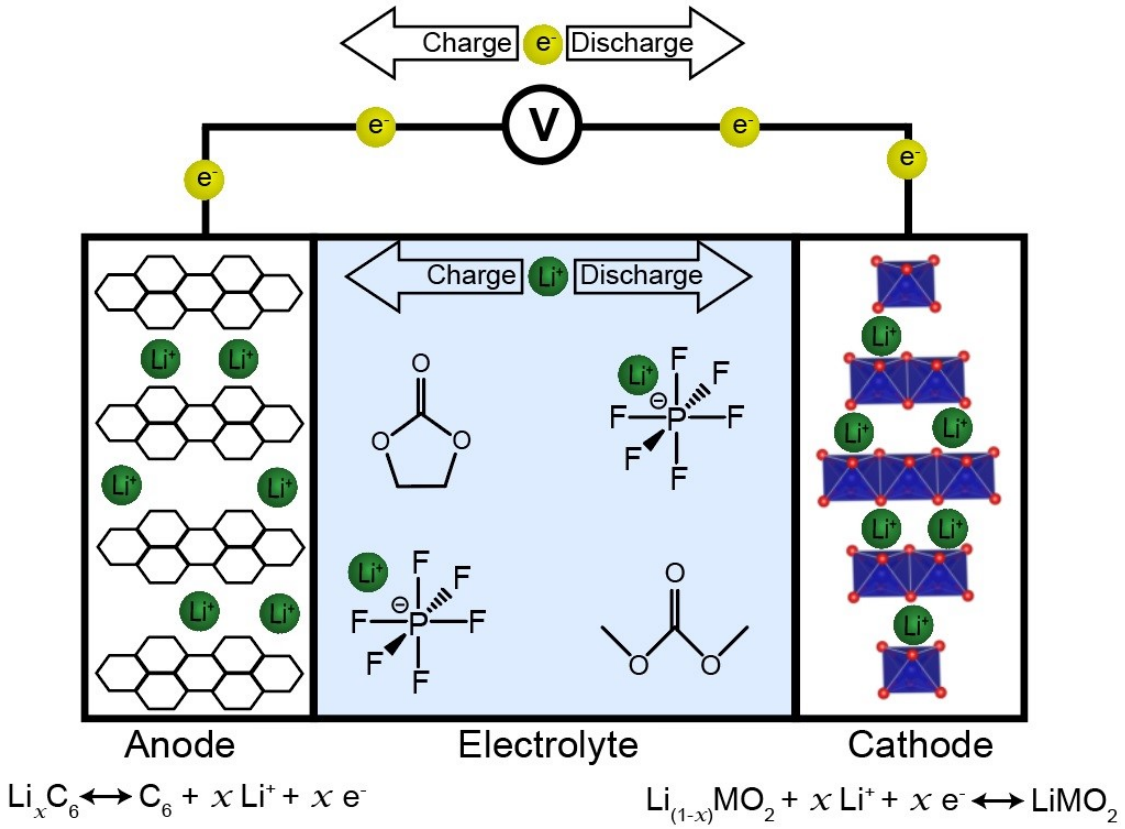

Figure 1.1: Simplified schematic of a Li-ion battery. Graphite anode and lithium transition metal oxide separated by an electrolyte of $LiPF_6$ in a mixture of ethylene carbonate and dimethyl carbonate. Arrows depict the direction of travel for Li-ions through the electrolyte and electrons through the external circuit during charge and discharge.

active materials with greater specific capacities.

$$\text{Energy} = \int_{t_{initial}}^{t_{final}} P(t)dt = \int_{t_{initial}}^{t_{final}} V(t)I(t)dt = \int_0^Q V(q)dq \tag{1.1}$$

$$\text{Gravimetric Energy Density} = \frac{E}{m_{battery}} = \int_0^{Q/m_{battery}} V(q)dq \tag{1.2}$$

$$\text{Volumetric Energy Density} = \frac{E}{v_{battery}} = \int_0^{Q/v_{battery}} V(q)dq \tag{1.3}$$

where P is the power, t is time, $t_{initial}$ is the time at the start of the charge/discharge, t_{final} is the time at the end of the charge/discharge, V is the voltage, I is the current, Q is the total capacity, q is the incremental capacity, and $m_{battery}$ and $v_{battery}$ are the mass and volume of the battery, respectively.

Another crucial factor for the widespread adoption of Li-ion batteries for energy storage applications is the cost. For example, electric vehicles are currently largely constrained to the luxury portion of the vehicle market due to their relatively high cost, which is heavily influenced by the cost of the battery pack.[13,14] As such, along with increasing the specific capacity of electrode active materials to boost the battery energy density, there is a tremendous need to reduce the cost of Li-ion batteries to enable more widespread use in a variety of applications.[15]

1.2 Characteristics and Limitations of Modern Commercial Cathode Materials

The layered lithium transition metal oxides (TMOs) that are used as the active material in modern commercial cathodes possess the general formula $LiMO_2$, where M represents a combination of Ni, Co, Mn, and Al.[4]. These materials possess an α-$NaFeO_2$ structure, in which the cations and anions each occupy interpenetrating face-centered cubic sublattices. Within the cation sublattice, the cations arrange themselves in alternating layers of Li and M.[6] Ni and Co are the predominant electrochemically-active transition metals in these materials, providing charge compensation for TMO (de)lithiation via the $Ni^{2+/4+}$ and $Co^{3+/4+}$ redox couples.[16] During charge, lithium is removed from the oxide lattice while the transition metal redox centers are simultaneously oxidized. Likewise, during discharge, lithium is reinserted into the oxide lattice while the transition metal redox centers are reduced.

The general chemistry that underlies (de)lithiation of layered TMO cathode materials limits the capacity that can be obtained during cycling to just 1 Li per transition metal center. In fact, structural limitations often limit the capacity even further, as excessive depopulation of the Li layer deteriorates the oxide structure.[4,6] Consequently, materials like LCO typically achieve a reversible capacity of no more than 0.6 Li per transition metal center, which usually amounts to roughly 150-200 mAh g^{-1}. This specific capacity is greatly limiting to the attainable energy density of Li-ion batteries, especially given that the capacity of the graphite anode material exceeds 350 mAh g^{-1}.[10]

$Ni^{2+/4+}$ and $Co^{3+/4+}$ remain the only transition metal redox centers that can be used within the class of layered TMO's, as the characteristics (size, charge, electronic structure) of other transition metals (Mn, Fe, etc.) are unsuitable to form the layered structure during material synthesis and maintain it under successive oxidation/reduction.[17,18] While Mn is commonly incorporated into the NMC class of layered TMO's, it remains inactive as Mn^{4+}.[16] The reliance on these two metals, Ni and Co, presents a significant limitation of layered TMO cathode materials from the perspective of cost and resource-abundance. Ni and Co are significantly more expensive and scarce than other transition metals like Fe, Mn, and Ti. Co is particular limiting from this perspective, as it is roughly 10-times more expensive than Ni.[15] Furthermore, the mining of Co is beset with humanitarian issues, as a large portion of Co mining is conducted with unethical labor practices that include low wages, unsafe

working conditions, and child labor.[19] Because of this reliance on Ni and Co, the cost of cathode materials remains one of the primary reasons for the high cost of Li-ion batteries.[20]

1.3 Developing Improved Cathode Materials

Based on the two characteristics outlined in the previous section, low capacity and high cost, the cathode material is the most significant impediment to the development of high energy density, low-cost Li-ion batteries. As such, there is a tremendous need to develop alternative cathode materials with higher capacity and lower cost to circumvent these constraints.

1.3.1 Raising the Capacity

Raising the capacity of Li-ion cathodes requires the development of a material that can provide a higher density of reversible charge compensation to accommodate a greater amount of delithiation. Furthermore, the cathode material structure must remain stable in a highly delithiated and oxidized state. To date, this increase in capacity has primarily been pursued through the development of Li-excess TMOs, which possess the formula $Li_{1+x}M_{1-x}O_2$ (where M represents a combination of transition metals).[21,22] The term 'Li-excess' refers to the increased Li composition ($x > 0$) relative to that of conventional layered TMOs ($x = 0$).

The Li-excess composition raises the achievable capacity by activating a secondary bulk redox process called oxygen redox. Oxygen redox is enabled by the existence of Li-O-Li configurations, which feature two Li-ions bound to an oxygen anion on opposite sides from one another.[23] These Li-O-Li configurations do not exist in conventional layered TMOs without Li-excess composition because the lithium ions are all contained within the Li layer. In the case of Li-excess TMOs, on the other hand, partial occupation of the transition metal layer by Li creates significant quantities of Li-O-Li configurations. This configuration leaves the oxygen 2p orbital pointing in the direction of the Li-ions unhybridized, causing a reshuffling the material electronic structure and the generation of a higher-energy oxygen band that can be reversibly oxidized and reduced.[23] Oxygen redox provides additional bulk charge compensation alongside that which can be provided by transition metal redox, enabling higher capacities in Li-excess TMOs.[22,24]

Despite these advantages, stability at high states of delithiation remains a significant challenge for Li-excess TMOs. In the highly delithiated state associated with the top of charge, the oxygen anions are both partially oxidized and under-coordinated, triggering the full oxidation of the surface oxygen species and the evolution of gaseous O_2 from the TMO surface.[25–28] O_2 evolution leaves behind a densified rocksalt phase that impedes Li transport and cannot be relithiated.[22,29–31] Furthermore, to achieve the high capacities associated highly delithiated TMO cathode materials, Li-excess TMOs are often charged to voltages as high as 4.8 V vs. Li/Li^+.[22,32] Charging to such high potentials takes the cathode outside of the electrolyte stability window, driving oxidative electrolyte degradation at the cathode-electrolyte interface.[27,33,34] This electrolyte degradation can have several deleterious

consequences, including depletion of the electrolyte, deposition of insulating degradation products on the cathode surface, and formation of reactive degradation products.[35–37] The deposition of insulating electrolyte degradation products on the cathode surface is likely to impede Li transport at the cathode-electrolyte interface, raising overpotentials and worsening the energy efficiency and rate capability of the cell.[38–41] Furthermore, the formation of reactive degradation products is likely to initiate secondary degradation processes within the cell, including TMO dissolution, electrolyte hydrolysis, and decomposition of passivating species at the electrode-electrolyte interfaces.[35,42,43] Collectively, these instabilities limit the long-term cycling stability of Li-excess TMOs, necessitating the development of routes towards a more stable cathode-electrolyte interface.

1.3.2 Improving Cathode Material Affordability and Sustainability

Lowering the cost of TMO cathode materials requires a shift away from the use of Ni and Co.[15] Given that layered TMO's are constrained to use of Ni and Co as the only electrochemically-active transition metal centers, this change requires the abandonment of layered TMOs for an alternative cathode material that can accommodate low-cost, resource-friendly transition metal redox centers.[17,18,44] Commercialized, low-cost alternatives to layered TMOs include spinels (ex. $LiMn_2O_4$) and lithium metal phosphates (ex. $LiFePO_4$).[1] By making use of low-cost transition metal redox centers such as Mn and Fe, these materials are much less expensive than traditional layered TMOs.[20,45] Unfortunately, spinels and lithium metal phosphates possess relatively low specific capacities (~ 120 mAh g^{-1} and ~ 140 mAh g^{-1}, respectively) due to their bulky lattices.[4,46]

Lithium-excess, cation-disordered rocksalt (DRX) materials are another alternative class of cathode materials that have received significant attention in recent years.[47] DRX materials possess the same rocksalt structure as layered TMOs but lack the layered ordering of lithium and transition metals. Instead, the cation sublattice of DRX materials possesses no long-range ordering, relieving the requirement to form and maintain a layered structure.[44] Without this constraint, DRX materials can incorporate a large variety of electrochemically-active transition metals.[34,48–51] This compositional flexibility has enabled the formulation of DRX materials employing low-cost, resource-friendly transition metal redox couples like $Mn^{3+/4+}$.[32,34,35,37,52–54]

1.4 Investigating Performance and Reactivity of Li-Excess, Cation-Disordered Rocksalt Materials

DRX materials have emerged as a promising candidate for Li-ion cathode materials owing to their desirable characteristics. Their cation-disordered nature confers a compositional flexibility that allows for the incorporation of low-cost, resource-friendly transition metal

redox centers into the cation sublattice and the incorporation of fluorine into the anion sublattice.[34,35,44,48] Additionally, their Li-excess composition and cation-disordered structure together give rise to a high concentration of Li-O-Li configurations, activating oxygen redox and thereby raising the achievable capacity.[37,44,49,55] Together, these traits make DRX materials a remarkably attractive candidate for next-generation Li-ion cathode materials.

Despite their undeniable promise, the chemistry of DRX materials remains under-explored. The extent and reversibility of the transition metal and oxygen redox processes is clouded by their intermixed and dynamic nature.[32,52,56] This lack of clarity limits the ability of researchers to design materials with the optimal balance between the two processes.

Furthermore, the long-term cycling performance of DRX materials is troubled by parasitic interfacial reactivity. The wide voltage window required to achieve high capacities triggers extensive degradation at the cathode-electrolyte interface.[34,56] The interfacial processes include degradation of the DRX surface, decomposition of native carbonate species leftover from synthesis, and degradation of the electrolyte.[37,49] In addition to directly causing the immediate degradation of the cathode and electrolyte, these degradation processes frequently lead to the formation of reactive degradation products that can drive downstream degradation processes throughout the cell.[35] Over long-term cycling, this reactivity inevitably compromises the performance of cells containing DRX cathodes.[32,52,54] While these degradation processes have been investigated for a variety of DRX materials, the effects of factors such as voltage window, DRX material composition, electrolyte composition, and DRX material processing on interfacial degradation remain undetermined. Understanding the influence of these conditions on interfacial degradation is necessary to engineer a more stable cathode-electrolyte interface, which will be required to improve the long-term cycling performance of DRX materials.

This dissertation focuses on investigating the bulk redox and interfacial degradation processes that occur during cycling of DRX cathode materials. These investigations employ a variety of characterization techniques, making especially heavy use of gas evolution measurements to examine outgassing during electrochemical cycling and aqueous titration of DRX cathodes. The gas evolution measurements conducted during cycling provide valuable *in-situ* information about interfacial degradation processes, while those conducted during aqueous titration provide *ex-situ* measures for the extents to which oxygen redox and solid carbonate formation/decomposition have occurred in cycled DRX cathodes. The gas evolution measurements are further extended to tease out subtle details about more complex processes such as DRX dissolution and electrode crosstalk by making alterations to the experimental cell design, including the addition of electrolyte additives and the substitution of different counter-electrode chemistries. Another central part of this dissertation is the use of long-term cycling experiments employing DRX-graphite full-cells to accurately evaluate the cycling stability of DRX cathodes. These experimental techniques are further complemented by a variety of characterization techniques, including a suite of spectroscopic techniques.

The goal of this dissertation is to provide a detailed analysis of the bulk redox and interfacial reactivity that underlie the initial and long-term performance of DRX materials. The findings documented herein provide information crucial for the design of DRX mate-

rials, electrolytes, and cycling protocols with characteristics beneficial to the performance of DRX-based Li-ion systems. Chapter 2 examines the influence of fluorine substitution on the bulk redox and interfacial degradation processes that occur during cycling of Mn/Nb-based DRX materials. This study demonstrates that fluorination shifts the balance between $Mn^{3+/4+}$ and oxygen redox, suppresses O_2 evolution, and has a negligible effect on electrolyte degradation. Chapter 3 explores the reactivity of a set of highly fluorinated Mn/Nb-based DRX materials synthesized by high-energy ball milling. It is shown that the fluorine content can be used to tune the balance of $Mn^{2+/4+}$ and oxygen redox in these materials. This investigation also reveals that these materials possess extremely high interfacial reactivity resulting in unique modes interfacial degradation, including fluorine dissolution and sustained electrolyte degradation that generates CO_2 and electrolyte-soluble acidic species. Chapter 4 establishes a link between voltage window, interfacial degradation, and performance decay during cycling of Mn/Ti-based DRX cathodes. This work reveals the manner in which interfacial degradation at each end of the voltage window leads to drastic performance decay during extended cycling. Finally, Chapter 5 summarizes the work presented throughout this dissertation and elaborates on its implications.

Chapter 2

Anionic Redox in Cation-Disordered Rocksalt Cathode Materials: The Role of Fluorine Substitution

2.1 Abstract

The demand for high energy-density, mass-producible cathode materials has spurred the exploration of new material structures and compositions. Lithium-excess, cation-disordered rocksalt (DRX) materials are a new class of transition metal oxides that display high capacity and environmentally friendly composition. These materials achieve their high capacities partially through oxygen redox, which leads to oxygen loss and detrimental reactivity with the electrolyte. It has previously been shown that oxygen loss can be suppressed by partial substitution of the lattice oxygen for fluorine, but the explicit mechanism behind this effect remains unknown. In this work, Differential Electrochemical Mass Spectrometry (DEMS) and Titration Mass Spectrometry are used to quantify the primary electrochemical reactions occurring during the first cycle in DRX materials. Comparing a DRX oxide and a DRX oxyfluoride, it is shown that fluorination limits oxygen redox and suppresses oxygen loss. Additionally, DEMS is coupled with fluoride-scavenging to demonstrate that small amounts of fluorine dissolve from DRX oxyfluorides during the first cycle. Finally, these techniques are extended over the first several cycles, demonstrating that CO_2 evolution persists and fluoride dissolution continues to a diminishing extent during the first few cycles. These findings motivate surface modifications to control interfacial reactivity and improve long term cycling.*

*This chapter is largely adapted, with permission from all co-authors, from previously published work in: Crafton et al. *Adv. Energy Mater.* **2020** 10(35), 202001500.

2.2 Introduction

Li-ion batteries are ubiquitous in society, powering electric vehicles and portable electronics everywhere. The global demand for this technology has created a tremendous need for Li-ion batteries that are safe, lightweight, low cost, and sustainable.[57] The energy density and cost of modern Li-ion batteries are determined largely by properties of the electrode materials.[3,15] Specifically, cathode materials possess a limited capacity compared to anode materials and often contain expensive or scarce metals like Co.[4,58] To address these shortcomings, there have been enormous efforts to develop new cathode materials that are high capacity, low cost, and resource friendly.[59,60]

Research in the field of lithium-rich transition metal oxides (TMO's) has led to the development a new class of cation-disordered rocksalt cathode materials.[50,61–63] These materials differ from traditional transition metal oxides in that they do not possess long-range cation ordering, a feature previously thought to be a requirement for lithium mobility. Lee et al. showed, however, that sufficient lithium mobility can be realized in disordered materials with lithium-excess compositions. Whereas lithium transport in layered TMO's occurs along lithium layers, lithium transport in cation-disordered materials occurs through a percolating network of lithium-rich channels.[64] This realization has opened the door for the exploration of lithium-excess, cation-disordered rocksalt (DRX) materials, leading to the formulation of many new cathode materials with promising characteristics.[34,65,66]

In addition to enabling lithium diffusion in cation-disordered materials, lithium-excess compositions can also activate oxygen redox.[23,33,67] This activation occurs because there is more extractable lithium than can be compensated for by oxidation of the transition metal alone. Once the transition metal capacity has been completely exhausted during delithiation, other oxidation sources are needed for delithiation to continue. In the case of many TMO's, this source is the oxygen lattice, where oxygen redox can occur through either reversible and irreversible channels. Reversible oxygen redox occurs by the oxidation of oxide, O_2^{4-}, without the evolution of O_2 gas or reaction with the electrolyte, to some oxidized form, O_2^{n-} ($n<4$).[63,68–70] The exact form of this oxidized species remains unclear, with one potential form including oxygen dimers that are peroxo-like in character (i.e. O_2^{2-}).[33,71,72] Upon relithiation during discharge, the oxidized oxygen lattice reverts back to its fully reduced oxide form if truly reversible. This desirable process adds to the reversible capacity that can be accessed by these materials, making them more promising as future cathode materials. In contrast to its reversible counterpart, irreversible oxygen redox occurs through one of three routes: 1. oxygen gas evolution during lattice oxygen oxidation, O_2,[23,73,74] 2. reaction of peroxo-like oxygen formed during lattice oxygen oxidation with the electrolyte or other cell components, and 3. only partial reduction of oxidized oxygen during discharge after it is formed during charge. These deleterious processes lead to permanent degradation that results in poor capacity retention.[65]

To address the issue of cathode degradation caused by irreversible oxygen redox, researchers have leveraged the compositional flexibility of DRX materials to study the effects of partial fluorination. This strategy has been shown to successfully reduce oxygen evolution

and improve capacity retention in DRX materials.[34,65,66] Despite its effectiveness, little is known about fluorine's interactions in the system. The effect of fluorine on oxygen redox, as well as the analogous stability of fluorine towards anionic redox, remains largely unclear. This knowledge is vital to understanding the role of fluorine in DRX materials and will prove crucial in the design of improved cathode materials.

In this study, we examine the role of fluorination on the anionic reactivity of DRX materials. We use DEMS to monitor and quantify the evolution of oxygen and carbon dioxide to provide information about irreversible oxygen redox and carbonate oxidation, respectively. In addition to these in-situ techniques, we also use TiMS on extracted cathodes to study reversible oxygen redox. This set of techniques allows us to individually study several of the primary electrochemical reactions occurring within DRX materials. We quantify the extent of these electrochemical reactions to estimate the contribution of each reaction towards the total capacity. We combine this analysis with previously published information on transition metal redox in DRX materials, allowing us to fully map redox chemistry in DRX materials. By carrying out this analysis on both a DRX oxide and a DRX oxyfluoride and comparing the results, we are able to examine the effects of fluorination on anionic reactivity.

In addition to studying the effect of fluorination on other redox processes, we also couple DEMS with fluoride-scavenging to examine the stability and reactivity of the lattice fluorine itself. Fluoride-scavenging is a technique whereby an additive that reacts to consume fluoride is added to the cell. In this work, we use the fluoride-scavenging additive tris(trimethylsilyl) phosphate (TMSPa). Bolli et al. showed that the gaseous product of the reaction between TMSPa and fluoride, trimethylsilyl fluoride (Me_3SiF), can be detected by gas evolution measurement techniques such as DEMS and used as a signal for fluoride formation in the electrolyte.[75,76] Using Me_3SiF evolution as a proxy for fluorine dissolution from the cathode into the electrolyte as fluoride, we can thereby monitor and quantify the dissolution of fluorine from the cathode. The in-situ nature of this technique is highly valuable, as it provides information on the electrochemical conditions under which fluorine dissolution from the lattice occurs. Similarly, we use fluoride-scavenging coupled with DEMS to study the effect of DRX materials on $LiPF_6$ degradation, a process that also produces fluoride in the electrolyte.[77–79]

The two materials studied in this work are referred to as LMNO and LMNOF. LMNO is a DRX oxide with molecular formula $Li_{1.2}Mn_{0.6}Nb_{0.2}O$, while LMNOF is a DRX oxyfluoride with molecular formula $Li_{1.2}Mn_{0.625}Nb_{0.175}O_{1.95}F_{0.05}$. As can be seen from their chemical formulae, LMNOF exhibits 2.5% substitution of oxygen for fluorine relative to LMNO. This fluorination has the effect of lowering the average anion valence. To maintain charge neutrality, this change is accompanied by an increase in the ratio of Mn to Nb, which correspondingly lowers the average cation valence. This difference implies that even without considering other effects, fluorination at least affects the stoichiometry of the DRX material. The transition metal redox activity of these materials has been studied previously by Lun et al.[34] The only electrochemically active transition metal redox couple is $Mn^{3+/4+}$, which spans the potential range of 3.0-4.2 V vs. Li/Li^+. This initial process provides a capacity of up to 0.6 mol-Li mol-DRX^{-1} for LMNO and 0.625 mol-Li mol-DRX^{-1} for LMNOF. In contrast to Mn, Nb is

considered inactive in the materials because its oxidation state remains constant during cycling.[34] This inactivity implies that Nb does not strongly impact material behavior, leading us to assume that any differences in behavior between materials are caused by the difference in fluorine composition, and not the accompanying difference in niobium composition. In this study, we focus primarily on the electrochemical processes that occur after the Mn redox reservoir has been exhausted (i.e., at charging potentials greater than 4.2 V).

2.3 Experimental Methods

2.3.1 Synthesis DRX Materials

$Li_{1.2}Mn_{0.6}Nb_{0.2}O_2$ (LMNO) and $Li_{1.2}Mn_{0.625}Nb_{0.175}O_{1.95}F_{0.05}$ (LMNOF) were synthesized using solid-state chemistry methods described in a previous report.[34] Commercially available precursors of lithium carbonate (Li_2CO_3, Sigma), manganese(III) oxide (Mn_2O_3, Sigma), niobium(V) oxide (Nb_2O_5, Sigma), and lithium fluoride (LiF, Sigma) were used for synthesis. Stoichiometric amounts of all chemicals, except 10% Li excess, were thoroughly mixed and annealed at 1000°C for 7 hours under Ar gas. After cooling, the annealed black powders were immediately transferred and stored in an Ar-filled glovebox. The annealed LMNO and LMNOF powders were milled with acetylene black (AB) powder at a weight ratio of 70:20 under Ar to enhance electrical conductivity of the composite electrode. Previous scanning electron microscopy characterization of these materails demonstrated that both materials form powders with a particle size in the range of 100-200 nm, suggesting that LMNO and LMNOF possess similar particle morphologies and specific surface areas.[34]

2.3.2 Electrochemical Cell Preparation

Custom Swagelok cells were used as described previously.[80–82] Li foil was used as the negative electrode. The separator was composed of 1 sheet of quartz microfiber filter paper (QMA, Whatman) on the Li side and 1 sheet of polypropylene (Celgard 2500) on the DRX side. The electrolyte varied depending on the type of experiment. For ordinary DEMS experiments monitoring O_2 and CO_2 evolution, the electrolyte was 1M lithium hexafluorophosphate ($LiPF_6$, Sigma) in 1:1 vol:vol ethylene carbonate (EC, Sigma):diethyl carbonate (DEC, Sigma). For DEMS experiments monitoring fluorine dissolution from the DRX material, the electrolyte was 1M lithium perchlorate ($LiClO_4$, Sigma) in 1:1 vol:vol EC:DEC with 1vol% TMSPa (TCI America). For fluoride-scavenging DEMS experiments monitoring electrolyte degradation, the electrolyte was 1M $LiPF_6$ in 1:1 vol:vol EC:DEC with 1vol% TMSPa. For all DEMS cells, the electrolyte loading was 60 μL cm^{-2}. Cathodes were made using a dry mixing technique, in which LMNO-AB or LMNOF-AB powder was mixed with binder in a mortar and pestle. The resulting mixture was then placed on stainless steel mesh and pressed into place using a steel pin. For all experiments that did not feature fluoride-scavenging, the binder was polytetrafluoroethylene (PTFE, Sigma). For the experiments that did include

fluoride-scavenging, the binder was polyethylene (PE, Sigma). Typical DRX loading in our measurements was 7 mg cm^{-2}, and our electrodes were 1/2 inch in diameter (1.3 cm^2). These quantities yield a TMSPa-to-fluorine molar ratio of 0.63 in an LMNOF cell with 1M $LiClO_4$ and PE binder. Despite this ratio, the highest amount of fluoride formation observed in any experiment was a small fraction of the amount of TMSPa present (∼10%), leading us to conclude that there is an excess of TMSPa in the electrolyte relative to the amount of fluoride available for reaction.

2.3.3 Electrochemical Testing and DEMS Gas Analysis

Hermetically sealed cells were assembled in an Ar atmosphere glovebox and appropriately attached to the DEMS apparatus to avoid air exposure. The cells were cycled on a Bio-Logic VSP-series potentiostat under positive Ar pressure (approximately 1.2 bar). For all experiments, cells were cycled at a current of 0.1 Li hr^{-1} (29.2 mA g-$LMNO^{-1}$, 29.4 mA g-$LMNOF^{-1}$) to cut-off potentials listed with each experiment. In some cases, the cells were then held at the relevant cut-off potential until the current decayed to 10% of its original value, or 0.01 Li hr^{-1}. During these experiments, gas evolution was monitored using a custom-built DEMS apparatus, as described in previous publications.[80–82] Throughout the experiment, the cell headspace was sampled every 10 minutes and any accumulated gases were swept to the mass spectrometer chamber. The apparatus is calibrated for O_2, CO_2, and Me_3SiF in Ar, allowing for the determination of the partial pressures of each analyte. The amount of each gas evolved was then quantified using the volume and temperature of the gas sample.

2.3.4 Cathode Extraction

All extracted cathodes were first charged to their listed cut-off voltage at 0.1 Li hr^{-1} and held at the cut-off until the current decayed to 10% of its original value. After the voltage hold, the cell was then switched to open-circuit to rest for a period of several hours. After resting, the cell was removed from the potentiostat and returned to the glovebox, minimizing air exposure. Once inside the glovebox, the cell was dissembled and the cathode and Celgard were placed in a dry vial. The cathode and Celgard were rinsed three times with DEC and dried under vacuum for several hours. The dried cathodes were then stored in the glovebox until titration.

2.3.5 Carbonate and Peroxo-like Oxygen Titration Mass Spectrometry (TiMS)

For studies of the as-synthesized materials, a small amount of DRX powder was placed in a custom-built, hermetically sealed titration vessel. For cathode titrations, rinsed and dried cathodes were instead placed in the titration vessel. This titration vessel was then connected to the TiMS gas handling system, which is identical to the DEMS gas handling system

described elsewhere.[81] After establishing baseline levels for gases of interest, 1 mL of N_2-sparged 10M H_2SO_4 was injected into the titration vessel through a septum-sealed injection port. The resulting acid-DRX mixture was mixed with a magnetic stir bar. CO_2 is evolved from any solid carbonates present on the material surface, whereas O_2 is evolved if any peroxo-like species are present. The quantification of these gases can be used to quantify the deposited carbonate and lattice oxygen oxidation through well-established stoichiometries, as described previously.[83] Gas samples were taken every 2 minutes until the reaction was completed. Similar to the DEMS instrument, the TiMS instrument is calibrated for O_2 and CO_2 in Ar. We refer to this titration procedure as TiMS, short for titration mass spectrometry.

2.4 Results and Discussion

2.4.1 Comparison of LMNO and LMNOF First Cycle Voltage Profiles

LMNO and LMNOF were both charged to 4.8 V vs. Li/Li^+ and discharged to 1.5 V vs. Li/Li^+ at a current of 0.1 Li hr^{-1}. The first charge and discharge profiles, along with the corresponding dQ dV^{-1} plots, are shown in Figure 2.1. During the first charge, each material exhibited two distinct sloping voltage plateaus separated by a transition period in which the voltage rose more quickly. In the dQ dV^{-1} plot, these plateaus are represented by the two adjacent anodic peaks centered around 3.8 V and 4.4 V. This result suggests that there are two distinct electrochemical processes providing capacity within the different potential ranges. As lithium is removed from each cathode, it is first charge compensated by $Mn^{3+/4+}$ redox.[34] After the Mn redox capacity is exhausted, the electrochemical reaction transitions to lattice oxygen oxidation (as will be conclusively verified later). This understanding allows for the assignment of the low-voltage (3.8 V) process to Mn redox and the high-voltage (4.4 V) process to oxygen redox. As can be seen in Figure 2.1, the low-voltage charge plateau is longer for LMNOF than for LMNO, leading to a larger low-voltage anodic peak in the dQ dV^{-1} plot. This result indicates that the Mn redox process accounts for a larger capacity for LMNOF ($\sim$160 mAh g^{-1}) than for LMNO ($\sim$140 mAh g^{-1}). This difference is consistent with the greater Mn content in LMNOF, relative to LMNO. Likewise, the high-voltage charge plateau corresponding to oxygen redox appears shorter in LMNOF than in LMNO, leading to a smaller high-voltage anodic peak in the dQ dV^{-1} plot. This difference indicates that LMNOF accesses less oxygen redox than LMNO. Therefore, it appears that LMNOF possesses a greater transition metal redox capacity and a lesser oxygen redox capacity, relative to LMNO. As a result, the two materials show very similar first charge capacities, owing to this balance between Mn and oxygen redox. On discharge, the two voltage plateaus are less distinguishable, leading to less resolved cathodic peaks in the dQ dV^{-1} plot. This shift in the positions of the cathodic peaks, relative to those of the corresponding anodic peaks, could be due to differences in the electrochemical kinetics of the two processes as well as any

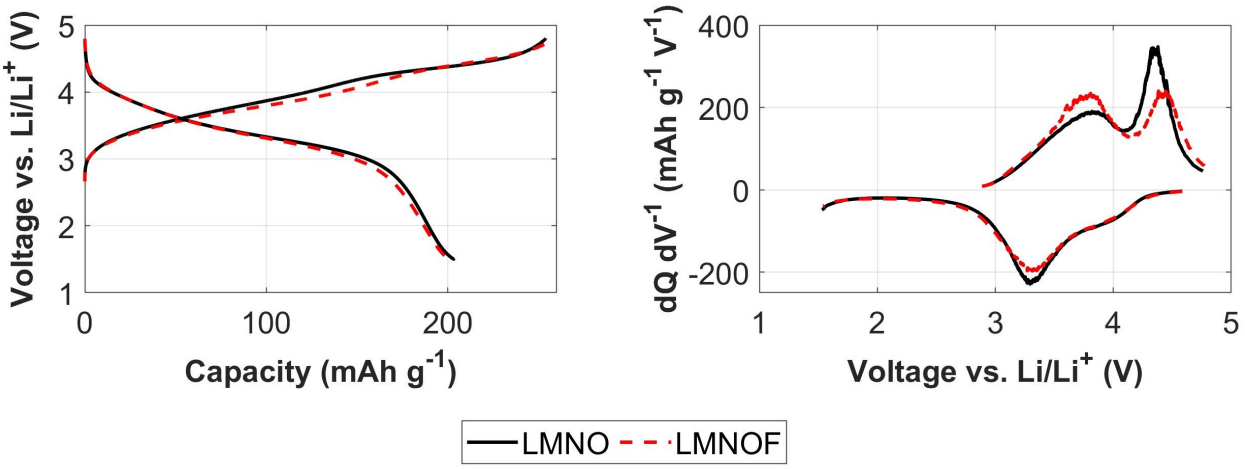

Figure 2.1: Voltage profiles and dQ dV^{-1} plots for LMNO and LMNOF during the first cycle at 0.1 Li hr^{-1} (29.2 mA g-LMNO^{-1}, 29.4 mA g-LMNOF^{-1}).

irreversible changes that occur during the first charge.

2.4.2 First Charge DEMS Comparison of LMNO and LMNOF

To compare gas evolution from LMNO and LMNOF during the first cycle, the two materials were charged to various cut-off potentials and held at the cut-off potential until the current decayed to 0.01 Li hr^{-1}. Meanwhile, O_2 and CO_2 evolution were monitored using DEMS. The cumulative gas evolution quantities for O_2 and CO_2 are listed in Tables 2.1 and 2.2, respectively. Figure 2.2 shows the O_2 evolution rate during charging to 4.4 and 4.8 V vs. Li/Li^+ for both materials. During the charge to 4.4 V, LMNO exhibits a small amount of oxygen loss at the end of charge with an onset potential of 4.4 V. In contrast, LMNOF shows no appreciable oxygen loss when charged to 4.4 V. Given that the capacities of both materials are well into the range expected for lattice oxygen oxidation to occur, these results suggest that fluorination, even in minor quantities, can delay the onset of O_2 evolution. During charging to 4.8 V, O_2 evolution occurs from both LMNO and LMNOF. Both materials begin to evolve O_2 at the end of charge (the onset for O_2 evolution from LMNOF is 4.45 V) as the cell potential approaches 4.8 V, and they continue to evolve O_2 during the voltage hold. It is clear, however, that LMNO evolves significantly more O_2 than LMNOF. This difference suggests fluorine is also successful in reducing the rate of O_2 evolution at higher potentials, which is consistent with previous findings.[34] Clearly, fluorination is successful in suppressing the total amount of oxygen loss and increasing the onset voltage for O_2 evolution in these materials. The CO_2 evolution from these experiments is shown in Figure 2.9 and discussed more in the Supporting Information.

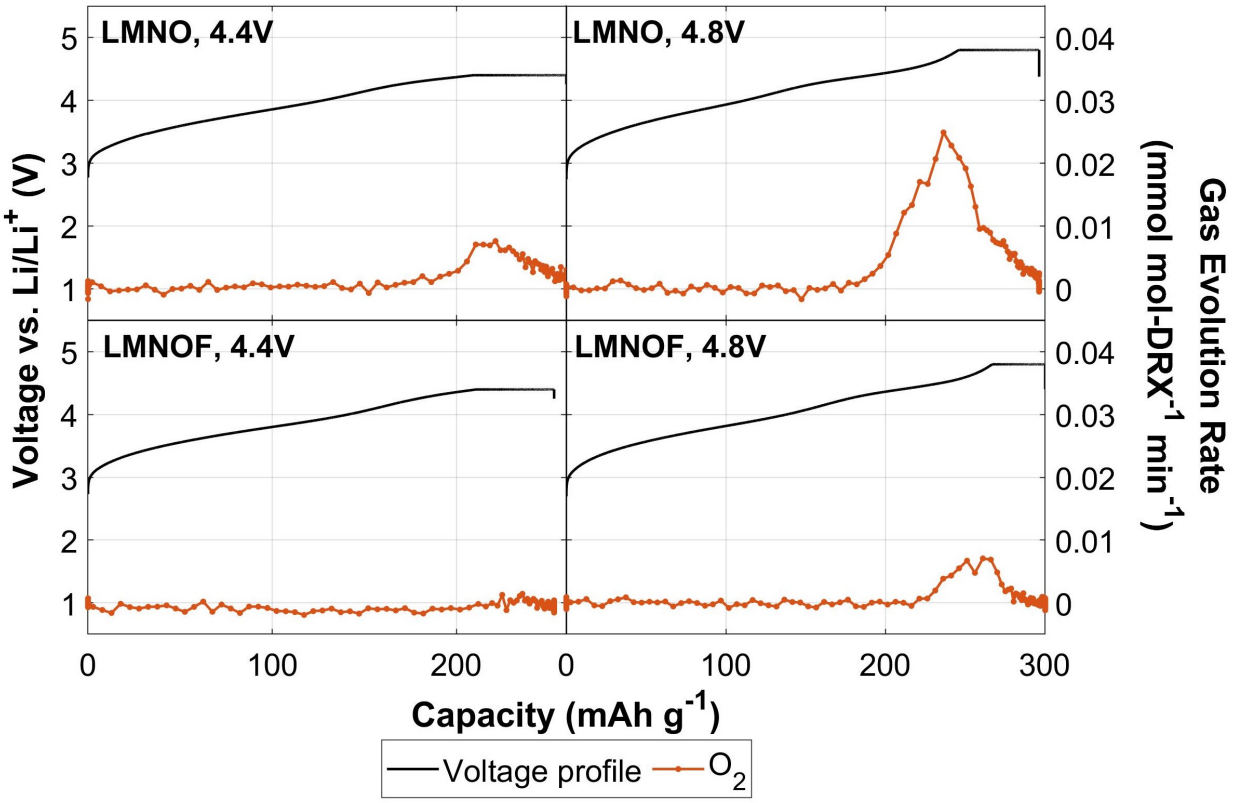

Figure 2.2: O_2 evolution rates from (top) LMNO and (bottom) LMNOF during the first charge to (left) 4.4 and (right) 4.8 V vs. Li/Li^+. Charging consisted of a constant current charge at 0.1 Li hr^{-1} (29.2 mA g-LMNO^{-1}, 29.4 mA g-LMNOF^{-1}) to the listed cut-off voltage followed by a potentiostatic hold at the cut-off voltage until current decayed to 0.01 Li hr^{-1}.

2.4.3 Surface Carbonate Titration on As-Synthesized Material

Lithium carbonate is used as a precursor in the synthesis of DRX materials, leading to small amounts of residual lithium carbonate present on the surface of as-synthesized DRX materials. Previous studies have shown that this residual carbonate can be oxidized during charging, leading to the evolution of CO_2 and singlet oxygen ($^1O_2$), the latter of which can react irreversibly with the electrolyte.[27,84] Another process that leads to CO_2 evolution during charging is oxidation of the carbonate solvents in the electrolyte.[27] To understand how much of the CO_2 observed during charging is due to lithium carbonate oxidation instead of solvent oxidation, it is important to know the total amount of lithium carbonate present on the surface of each DRX material. This value provides an upper limit for the amount of CO_2 that could stem from lithium carbonate oxidation, and it is useful in evaluating the

contribution of each source of CO_2.

To quantify the amount of residual lithium carbonate present on LMNO and LMNOF, samples of each as-synthesized material were analyzed using TiMS as described in the Methods section. The chemistry assumed in the chemical reaction producing CO_2 is provided in Equation 2.1. Because the as-synthesized materials were not exposed to electrolyte, the observed CO_2 must come entirely from residual lithium carbonate. The estimated amounts of residual lithium carbonate present on each material were 23.1 mmol mol-DRX^{-1} for LMNO and 8.1 mmol mol-DRX^{-1} for LMNOF. These values are listed in Table 2.3. Importantly, LMNO has nearly 3 times as much residual lithium carbonate as LMNOF. This information will be used in later sections to understand the relative rates of lithium carbonate oxidation and solvent oxidation.

$$CO^{2-}_{3,\,(s)} + H_2SO_{4,\,(aq)} \rightarrow CO_{2,\,(g)} + H_2O_{(l)} + SO^{2-}_{4,\,(aq)} \tag{2.1}$$

2.4.4 Formation of Peroxo-like Oxygen Species and Deposition of Solid Carbonates During First Charge

During charging, oxygen redox leads to the formation of peroxo-like oxygen species in the bulk of DRX materials. At the same time, electrolyte solvent oxidation and solid carbonate oxidation lead to the deposition and removal of solid carbonates from the surface of DRX materials, respectively.[25,83] Studying the formation of these species provides information about the delithiation charge compensation mechanism and active electrochemistry occurring at high voltages. To measure the amount of peroxo-like oxygen species and surface carbonates produced during the first charge, LMNO and LMNOF cathodes were extracted at different cut-off voltages for acid titration using TiMS. During titration, O_2 and CO_2 evolution were monitored and quantified. The stoichiometry assumed in the chemical reaction producing O_2 is given in Equation 2.2, while the stoichiometry assumed for CO_2 production is given previously in Equation 2.1. Using this information, the amount of peroxo-like oxygen and residual surface carbonate in each cathode was calculated. By studying the amount of these two species in DRX materials after different amounts of cycling, we can obtain information about the progression of oxygen redox and carbonate (both residual lithium carbonate and electrolyte solvent) oxidation.

$$O^{2-}_{2,\,\text{lattice}} + H_2SO_{4,\,(aq)} \rightarrow \frac{1}{2}O_{2,\,(g)} + H_2O_{(l)} + SO^{2-}_{4,\,(aq)} \tag{2.2}$$

The results of the cathode titrations are shown in Figure 2.3. For each material, cathodes were extracted at 4.2, 4.4, 4.6, and 4.8 V vs. Li/Li$^+$. The extraction procedure consisted of a charge at 0.1 Li hr^{-1} to the cut-off voltage followed by a voltage hold at the cut-off voltage until the current decayed to 0.01 Li hr^{-1}. The capacity extracted from each cathode was calculated as the sum of the capacities coming from the constant-current and constant-voltage portions. As can be seen, the 4.6 V extraction for LMNOF achieved a slightly higher capacity than the corresponding 4.8 V extraction. This discrepancy is ascribed to the simple

process variation in cell fabrication, given the small difference in capacity between the two samples (<5%) as well as the fact that there is little capacity between 4.6 V and 4.8 V for LMNOF. Considering first the data from the peroxo-like oxygen titration, it can be seen that the amount of peroxo-like oxygen within both DRX materials grows linearly with capacity throughout the upper charge plateau (>180 mAh g^{-1}). This observation shows that lattice oxygen oxidation occurs at a consistent and significant rate throughout the plateau, supporting the claim that the upper charge plateau corresponds largely to oxygen redox (we will discuss oxygen redox's quantitative contribution to capacity in a later section). Additionally, in the case of the 4.6 V and 4.8 V extractions for LMNOF, the fact that the amount of peroxo-like oxygen trends with capacity and not cut-off voltage suggests that oxygen redox is driven primarily by state-of-charge and not voltage. Looking next at the carbonate titration results, the carbonate content in the LMNO increases with increasing cut-off voltage up to 4.6 V, and the total carbonate deposited at this point, 45 mmol mol-$LMNO^{-1}$, is roughly twice the amount of residual lithium carbonate found in the as-synthesized LMNO powder (23.1 mmol mol-$LMNO^{-1}$, Table 2.3). This indicates that electrolyte degradation at high voltages (>4.2 V) results in surface carbonate formation on LMNO cathodes. For LMNOF, no increase in surface carbonate is observed as a function of cut-off voltage. However, the total carbonate deposited on extracted LMNOF cathodes, roughly 30 mmol mol-$LMNOF^{-1}$, is substantially greater than the amount of lithium carbonate contained in the as-synthesized LMNOF powder (8.1 mmol mol-$LMNOF^{-1}$, Table 2.3). This result indicates that electrolyte degradation results in surface carbonate deposition at voltages lower than 4.2 V on LMNOF cathodes. The surface carbonate on both LMNO and LMNOF appears to either plateau or slightly decrease above 4.6 V, where CO_2 evolution is its highest (Figure 2.9). These results suggest that the mechanism for electrolyte degradation involves solid carbonate deposition and oxidation to evolve CO_2. Similarly to oxygen redox, we will consider in a later section the total contribution of electrolyte degradation to electrochemical capacity.

2.4.5 Fluorine Dissolution from DRX Materials and Electrolyte Salt Degradation During First Cycle

Fluoride-scavenging coupled with DEMS allows us to study fluorine dissolution from the DRX material, or fluoride ion formation from the degradation of other cell components (e.g., the salt anion and the binder). The scavenging additive (TMSPa) reacts with fluoride in the electrolyte to form gaseous Me_3SiF, which then evolves from the cell and can be detected in-situ using DEMS. The use of this technique to study formation of fluoride from a specific source is complicated, however, by the numerous sources of fluoride in the cell, including the aforementioned salt anion and cathode binder. Fluoride formed from any of these components will lead to the evolution of Me_3SiF, preventing us from studying fluoride formation from any single component.

To study the dissolution of fluorine from DRX materials exclusively, all other fluoride-forming components must be eliminated from the cell, prompting us to study cells that

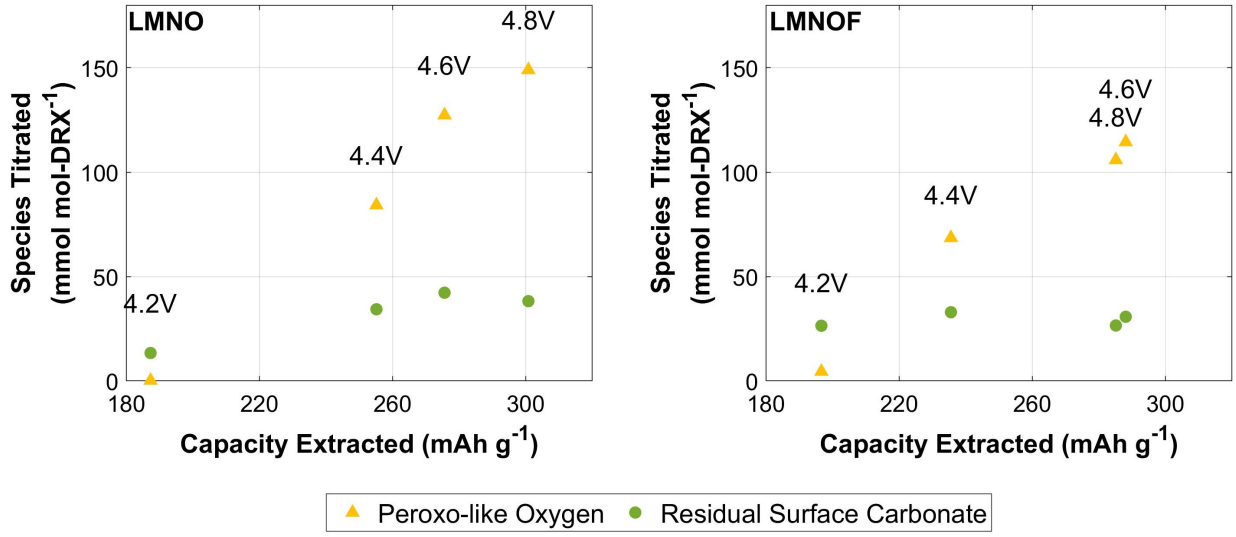

Figure 2.3: Amounts of peroxo-like oxygen and surface carbonate in DRX materials during first charge as measured using TiMS. Cathodes were charged to the labelled cut-off potentials at 0.1 Li hr^{-1} and held at the cut-off potential until the current decayed to 0.01 Li hr^{-1}. The extracted capacity is the sum of the capacities from the constant-current charge and the voltage hold.

employed $LiClO_4$ as the salt and polyethylene as the binder. Additionally, 1 vol% TMSPa was added to the electrolyte. LMNO and LMNOF were charged to 4.8 V vs. Li/Li^+ and discharged to 1.5 V vs. Li/Li^+ on DEMS in cells with these new salt and binder compositions. The cell containing LMNO has no sources of fluoride in the electrodes and electrolyte, meaning there should be no electrochemically-dependent Me_3SiF evolution. In the cell containing LMNOF, however, the only source of fluoride is the cathode active material, meaning any Me_3SiF evolved during charging has to originate from fluorine dissolution from LMNOF.

The evolution profiles of Me_3SiF for the two materials are shown with the corresponding voltage profiles in the top panel of Figure 2.4. Both gas evolution profiles display a sloping baseline, which we ascribe to gas evolution from the reaction of TMSPa with trace amounts of residual fluoride present in the cell from the fluorinated polymer O-rings used for hermetic seals. LMNOF also shows a small peak in Me_3SiF evolution commencing at the end of charge, indicating formation of fluoride in the electrolyte. In contrast, because LMNO contains no fluorine, there is no Me_3SiF evolution resulting from voltage-dependent fluorine dissolution. This data suggests that the fluorine in LMNOF is partially unstable at high voltages, leading to the dissolution of fluorine from LMNOF into the electrolyte as fluoride. The cell potential corresponding to the onset of fluorine dissolution in LMNOF is difficult to precisely identify due to the drifting Me_3SiF baseline, but it appears to begin somewhere around 4.0-4.3 V.

Furthermore, integrating the entire Me_3SiF evolution profile yields a total of 0.7 mmol-Me_3SiF mol-LMNOF^{-1}, which includes any Me_3SiF evolved due to the presumed reaction with the O-rings. Even with this overestimation, the amount of Me_3SiF evolved corresponds to <1% of the fluorine in the LMNOF cathodes. From this analysis, we can conclude that fluorine dissolution affects only a minuscule fraction of the fluorine in the system. Based on the scale of the reaction, we can further conclude that fluorine dissolution does not contribute to the cathode's capacity in any significant way.

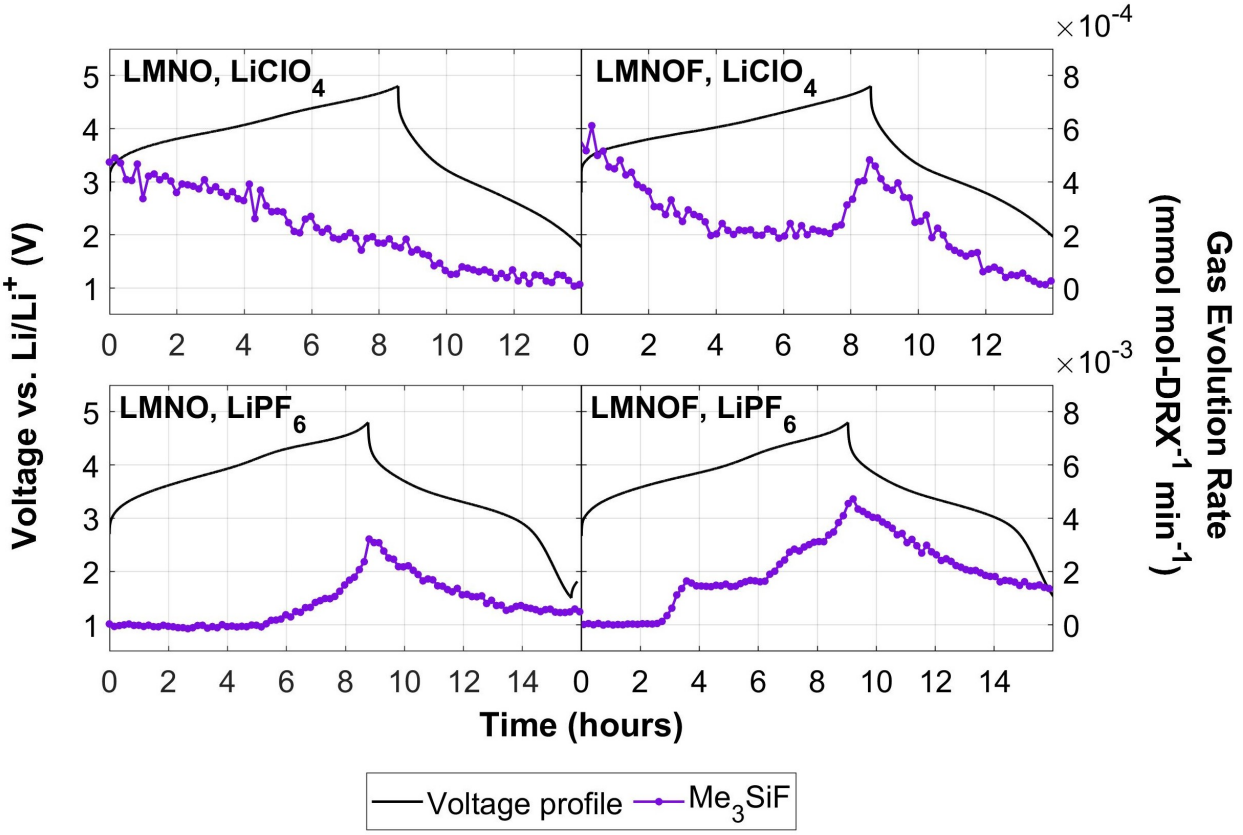

Figure 2.4: Me_3SiF evolution from LMNO and LMNOF in (top panel) 1M $LiClO_4$ in EC:DEC and (bottom panel) 1M $LiPF_6$ in EC:DEC. All cathodes were charged to 4.8 V vs. Li/Li$^+$ and discharged to 1.5 V vs. Li/Li$^+$ at a rate of 0.1 Li hr^{-1} (29.2 mA g-LMNO^{-1}, 29.4 mA g-LMNOF)$^{-1}$ and contained polyethylene as the cathode binder.

While we conclude from the previous experiments that fluorine dissolves from LMNOF into the electrolyte as fluoride during cycling, the effect of this fluoride in a cell containing $LiPF_6$ is unclear. $LiPF_6$ also commonly degrades to form fluorides such as LiF and HF, so the additional fluoride formed from LMNOF could potentially be insignificant in comparison to

the electrolyte-originating fluoride.[75,77,79,85] To study the effect of cathode fluorination on fluoride ion formation in a cell containing $LiPF_6$, we also conducted fluoride-scavenging DEMS in cells containing $LiPF_6$ electrolyte and polyethylene bound cathodes. Now using Me_3SiF evolution as a proxy for fluoride formation from either fluorine dissolution from LMNOF or degradation of $LiPF_6$, we are able to study fluoride formation in another setting. One caveat is that this technique cannot differentiate between cathode-originating fluoride and electrolyte-originating fluoride. These two sources must both be considered when evaluating the role of cathode-originating fluoride on electrolyte degradation.

The Me_3SiF evolution profiles and corresponding voltage profiles for LMNO and LMNOF with $LiPF_6$ as the electrolyte are shown in the bottom panel of Figure 2.4. As can be seen by comparing the scales of the vertical axes in the top and bottom panels of Figure 2.4, both materials display vastly increased amounts of Me_3SiF evolution with $LiPF_6$ (bottom panel) when compared to the analogous experiment with $LiClO_4$ as the electrolyte (top panel). As a result, the sloping baseline due to reaction of TMSPa with the cell O-rings becomes insignificant. The drastic difference in Me_3SiF evolution between the two electrolytes suggests that the majority of the F^- formed in $LiPF_6$ comes from electrolyte degradation, while the amount dissolved from LMNOF is significantly smaller.

Even with the majority of the fluoride coming from $LiPF_6$, LMNOF still displays significantly increased Me_3SiF evolution compared to LMNO. The Me_3SiF evolution profile for LMNO shows a single peak with an onset at 4.2 V and a maximum at the cut-off potential. In contrast, the Me_3SiF evolution profile for LMNOF displays an extended plateau between 3.8 and 4.2 V followed by a large peak at the cut-off potential. Additionally, the rate of Me_3SiF evolution from LMNOF is consistently higher than the rate of Me_3SiF evolution from LMNO. The differences between LMNO and LMNOF can be used to understand the effect of cathode fluorination on $LiPF_6$ degradation.

Based on the extended plateau of Me_3SiF evolution observed from LMNOF in the bottom panel of Figure 2.4, it is clear that fluoride formation begins earlier during cycling of LMNOF than LMNO. As concluded earlier, the primary source of this fluoride must be the electrolyte. This plateau of Me_3SiF evolution therefore suggests that the fluorine present in LMNOF initiates $LiPF_6$ degradation earlier in cycling than in LMNO. Another difference in the Me_3SiF evolution behavior from the two materials is the overall rate of Me_3SiF evolution later during cycling. Past the onset of Me_3SiF evolution in both materials, LMNOF consistently displays higher rates of Me_3SiF evolution than LMNO. This increased rate is more than can be accounted for by fluorine dissolution from LMNOF, suggesting that the fluorine in LMNOF also accelerates $LiPF_6$ degradation after the onset potential.

These findings suggest that the fluorine present in LMNOF both initiates and accelerates the degradation of $LiPF_6$ to form fluoride species. One possible explanation for this result is that small amounts of fluorine dissolved from LMNOF as fluoride have an autocatalytic effect, allowing them to greatly accelerate the degradation of $LiPF_6$. Fluoride species like HF have been shown to increase the degradation of $LiPF_6$.[75,79] This reaction leads to the formation of more fluoride species, thereby accelerating itself in an autocatalytic loop. Through this mechanism, an initially small amount of fluoride dissolved from the cathode

could therefore greatly increase the extent of electrolyte degradation in the cell. Another possible explanation is that the surface of LMNOF is more catalytically active towards $LiPF_6$ than that of LMNO. This enhanced activity would also allow for earlier onset and increased rate of $LiPF_6$ degradation. These results suggest that mitigation strategies to eliminate all fluorine-dissolution from DRX oxyfluoride materials through surface modification may dramatically improve long term cyclability.

2.4.6 First Charge Capacity Accounting

To map the redox chemistry occurring within DRX materials, we now account for the full capacity extracted from LMNO and LMNOF during the first charge by combining results from the suite of characterization techniques discussed herein. This analysis allows for the decoupling of the primary electrochemical processes: transition metal redox, carbonate oxidation, oxygen redox, and oxygen loss. By quantifying each of these, we can estimate the contribution of each type of oxidation to the total capacity observed upon charging. Comparing the results of this analysis for LMNO and LMNOF provides valuable information about the effect of fluorine on DRX electrochemistry.

During delithiation, it was assumed that both materials first undergo complete transition metal oxidation. This assumption is supported by previous studies on LMNO and LMNOF by Lun et al., which used X-ray Absorption Near Edge Structure (XANES) to show that the Mn oxidation state changes during the extraction of the first 0.7 mol-Li mol-DRX^{-1} during charging and remains constant afterwards.[34] Accordingly, the point of complete transition metal oxidation was chosen as a starting point for cathode extractions to quantify lattice oxygen oxidation and carbonate oxidation. The cathode titrations shown previously featured cathodes that were charged to 4.2, 4.4, 4.6, and 4.8 V vs. Li/Li^+, all of which were delithiated close to or past this starting point. Based on this information, we assume that they all underwent complete transition metal oxidation and use the data obtained from outgassing and titrations discussed in the sections above to account for the additional observed capacity.

During charging on DEMS, the evolution of O_2 and CO_2 from each cathode was measured and quantified. The total amounts of O_2 and CO_2 evolved were used to calculate the partial capacities related to irreversible oxygen redox and carbonate oxidation, respectively. For this analysis, O_2 evolution is expected to arise from complete oxidation of the lattice oxide, as shown in Equation 2.3. CO_2, on the other hand, is expected to originate from electrochemical oxidation of carbonate (residual surface carbonate or electrolyte solvent), yielding CO_2 and singlet oxygen. This reaction, as described in Equation 2.4, has previously been studied using isotopic tags and chemical probes.[27,84]

$$O^{4-}_{2,\,(\text{lattice})} \rightarrow O_{2,\,(g)} + 4e^- \tag{2.3}$$

$$CO^{2-}_{3,\,(s)} \rightarrow CO_{2,\,(g)} + \frac{1}{2}\,{}^1O_2 + 2e^- \tag{2.4}$$

Next, the extracted cathodes were analyzed using TiMS as discussed previously. The total oxygen evolved during each titration was used to determine the amount of the amount of peroxo-like oxygen dimers present in the material (shown earlier in Figure 2.3), which in turn was used to determine the partial capacity owing to reversible oxygen redox.[83] The oxidation stoichiometry leading to the formation of peroxo-like oxygen is shown in Equation 2.5, and the accompanying titration chemistry is given earlier in Equation 2.2.

$$O^{4-}_{2,\,(\text{lattice})} \rightarrow O^{2-}_{2,\,(\text{lattice})} + 2e^- \tag{2.5}$$

For each cathode studied, the partial capacities corresponding to Mn redox, carbonate oxidation, reversible oxygen redox, and irreversible oxygen redox were summed to calculate the accounted capacity. If the assumptions made in this analysis are accurate, the accounted capacity should agree with the observed capacity for each cathode. The capacity accounting graphs for LMNO and LMNOF are shown in Figure 2.5. As can be seen for each graph, the capacity accounted from the suite of characterization techniques matches well with the observed electrochemical capacity. This agreement supports the stoichiometry as well as the general reaction scheme used to understand the primary electrochemical reactions.

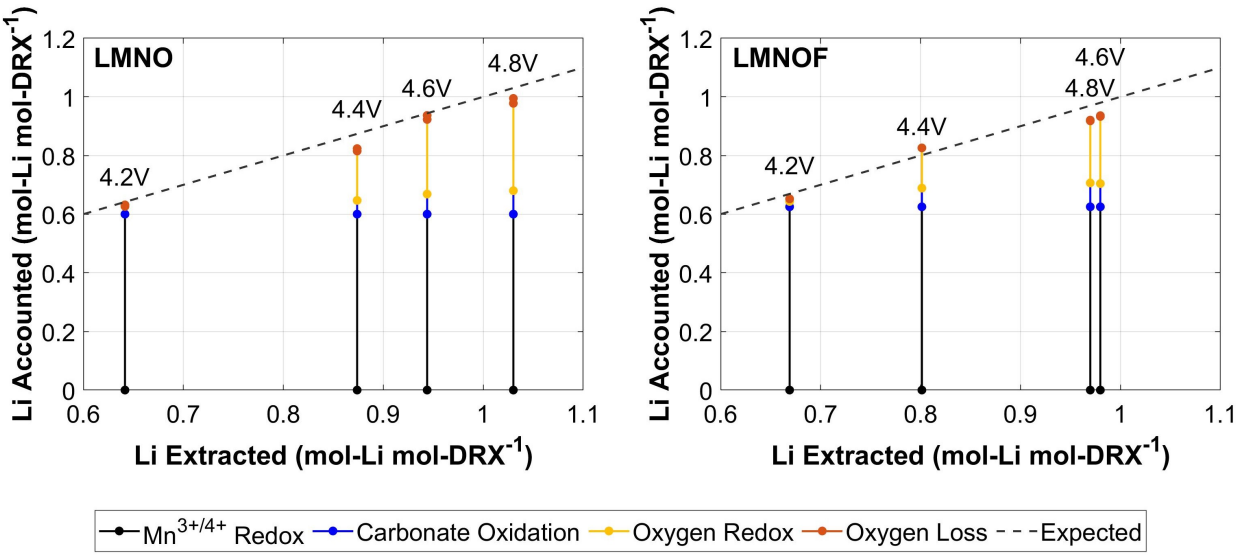

Figure 2.5: Capacity accounting for LMNO and LMNOF cathodes. The results in prior sections are used here to quantitatively assign total capacity to different electrochemical processes. Given that titrations to quantify oxygen redox were performed only at 4.2, 4.4, 4.6, and 4.8 V vs. Li/Li^+, capacity assignments are only made at these voltages. Segments are plotted in the order given in the legend.

Comparing the partial capacities of each primary electrochemical reaction across materials can provide insight into the effect of fluorination on DRX electrochemistry. Based on the assumptions relating to transition metal redox, we conclude that LMNOF undergoes slightly more transition metal oxidation than LMNO owing only to its greater Mn content. Next, we observe that carbonate oxidation accounts for similar amounts of capacity in both materials, although a relatively minor fraction of the total capacity. In contrast to the similar levels of carbonate oxidation, we notice that the amount of reversible oxygen redox differs significantly for the two materials. The capacity contributed from reversible oxygen redox is 0.30 mol-Li mol-DRX^{-1} for LMNO, while it is only 0.23 mol-Li mol-DRX^{-1} for LMNOF. From this, we conclude that LMNOF exhibits less reversible oxygen redox than LMNO, suggesting that fluorination suppresses the total accessible reversible oxygen redox. Finally, comparing the extents of oxygen loss in the two materials, we note that the capacity contributed by oxygen loss is smaller for LMNOF than for LMNO as is shown in the DEMS results in previous sections. In each case, oxygen loss accounts for a very minor fraction of the total capacity.

In considering the differences between LMNO and LMNOF, fluorination of DRX materials clearly has two important and competing effects on material capacity. First, fluorination lowers the average anion valence, which requires an increase in Mn content to correspondingly lower the average cation valence. This shift increases the capacity available from transition metal redox in LMNOF compared to LMNO. In addition, fluorination appears to directly lower the amount of accessible oxygen redox. These two effects nearly offset each other, causing LMNOF to display a capacity similar to that of LMNO. In other words, the fluorination appears to shift the balance between transition metal and oxygen redox without strongly affecting the total charge capacity. Furthermore, the ability of fluorination to shift the balance between the primary redox processes indicates that the fluorine is successfully incorporated into the bulk of the material.

This insight can also be extended to understand the effect of fluorination on oxygen evolution from DRX materials. If fluorination promotes transition metal redox and mitigates reversible oxygen redox, then LMNOF should rely less on oxygen redox to reach a high state of charge compared to LMNO. Consequently, LMNOF undergoes less irreversible oxygen redox than LMNO. This effect could explain the role of fluorination in suppressing oxygen loss and improving capacity retention.

One potential explanation for the effects of fluorination is that it influences the thermodynamics associated with oxygen redox, limiting the amount of oxygen redox accessible below 4.8 V. Another explanation could be that fluorine reduces lithium mobility in DRX materials, requiring higher overpotentials to extract the lithium that is extracted through oxygen redox charge compensation. In either case, fluorination would shift a portion of the oxygen redox reservoir above 4.8 V, thereby reducing both accessible oxygen redox and oxygen loss.

2.4.7 Multiple Cycle DEMS Comparison of LMNO and LMNOF

While it is clear that fluorination suppresses oxygen loss on the first cycle, little is known about oxygen loss on subsequent cycles in DRX materials. Additionally, the extent of carbonate oxidation from DRX materials over multiple cycles has not been studied. To provide information about these processes, LMNO and LMNOF were studied on DEMS for four full cycles at a rate of 0.1 Li hr^{-1}. This four-cycle DEMS experiment was conducted for each material at two different charging cut-off voltages: 4.45 and 4.8 V vs. Li/Li^+, with 4.45 V being selected due to it corresponding to the onset of O_2 evolution for the LMNOF material. Figure 2.6 shows gas evolution profiles and voltage profiles for the two materials when cycled to both cut-off voltages. The cycle-to-cycle gas evolution quantities for each experiment are given in Table 2.4.

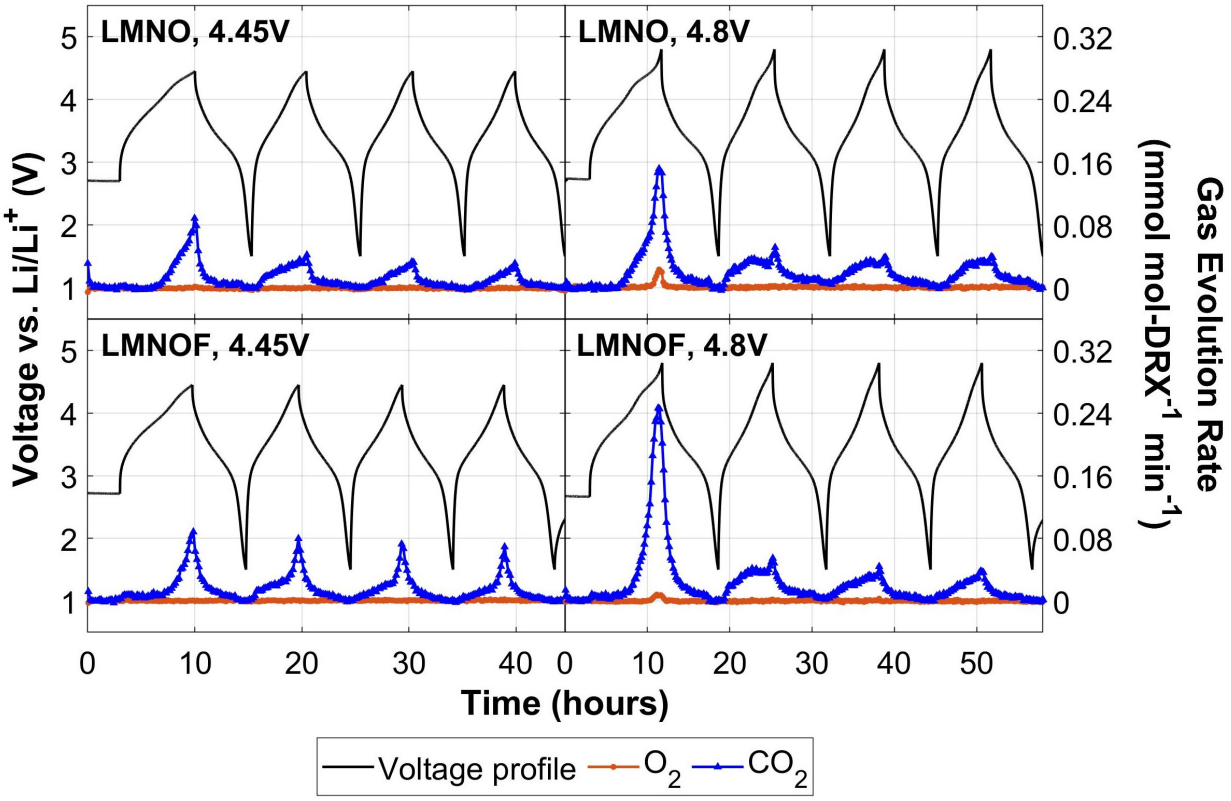

Figure 2.6: O_2 and CO_2 evolution from (top) LMNO and (bottom) LMNOF over the first four cycles with charging cut-off voltages of (left) 4.45 and (right) 4.8 V vs. Li/Li^+. Cycling consisted of charging to the listed cut-off voltage and discharging to 1.5 V vs. Li/Li^+ at a constant current of 0.1 Li hr^{-1} (29.2 mA g-$LMNO^{-1}$, 29.4 mA g-$LMNOF^{-1}$).

In the 4.45 V cut-off experiment, neither material evolves any O_2 throughout all four cycles. The discrepancy between the lack of O_2 evolution here and the O_2 evolution observed in Figure 2.2 is ascribed to the lack of a voltage-hold step in Figure 2.6. Despite this variability, these results suggest that irreversible O_2 evolution can be controlled when the cell potential is kept below 4.45 V for each material.

In the 4.8 V cut-off experiment, both materials evolve a small amount of O_2 on the first cycle and none on subsequent cycles. The amounts of O_2 evolved from the two materials during the first cycle are consistent with the amounts evolved during the constant current portion of the charges shown in the Figure 2.2 measurements. While it does not tell us about other aforementioned irreversible processes associated with oxygen redox, the lack of oxygen evolution on subsequent cycles does indicate that irreversible oxygen loss occurs only on the first cycle. Because gas evolution occurs from the surface, it is likely that an oxygen-depleted region forms close to the surface of DRX materials. This region would serve to passivate the cathode from further oxygen loss, explaining the lack of O_2 evolution on subsequent cycles.

Carbon dioxide evolution is a parasitic process that can originate either from the oxidation of residual lithium carbonate or the electrolyte solvents: ethylene carbonate and diethyl carbonate.[27,84] Given that lithium carbonate would oxidize to form a stoichiometric equivalent of CO_2, the lithium carbonate quantities presented in Table 2.3 represent the upper limit of CO_2 evolution anticipated from oxidation of residual lithium carbonate. Of note, LMNO has nearly three times as much residual lithium carbonate as LMNOF, such that LMNO would be expected to display more CO_2 evolution if Li_2CO_3 oxidation solely accounted for CO_2 evolved during cycling.

However, in the 4.45 V experiment, LMNO and LMNOF display similar CO_2 evolution profiles on the first cycle. Furthermore, over all four cycles, more CO_2 is evolved than can be accounted for by residual lithium carbonate for both materials. For example, the total CO_2 evolved from LMNOF over 4 cycles is 39.2 mmol mol-DRX^{-1}, whereas the residual lithium carbonate contained in the LMNOF powder is only 8.1 mmol mol-DRX^{-1}. These results indicate that a large fraction of the CO_2 is evolved from electrolyte degradation. In fact, the similarity in CO_2 evolution from LMNO and LMNOF, despite the difference in residual lithium carbonate, suggests that the majority of the CO_2 comes from oxidation of the electrolyte solvent. On subsequent cycles to 4.45 V, CO_2 evolution from LMNO attenuates at a faster rate than from LMNOF. The greater rate and slower attenuation of CO_2 evolution from LMNOF, relative to LMNO, may be caused by some degradation process involving fluorine at the surface of DRX materials.

As expected, both materials display significantly increased CO_2 evolution when charged to 4.8 V compared to 4.45 V. LMNOF displays significantly higher CO_2 evolution than LMNO on the first cycle, and much more than can be accounted for by residual lithium carbonate oxidation. As suggested for the 4.45 V experiment, the increased rate of CO_2 evolution from LMNOF relative to LMNO may be driven by some process involving fluorine near the surface of the DRX material. On subsequent cycles, the CO_2 evolution attenuates for both materials, although continues to evolve at non-zero quantities. This sustained CO_2 evolution suggests that electrolyte degradation continues to occur over multiple cycles, posing

an issue for long term cell stability. Surface passivation strategies like rinsing or coating may represent a useful means of suppressing this sustained electrolyte degradation.

2.4.8 Formation of Peroxo-like Oxygen Species and Deposition of Solid Carbonate Over Multiple Cycles

Cathode titrations were also used to study oxygen redox and residual surface carbonate over multiple cycles between 4.8 and 1.5 V vs. Li/Li^+ at 0.1 Li hr^{-1}. Figure 2.7 shows the titration data from LMNO and LMNOF cathodes extracted at the end of the first charge, first discharge, fourth charge, and fourth discharge. For comparison, the titration data for the as-synthesized materials are also included.

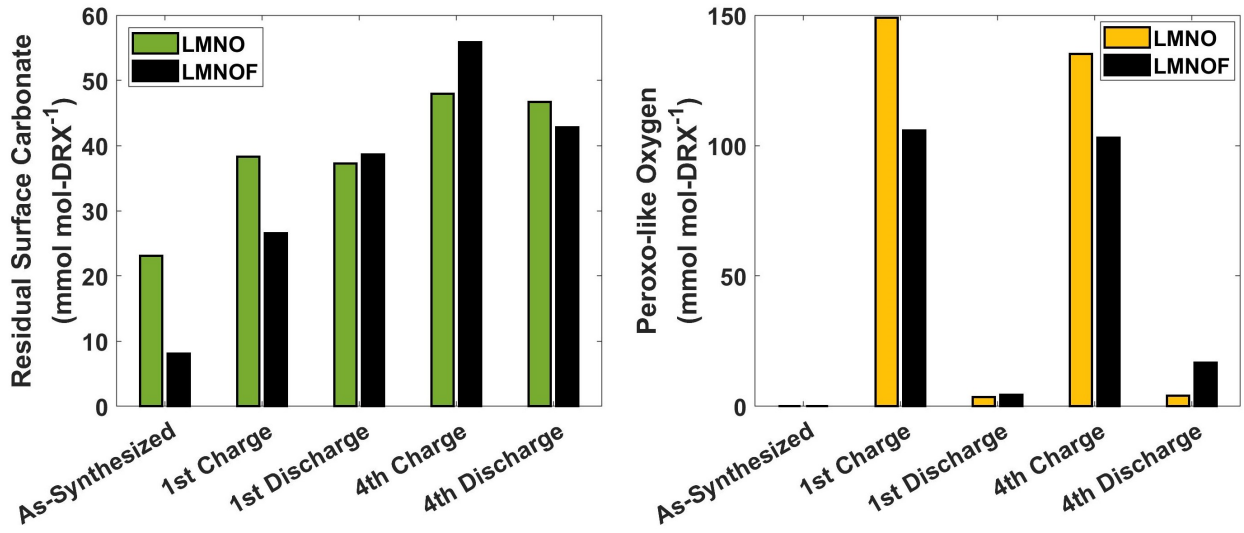

Figure 2.7: Amounts of residual surface carbonate (left) and peroxo-like oxygen (right) in DRX materials through four cycles as measured using TiMS. To acquire the first charge data, a constant current charge to 4.8 V vs. Li/Li^+ at 0.1 Li hr^{-1} was performed, followed by a voltage hold at 4.8 V until the current decayed to 0.01 Li hr^{-1}. The remaining data points were acquired using cathodes only charged/discharged at 0.1 Li hr^{-1} without additional voltage holds.

As shown by the carbonate titration results in Figure 2.7 (left), the amount of surface carbonate generally increases, with some fluctuations, throughout the first four cycles for both materials. This trend is consistent with that observed during the first charge, where electrolyte degradation results in an ever-increasing deposition of solid carbonates on the electrode surface. The peroxo-like oxygen titration data, also shown in Figure 2.7 (right), provides valuable information about the reversibility of oxygen redox in LMNO and LMNOF.

After the first charge, both LMNO and LMNOF possess a large amount of peroxo-like oxygen. After the subsequent discharge, the amount of peroxo-like oxygen decreases nearly to zero in each material. This finding is consistent with the oxidation of the oxide lattice during charge to form peroxo-like oxygen, and the subsequent reduction of peroxo-like oxygen to oxide on discharge. The tendency for the majority of the peroxo-like oxygen to return to oxide suggests that first cycle oxygen redox is mostly reversible in DRX materials, and certainly more reversible than oxygen redox in Li/Mn rich layered oxides.[25] Looking next at the fourth cycle titrations, similar conclusions can be drawn about the reversibility of oxygen redox on subsequent cycles. After the fourth charge, the amount of peroxo-like oxygen present is similar to the amount after first charge. After the fourth discharge, the amount of peroxo-like oxygen is again small, although greater than the amount after the first discharge. These results suggest that the majority of oxygen redox on subsequent cycles is reversible, accompanied by a small portion of peroxo-like oxygen that cannot be reduced. The observed reversibility of oxygen redox indicates that the initial loss in capacity from DRX materials is not due to irreversible oxygen redox. Instead, it appears that there must be some loss of transition metal redox capacity to account for the missing capacity on subsequent cycles.

2.4.9 Fluorine Dissolution from DRX Materials Over Multiple Cycles

To better understand the stability of fluorine in DRX materials during extended cycling, fluoride-scavenging DEMS was conducted on LMNOF for four full cycles. Just like the cells with $LiClO_4$ outlined earlier, the cell contained no sources of fluorine besides LMNOF: the electrolyte was $LiClO_4$ and the binder was PE. The analogous experiment was not conducted on LMNO because the cell contains no sources of fluorine. The voltage profile and corresponding Me_3SiF evolution profile for LMNOF are shown in Figure 2.8. Similar to the LMNO and LMNOF cells with $LiClO_4$ studied previously, the Me_3SiF evolution displays a sloping baseline that decays throughout the experiment. As mentioned earlier, this baseline is attributed to reaction of TMSPa with trace fluorides remaining in the cell. Superimposed on this baseline are four distinct peaks in Me_3SiF evolution, each corresponding to the maximum voltage reached by the cell during charging. These peaks indicate the dissolution of fluorine from LMNOF at high potentials, demonstrating that fluorine continues to dissolve on subsequent cycles. The peaks get smaller as the number of cycles increases, suggesting that the extent of fluorine dissolution decreases over the first few cycles. This result indicates that fluorine dissolution from LMNOF occurs to a diminishing extent over the first several cycles, and only a very minor amount of the total fluorine in the material dissolves during cycling ($\sim$1% over all four cycles). By the fourth cycle, it appears as though fluorine dissolution is nearly exhausted. This attenuation suggests that fluorination dissolution likely occurs at the surface, leading to the formation of a fluorine-depleted region near the surface of LMNOF particles that passivates the material from further fluorine dissolution.

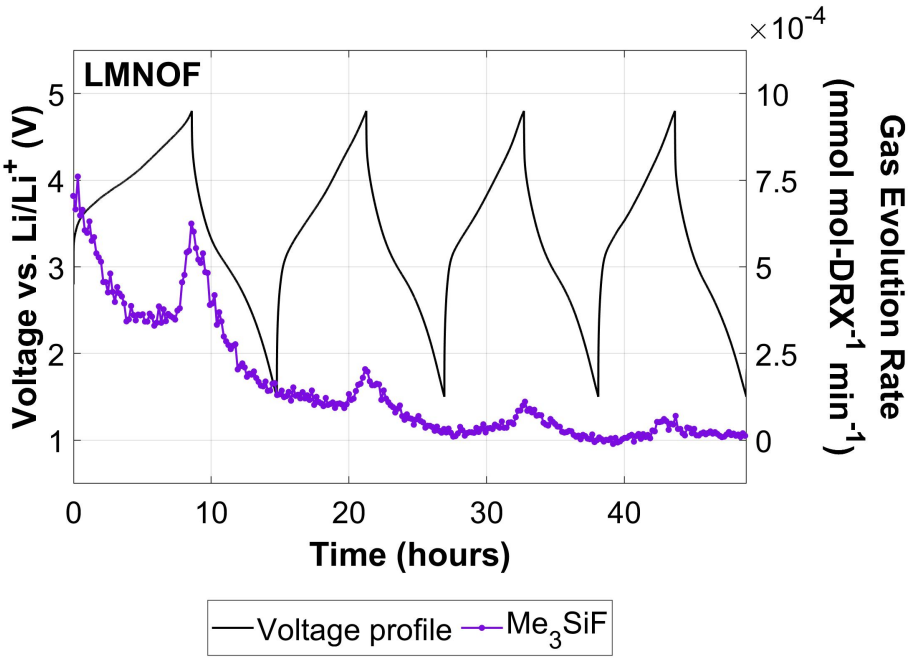

Figure 2.8: Me_3SiF evolution from LMNOF cathode with polyethylene binder in 1M $LiClO_4$ in EC:DEC during the first four cycles. Cycling consisted of charging to 4.8 V vs. Li/Li^+ and discharging to 1.5 V vs. Li/Li^+ a constant current of 0.1 Li hr^{-1} (29.4 mA g-LMNOF^{-1}).

2.5 Conclusions

In this work, we first examined the redox chemistry and interfacial reactivity of DRX materials during the first cycle. We confirmed previous findings that fluorination suppresses oxygen loss from DRX materials upon charging to high potentials. We also showed that fluorination delays the onset of oxygen loss, allowing charging to higher potentials before oxygen evolution begins. We then used quantitative acid titrations to show that peroxo-like oxygen species form due to oxygen redox above 4.2 V vs. Li/Li^+ after $Mn^{3+/4+}$ redox is exhausted. Using an electrolyte additive to monitor fluoride formation, we found that that the fluorine in LMNOF is partially unstable at high voltages, causing a very small fraction ($\sim$1%) to dissolve into the electrolyte as fluoride. We also used this electrolyte additive with $LiPF_6$ electrolyte to show that cathode fluorination negatively impacts electrolyte stability.

Combining the results of the first cycle analysis, we used external measures for the primary electrochemical reactions occurring within DRX materials to account for the capacity expected from the cathodes extracted on first charge. We used the results of this analysis to compare the charge compensation contributions in LMNO and LMNOF, providing a more complete understanding of fluorine incorporation's influence on DRX electrochemistry.

Importantly, while fluorination increases the available transition metal redox capacity in LMNOF due to a stoichiometric effect, it reduces the extent of accessible oxygen redox for reasons that remain unclear. These two effects influence the material capacity in opposite ways, shifting the balance between transition metal and oxygen redox without strongly affecting the total capacity. This effect was extended to explain the effect of fluorination in suppressing oxygen loss. Because fluorination promotes transition metal redox and mitigates oxygen redox, fluorinated materials rely less on oxygen redox to reach high state of charge, causing DRX oxyfluorides to undergo less oxygen loss than comparable DRX oxides.

Next, we examined the reversibility of the primary redox processes and the stability of DRX materials over multiple cycles. We showed that irreversible oxygen loss occurs only on the first cycle of LMNO and LMNOF electrodes, whereas electrolyte degradation continues to occur over several cycles. We also demonstrated that peroxo-like oxygen species continue to form to a similar extent on charge after multiple cycles, and that the majority of this peroxo-like oxygen is consumed on subsequent discharge. This behavior indicates that the majority of charge compensation related to the oxygen lattice is reversible, and that this oxygen redox reversibility is mostly retained after multiple cycles. Using the fluoride-scavenging additive, we also found that fluorine continues to dissolve from LMNOF to a diminishing extent during early cycles. Considering the results of the multiple cycle analysis, we conclude that while DRX materials display promising reversibility with respect to oxygen redox, they also display high susceptibility to degradation reactions in the cell. These findings suggest surface modifications to control interfacial reactivity as an important direction to improve long term cycling, especially for fluorinated cathode materials.

2.6 Supplementary Information

2.6.1 First-Cycle DEMS Experiments

Table 2.1: Cumulative first-cycle O_2 evolution data from LMNO and LMNOF. Cathodes were charged to 4.4 and 4.8 V vs. Li/Li^+ at a constant current of 0.1 Li hr^{-1} and subsequently held at their respective cut-off voltages until the current decayed to 0.01 Li hr^{-1}. Visual comparison of quantities in Figure 2.2 is challenging due to changing gas sampling density with respect to capacity during the voltage hold.

Material	4.4 V Charge (mmol-O_2 mol-DRX^{-1})	4.8 V Charge (mmol-O_2 mol-DRX^{-1})
LMNO	2.1	4.2
LMNOF	0	0.6

LMNO and LMNOF cathodes were charged to various cut-off potentials and held at the cut-off potential until the current decayed to 0.01 Li hr^{-1}. Meanwhile, CO_2 evolution was monitored using DEMS. Figure 2.9 shows the CO_2 evolution rate during charging to 4.4 and 4.8 V vs. Li/Li^+ for both materials, and Table 2.2 contains the accompanying cumulative gas evolution quantities. Both materials display a sloping peak of CO_2 evolution with a maximum at the end of charge. At each cut-off voltage, LMNOF displays greater CO_2 evolution than LMNO.

As mentioned in the multi-cycle DEMS experiment discussed in the main text (Figure 2.6), CO_2 evolution is a parasitic process that can originate either from the oxidation of residual carbonates or the electrolyte solvents: ethylene carbonate and diethyl carbonate.[27,84] Because that Li_2CO_3 oxidizes to form a stoichiometric equivalent of CO_2, the Li_2CO_3 quantities presented in Table 2.3 represent the upper limit of CO_2 evolution anticipated from oxidation of residual Li_2CO_3. Of note, LMNO has nearly three times as much residual Li_2CO_3 as LMNOF, such that LMNO would be expected to display more CO_2 evolution if Li_2CO_3 oxidation solely accounted for CO_2 evolved during cycling.

For each material, significantly more CO_2 is evolved at both cut-off voltages than can be accounted for by residual Li_2CO_3 oxidation alone. This result indicates that a large portion of the CO_2 evolved must come from oxidation of the electrolyte solvent. Furthermore, the increased CO_2 evolution from LMNOF, despite the greater amount of residual Li_2CO_3 on LMNO, indicates that in fact the majority of CO_2 evolution comes from electrolyte solvent oxidation. This conclusion is consistent with the findings of the multi-cycle DEMS experiment and the quantitative acid titrations described in the main text.

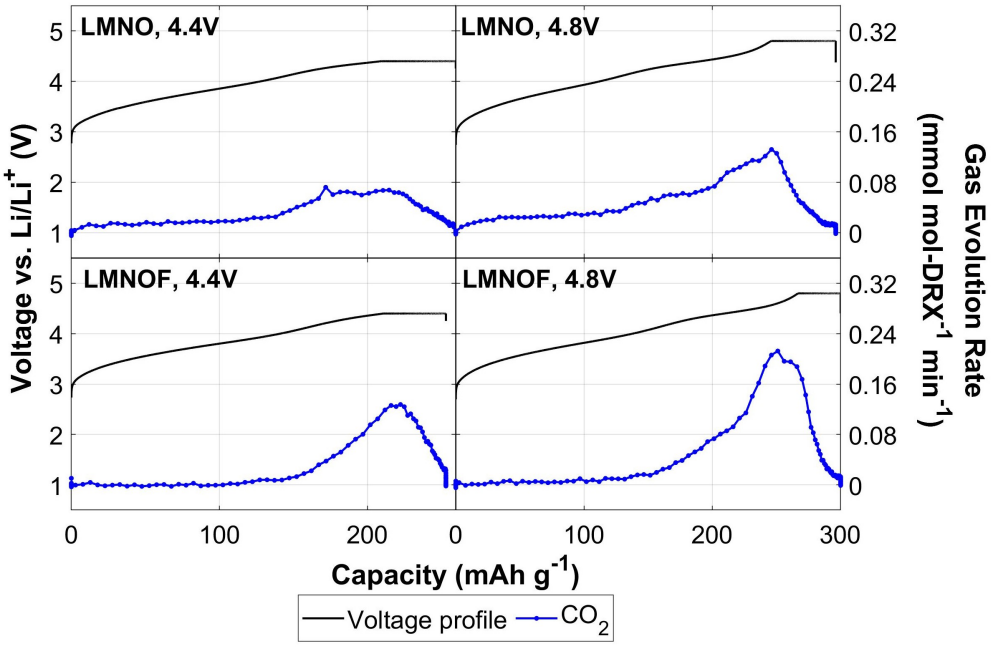

Figure 2.9: CO_2 evolution rates from (top) LMNO and (bottom) LMNOF during the first charge to (left) 4.4 and (right) 4.8 V vs. Li/Li^+. Charging consisted of a constant current charge at 0.1 Li hr^{-1} (29.2 mA g-$LMNO^{-1}$, 29.4 mA g-$LMNOF^{-1}$) to the listed cut-off voltage followed by a potentiostatic hold at the cut-off voltage until current decayed to 0.01 Li hr^{-1}.

Table 2.2: Cumulative first-cycle CO_2 evolution data from LMNO and LMNOF. Cathodes were charged to 4.4 and 4.8 V vs. Li/Li^+ at a constant current of 0.1 Li hr^{-1} and subsequently held at their respective cut-off voltages until the current decayed to 0.01 Li hr^{-1}. Visual comparison of quantities in Figure 2.9 is challenging due to changing gas sampling density with respect to capacity during the voltage hold.

Material	4.4 V Charge (mmol-CO_2 mol-DRX^{-1})	4.8 V Charge (mmol-CO_2 mol-DRX^{-1})
LMNO	25.3	40.0
LMNOF	30.7	40.9

2.6.2 As-Synthesized Material Data

Table 2.3: Amount of residual lithium carbonate on as-prepared LMNO and LMNOF powders, reported in mmol-Li_2CO_3 mmol-DRX^{-1} and wt% Li_2CO_3

Material	mmol-Li_2CO_3 mol-DRX^{-1}	wt% Li_2CO_3
LMNO	23.1	2.1
LMNOF	8.1	0.66

2.6.3 Multiple-Cycle DEMS Experiments

Table 2.4: Cumulative CO_2 and O_2 evolution data for the first four cycles of LMNO and LMNOF cathodes with charging cut-off voltages of 4.45 and 4.8 V vs. Li/Li^+. Cycling consisted of charging to the listed cut-off voltage and discharging to 1.5 V vs. Li/Li^+ at a constant current of 0.1 Li hr^{-1} (29.2 mA g-$LMNO^{-1}$, 29.4 mA g-$LMNOF^{-1}$).

Material	Cut-off Voltage	Cumulative Gas Evolved (mmol-gas mol-DRX^{-1})			
		Cycle 1	Cycle 2	Cycle 3	Cycle 4
CO_2					
LMNO	4.45V	10.8	8.3	5.4	4.1
LMNOF	4.45V	12.5	10.7	8.7	7.3
LMNO	4.8V	25.9	16.3	13.1	12.3
LMNOF	4.8V	40.6	16.3	10.8	10.2
O_2					
LMNO	4.45V	0	0	0	0
LMNOF	4.45V	0	0	0	0
LMNO	4.8V	1.8	0	0	0
LMNOF	4.8V	0.5	0	0	0

Chapter 3

Tuning Bulk Redox and Interfacial Reactivity in Highly-Fluorinated Cation-Disordered Rocksalt Cathodes

3.1 Abstract

Lithium-excess, cation-disordered rocksalt (DRX) materials have been subject to intense scrutiny and development in recent years as potential cathode materials for Li-ion batteries. Despite their compositional flexibility and high initial capacity, they suffer from poorly understood parasitic degradation reactions at the cathode-electrolyte interface. These interfacial degradation reactions deteriorate both the DRX material and electrolyte, ultimately leading to capacity fade and voltage hysteresis during cycling. In this work, differential electrochemical mass spectrometry (DEMS) and titration mass spectrometry are combined to quantify the extent of bulk redox and surface degradation reactions for a set of $Mn^{2+/4+}$-based DRX oxyfluorides during initial cycling with a high voltage charging cut-off (4.8 V vs. Li/Li^+). Increasing the fluorine content from 7.5% to 33.75% is shown to diminish oxygen redox and suppresses high-voltage O_2 evolution from the DRX surface. Additionally, electrolyte degradation processes resulting in the formation of both gaseous species and electrolyte-soluble protic species are observed. Subsequently, DEMS is paired with a fluoride-scavenging additive to demonstrate that increasing fluorine content leads to increased dissolution of fluorine from the DRX material into the electrolyte. Finally, a suite of ex-situ spectroscopy techniques are employed to study the change in DRX composition during charging, revealing the dissolution of manganese and fluorine from the DRX materials at high voltages. This work provides insight into the degradation processes occurring at the DRX-electrolyte interface and points towards potential routes of interfacial stabilization.*

*This chapter is largely adapted, with permission from all co-authors, from previously published work in: Crafton et al. *ACS Appl. Mater. Interfaces* **2023** 15(15), 18747-18762.

3.2 Introduction

The electric vehicle and portable electronic industries have created an enormous demand for low cost, high energy density, resource friendly lithium ion (Li-ion) batteries. The ability of the current commercial battery technology to meet this demand is limited in large part by the cathode active material, which commonly consists of a layered lithium transition metal oxide (TMO) such as $LiCoO_2$ or $Li(Ni_xMn_yCo_z)O_2$.[3,6] These materials possess a limiting electrochemical capacity compared to most prospective anode materials (graphite, Li, etc), thereby limiting the energy density of the full electrochemical cell.[4,11] Furthermore, TMO's often contain scarce or expensive transition metals like Co, raising the cost and limiting the supply of TMO-based cathode materials.[15,57] This limitation has spurred an enormous effort to develop alternative cathode materials with low cost, resource friendly compositions and high electrochemical capacities.[58,86,87] From these efforts, lithium-excess cation-disordered rocksalt (DRX) materials have emerged as a promising class of transition metal oxides and oxyfluorides that display several characteristics that are desirable for applications as Li-ion cathode materials.[64]

DRX materials exhibit the α-$LiFeO_2$ structure wherein the cations (Li, transition metals) and anions (oxygen, fluorine) possess no long-range order within their respective sublattices, although numerous studies have demonstrated the presence and role of short-range order in DRX materials.[44,88–90] This feature is contrasted to the α-$NaFeO_2$ structure of layered TMO cathode materials, in which the cations are arranged in alternating layers of lithium and transition metals.[6]

The cation-disordered structure of DRX materials confers a degree of compositional flexibility that allows for the incorporation of transition metals and anions that are incompatible with layered TMO's, which must maintain their layered structure during cycling. For example, $Ni^{2+/4+}$ and $Co^{3+/4+}$ are the predominantly available transition metal redox couples in layered TMO's because their electronic structure prevents site migration during cycling, a process that would otherwise disrupt the layered structure and impede Li transport.[17,44] Although Mn is often included in layered TMO's, it must remain electrochemically inactive in the Mn^{4+} state to prevent migration into the Li layer.[18] However, because the requirement to form and maintain a layered structure is removed in the case of DRX materials, a wide range of transition metals like Mn, Ni, Fe, V, Cr, and Mo can be employed to provide charge compensation.[48,52,61] The expanded range of accessible transition metals allows for the incorporation of low-cost, Co-free redox centers like Mn and Fe. The compositional flexibility conferred by the cation-disordered structure also allows for the incorporation of fluorine into the anion lattice of DRX materials.[91] In contrast, achieving fluorine incorporation into the anion lattice of layered TMO's is infeasible, and attempts have led instead to the formation of a LiF surface coating.[92] Fluorine substitution has previously been shown to improve the high-voltage stability of DRX cathode materials by suppressing surface degradation processes like oxygen loss and mitigating the extent of structural transformation to a spinel-like phase.[34,37,93] Furthermore, by lowering the average anion valence, fluorination enables the inclusion of transition metals in the 2+ oxidation state, allowing for the utilization of two-

electron redox couples like $Mn^{2+/4+}$. Such 'double' redox couples are desirable because they can provide twice as much charge compensation per transition metal as a one-electron redox couple. Therefore, the compositional flexibility conferred by the cation-disordered structure greatly enhances the variety and tunability of DRX materials, allowing the formulation of DRX materials with resource friendly composition and high stability.[32,62,93]

The cation-disordered structure of DRX materials also creates a large amount of local environments referred to as Li-O-Li configurations, in which two Li ions are bonded to an oxygen atom on opposite sides from one another. Li-O-Li configurations, which do not exist in perfectly ordered layered TMO's without Li-excess composition, give rise to an electronic structure in which bulk oxygen redox may occur at potentials in the range of 4.0 - 4.6 V vs. Li/Li^+.[23] The abundance of Li-O-Li configurations induced by the cation-disordered structure therefore creates another potentially reversible redox reservoir in DRX materials, increasing the capacity available during cycling. These two features of compositional flexibility and abundance of Li-O-Li configurations, both of which are consequences of the cation-disordered structure, make DRX materials promising candidates for next-generation cathode materials.

Despite these promising characteristics, DRX materials still suffer from several issues that limit their long-term cyclability. One key limitation is the degradation imposed by the high interfacial reactivity of DRX cathode materials. Extracting the promisingly high capacities from DRX materials requires cycling to high potentials (4.8 V vs. Li/Li^+), which leads to degradation at the cathode-electrolyte interface. This degradation drives the depletion of electrolyte; formation of a densified, reduced TMO layer; generation of reactive electrolyte degradation products; and evolution of gaseous species such as O_2 and CO_2.[34,37,49] In turn, these processes lead to capacity loss and impedance rise in the cell, limiting the attainable energy density from cells containing DRX materials.[52,93]

To address these shortcomings, there have been many efforts to improve the stability and cyclability of DRX materials.[34,37,48,94] In this work, we leverage the compositional flexibility of DRX materials by studying a set of DRX oxyfluorides with varying degrees of fluorination and, hence, $Mn^{2+/4+}$ redox. The DRX materials investigated are LMNOF-4515 ($Li_{1.2}Mn_{0.45}Nb_{0.35}O_{1.85}F_{0.15}$), LMNOF-6060 ($Li_{1.2}Mn_{0.60}Nb_{0.20}O_{1.40}F_{0.60}$), and LMNOF-6368 ($Li_{1.2}Mn_{0.625}Nb_{0.175}O_{1.325}F_{0.675}$). A previous publication by Yue et al. has investigated the structure and morphology of these materials as well as the redox processes that occur within the bulk of the materials during electrochemical cycling.[52] The three materials studied herein consist of nanosized crystallites of comparable particle size (100-200 nm). These materials achieve bulk charge compensation during cycling via two primary electrochemical processes: $Mn^{2+/4+}$ redox and oxygen redox. They also contain electrochemically-inactive Nb^{5+}, which stabilizes the disordered structure. Herein, we conduct ex-situ acid titration mass spectrometry (TiMS) on cycled cathodes to demonstrate that increasing fluorination from 7.5% to 33.75% deactivates bulk oxygen redox in DRX materials, shifting the entirety of the electrochemical capacity to $Mn^{2+/4+}$ redox. We also couple TiMS with in-situ differential electrochemical mass spectrometry (DEMS) to show that increasing the fluorine content in DRX materials influences the surface reactivity of DRX cathodes, stabilizing surface carbonate

species at high voltages. We then extend our DEMS analysis over multiple cycles, demonstrating that fluorination suppresses high-voltage oxygen evolution from DRX cathodes and revealing multiple modes of electrolyte degradation that slowly diminish throughout cycling for all three DRX materials. Next, we introduce into our DEMS cells a fluoride-scavenging electrolyte additive to observe fluorine dissolution from the DRX materials in-situ, showing that increasing DRX fluorine content increases the amount of fluorine that dissolves from the DRX material into the electrolyte.[75,95] Finally, we use X-Ray photoelectron spectroscopy (XPS), inductively coupled plasma optical emission spectroscopy (ICP-OES), and solid-state nuclear magnetic resonance spectroscopy (SS-NMR) to monitor the change in DRX composition during the first charge, revealing the deposition of electrolyte degradation products and the dissolution of DRX-originating Mn and F.

3.3 Experimental Methods

3.3.1 Synthesis of Li-excess $LiMn^{2+}Nb^{5+}OF$ DRX Materials

All $LiMn^{2+}Nb^{5+}OF$ DRX materials were synthesized via a mechanochemical reaction. Precursors of lithium oxide, manganese (II) oxide, niobium (V) oxide, and lithium fluoride were used. All precursors were weighed stoichiometrically except lithium oxide (10% excess) and loaded inside a stainless-steel jar, then sealed tightly inside an Ar-fill glove box. The precursors were high-energy milled extensively until the pure rocksalt phase was formed. The milled powder was then collected inside the glove box. Detailed synthesis conditions can be found in our previous report.[52]

3.3.2 Cathode Preparation

The as-synthesized DRX active material was first mixed with acetylene black (AB) conductive carbon powder in a DRX:AB ratio of 6:3 (wt). Cathodes for all experiments except fluoride-scavenging DEMS were made using a slurry mixing technique. The DRX-AB powder mixture was mixed with a solution of 10wt% polyvinylidene fluoride (PVDF) binder dissolved in N-Methyl-2-pyrrolidone (NMP, Sigma) in a mortar and pestle until a uniform slurry was formed. The DRX:AB powder and PVDF/NMP solution were combined to produce an approximate composition of 60:30:10 (wt) DRX:AB:PVDF. The resulting slurry was then spread onto stainless steel mesh and dried at 90°C for 30 minutes. After this brief initial drying, the electrodes were pressed with uniform pressure using a screw-driven clamp and dried overnight under vacuum at 120°C. For fluoride-scavenging experiments, the electrodes were fabricated using a dry technique using polyethylene (PE) (Sigma) as the binder instead of PVDF. The DRX:AB mixture was combined with PE powder to produce an approximate composition of 60:30:10 (wt) DRX:AB:PE. The powders were ground together in a mortar and pestle, and the resulting mixture was placed on stainless steel mesh before being pressed

into place using a steel pin. Typical DRX loading in all measurements was 7 mg cm^{-2}, and all electrodes were 1/2 inch in diameter (1.3 cm^2).

3.3.3 Electrochemical Cell Preparation

Custom-built Swagelok cells were used as described previously.[80–82] Li foil was used as the counter electrode in all cells except for those used to prepare electrodes for XPS analysis or those used to verify the H_2 formation mechanism. For the cells used to prepare electrodes for XPS analysis, the counter electrode was graphite (Argonne National Laboratory CAMP Facility, 91.83wt% Superior Graphite SLC 1406T, 2wt% Timcal C45 carbon, 6wt% Kureha 9300 PVDF binder, 0.17% Oxalic Acid on 10μm Cu foil). For the control experiments verifying the formation mechanism of H_2, the counter electrode was delithiated lithium iron phosphate (Argonne National Laboratory CAMP Facility, 90wt% Johnson Matthey Lithium Iron Phopshate, 5wt% Timcal C-45, 5wt% Solvay 5130 PVDF Binder on 20μm Al foil). The separator in all cells was composed of 1 sheet of Whatman QMA filter paper (on the counter electrode side) and 1 sheet of Celgard 2500 (on the DRX side). The electrolyte varied depending on the type of experiment. For DEMS experiments measuring the evolution of O_2, CO_2, and H_2, the electrolyte was 1M lithium hexafluorophosphate ($LiPF_6$, Gotion) in 1:1 (vol) mixture of ethylene carbonate (EC, Gotion):diethyl carbonate (DEC, Gotion). For the experiments preparing electrodes for XPS analysis and for those verifying the H_2 formation mechanism, the electrolyte was also 1M $LiPF_6$ in 1:1 (vol) EC:DEC. For DEMS experiments monitoring fluoride dissolution from the DRX material, the electrolyte was 1M lithium bis(trifluoromethanesulfonyl)imide (LiTFSI, BASF) in 1:1 (vol) EC:DEC with 1vol% tris(trimethylsilyl)phosphate (TMSPa, Sigma). For DEMS experiments monitoring formation of fluoride from either the DRX material or the electrolyte, the electrolyte was 1M $LiPF_6$ in 1:1 (vol) EC:DEC with 1vol% TMSPa. For all DEMS cells, the electrolyte loading was 60 μL cm^{-2}. Despite the low concentration of TMSPa in the electrolyte for fluoride-scavenging DEMS cells, the highest amount of fluoride formation observed in any experiment was a fraction of the amount of TMSPa present ($\sim$30%), leading us to conclude that there is an excess of TMSPa in the electrolyte relative to the amount of fluoride available for reaction.

3.3.4 Electrochemical Testing and DEMS Gas Analysis

The custom-built DEMS instrument and its operation was described in previous publications.[80–82] Hermetically-sealed, custom-built Swagelok cells were assembled in an Argon atmosphere glovebox and appropriately attached to the DEMS apparatus to avoid air exposure. The cells were cycled on a Bio-Logic VSP-series potentiostat under positive Ar pressure (approximately 1.2 bar). For all experiments, cells were cycled at a current of 0.1 Li hr^{-1} (27.3 mA g^{-1} for LMNOF-4515, 28.6 mA g^{-1} for LMNOF-6060, and 28.8 mA g^{-1} for LMNOF-6368) to cut-off potentials listed with each experiment. In some cases, the cells were then held at the relevant cut-off potential until the current decayed to 10% of its original value,

or 0.01 Li hr^{-1}. Throughout the experiment, the cell headspace was purged with 500 μL of Ar by the DEMS instrument every 10 minutes and any accumulated gases were swept to the mass spectrometer chamber for analysis. The apparatus is calibrated for O_2, CO_2, H_2, and trimethylsilyl fluoride (Me_3SiF) in Ar, allowing for the determination of the partial pressures of each analyte. The amount of each gas evolved was then quantified using the known volume, temperature, and partial pressure of the gas in each sample through the ideal gas law.

3.3.5 TiMS Analysis of DRX Powders and Electrodes

The design and operation of the custom-built TiMS instrument is nearly identical to that of the DEMS instrument, as described in previous publications.[49,80–82] For studies on the as-synthesized materials, pristine cathodes were placed in a custom-built, hermetically sealed titration vessel. For studies on charged cathodes, rinsed and dried cathodes extracted from electrochemical cells were instead placed in the titration vessel. This vessel was then appropriately connected to the TiMS apparatus to avoid air exposure. During the experiment, the cell headspace was purged with 2 mL of Ar by the TiMS instrument every 2 minutes and any accumulated gases were swept to the mass spectrometer chamber for analysis. After establishing baseline levels for gases of interest, 1 mL of N_2-sparged 10M H_2SO_4 was injected into the titration vessel through a septum-sealed injection port. The resulting acid-cathode mixture was mixed with a magnetic stir bar. Gas samples were taken until the reaction was completed, as determined by the return of any analyte signals to their baseline levels. The apparatus is calibrated for O_2 and CO_2 in Ar, allowing for the determination of the partial pressures of each analyte. The amount of each gas evolved was then quantified using the known volume, temperature, and partial pressure of the gas in each sample through the ideal gas law. For all charged cathode samples, the charging procedure consisted of a constant current charge to the listed cut-off voltage at 0.1 Li hr^{-1} followed by a potentiostatic hold at the cut-off until the current decayed to 0.01 Li hr^{-1}. After the voltage hold, the cell was returned to the glovebox, minimizing air exposure. Once inside the glovebox, the cell was disassembled, and the cathode was placed in a dry vial. The cathode was rinsed three times with 200 μL DEC and dried under vacuum at room temperature for several hours. The dried cathodes were then stored in a sealed vial in the glovebox until TiMS analysis.

3.3.6 ICP-OES Analysis of Mn Dissolution

Inductively coupled plasma optical emission spectroscopy (ICP-OES) measurements were performed using a Perkin Elmer 5300 DV optical emission inductively coupled plasma spectrometer with an auto sampler. For all samples and standards, a matrix solution consisting of 2wt% HNO_3 (70%, Sigma Aldrich) and 0.1wt% $H_2C_2O_4$ (oxalic acid dihydrate, Suprapur, Sigma Aldrich) in deionized water was used. A manganese standard solution for ICP-OES (Sigma Aldrich) was diluted with matrix solution to four different concentrations to calibrate manganese between 0-1 mg L^{-1}, and all sample measurements fell within the cali-

brated range. Electrolyte and anode samples were obtained from DRX cells by recovering the electrolyte-soaked separator and Li metal anode from Swagelok-type cells. To allow for easier removal, the Li metal anode was backed by a sheet of stainless steel foil. Each DRX material was subjected to three different cycling procedures: rest on open-circuit (OCV), charge to 4.0 V, and charge to 4.8 V. The OCV procedure consisted of simply allowing the cell to rest on open-circuit for 24 hours. The charging procedures consisted of a constant current charge at 0.1 Li hr^{-1} to the listed cut-off voltage followed by a potentiostatic hold at the cut-off voltage until the current decayed to 0.01 Li hr^{-1}. After the potentiostatic hold, the cell was allowed to rest at open-circuit until the cell had been intact for 24 hours, ensuring similar electrode-electrolyte contact times for all three cycling procedures. After the end of a cycling procedure, the cell was returned to an Ar-filled glovebox where the separator and anode were each separately extracted and dried under vacuum overnight. After drying, the separator and anode were separately dissolved in 20 mL of matrix solution. The resulting solutions were stored for three days to allow for full dissolution of Mn ions, after which the solutions were filtered. The concentration of Mn ions in the resulting filtered solution was then analyzed by ICP-OES, and the DRX-normalized manganese dissolution for each cell was back-calculated from the electrode loading and the sum of the amounts of Mn detected in the separator and electrolyte samples.

3.3.7 XPS Analysis of DRX Electrodes

X-ray photoelectron spectroscopy (XPS, Thermo Fisher, USA) measurements were conducted to analyze the chemical states of each element. The photoelectron spectrometer system is configured with an Al Kα excitation source with spot size of 400 μm. Before collecting XPS spectrum, ion flood source is adopted for charge neutralization. XPS data were analyzed using CasaXPS software. The binding energy scale of the XPS spectra was calibrated from the C1s C-C peak at 284.8 eV, and peaks were fit with a LF lineshape on top of a Shirley background. For the charged sample of each DRX material, the charging procedure consisted of a constant current charge at 0.1 Li hr^{-1} to 4.8 V followed by a potentiostatic hold at 4.8 V until the current decayed to 0.01 Li hr^{-1}. After charging, the cell was returned to the Ar-filled glovebox, where the cathode was extracted, rinsed with DEC, and dried under vacuum overnight.

3.3.8 SS-NMR Analysis of DRX Powders and Electrodes

Solid-state NMR spectra were recorded at B_0=2.35 T (100 MHz for ^{1}H) using a wide bore Bruker BioSpin spectrometer equipped with a DMX 500 MHz console and a custom made 1.3 mm X-broadband magic angle spinning (MAS) probe (tuned to ^{7}Li: 38.9 MHz or ^{19}F: 94.1 MHz). To avoid air exposure, samples were packed in zirconia rotors in an Ar-filled glovebox and spun at ν_R = 60 kHz using dry nitrogen. ^{19}F and ^{7}Li NMR chemical shifts were externally referenced against pure lithium fluoride powder (LiF, $\delta_{iso}(^{19}F)$ = -204 ppm and $\delta_{iso}(^7Li)$ = -1 ppm). Both ^{7}Li and ^{19}F MAS NMR spectra were obtained using a

rotor synchronized spin-echo sequence (90° - τ_R - 180° - τ_R) with 90° radiofrequency (RF) pulses of 0.45 μs and 0.34 μs, respectively. For both nuclei, a total of 7616 transients were averaged with a recycle delay of 50 ms. This short recycle delay was enough to reach fully relaxed ^{7}Li NMR spectra while in ^{19}F NMR, only signal around -190 ppm (from F in the LMNOF cathode) were fully relaxed. In addition, isotropic ^{7}Li and ^{19}F NMR spectra were recorded using the projected magic angle turning phase-adjusted sideband separation (pj-MATPASS) pulse sequence which effectively removes spinning sidebands due to MAS.[96,97] Both experiments used the same 90° RF pulses as their corresponding spin echoes and data were averaged over 4000 scans with a recycle delay of 50 ms. Solid-state NMR data were processed using Bruker TopSpin 3.6.0 and spectra were fitted using DMfit software.[98] For the charged sample of each DRX material, the charging procedure consisted of a constant current charge at 0.1 Li hr^{-1} to 4.8 V followed by a potentiostatic hold at 4.8 V until the current decayed to 0.01 Li hr^{-1}. After charging, the cell was returned to the Ar-filled glovebox and disassembled. The charged DRX cathode was then extracted, rinsed three times with 200 μL DEC, and dried under vacuum overnight. For both the pristine and charged samples, electrode material containing DRX material, acetylene black, and PVDF was scraped from the stainless steel mesh current collector and collected for analysis. For the active material sample, the carbon-coated DRX powder containing only DRX material and acetylene black was used.

3.4 Results and Discussion

3.4.1 Comparison of Voltage Profiles

To interpret the bulk electrochemical properties of the DRX materials, all three LMNOF materials were subjected electrochemical cycling consisting of charging to 4.8 V and discharging to 1.5 V at a constant rate of 0.1 Li hr^{-1}. The voltage profiles for the first charge and discharge for LMNOF-4515, LMNOF-6060, and LMNOF-6368 are shown in Figure 3.1a. The initial charge capacities of LMNOF-4515, LMNOF-6060, and LMNOF-6368 were 269 mAh g^{-1}, 246 mAh g^{-1}, and 260 mAh g^{-1}, respectively. The initial discharge capacities, in contrast, were similar: 218 mAh g^{-1} for LMNOF-4515, 216 mAh g^{-1} for LMNOF-6060, and 212 mAh g^{-1} for LMNOF-6368. While the voltage profiles for all three materials possess the same general shape, that of LMNOF-4515 has more strongly defined charge plateaus around 3.5 V and 4.4 V, whereas those of LMNOF-6060 and LMNOF-6368 are more consistently sloping throughout the voltage range. The shape of the voltage profiles can be evaluated more rigorously by viewing the same voltage profile information in dQ dV^{-1} vs. V format (where Q is capacity), as shown in Figure 3.1b. In this format, it is apparent that the dQ dV^{-1} profile for the first charge of LMNOF-4515 has pronounced peaks centered at 3.5 V and 4.4 V, while the dQ dV^{-1} profiles for the first charge of LMNOF-6060 and LMNOF-6368 tend to be flatter and broader. This difference indicates that two primary redox processes in LMNOF-4515 provide bulk charge compensation at relatively well-defined voltages

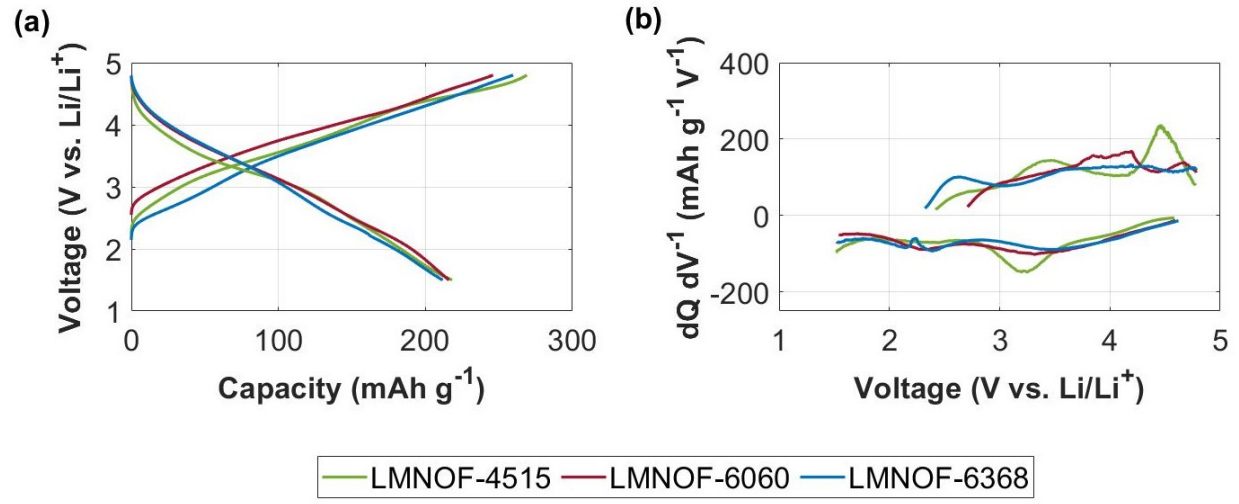

Figure 3.1: First charge-discharge comparison for the three LMNOF materials. (a) Voltage profiles during first charge-discharge and (b) corresponding $dQ\,dV^{-1}$ for all three DRX materials. All materials were charged to 4.8 V vs. Li/Li^+ and discharged to 1.5 V vs. Li/Li^+ at a constant current rate of 0.1 Li hr^{-1}. The electrolyte was 1M $LiPF_6$ in 1:1 EC:DEC.

in LMNOF-4515, whereas the primary redox processes in LMNOF-6060 and LMNOF-6368 provide charge compensation across a wider range of voltages. The less defined nature of the redox processes occurring during charging of LMNOF-6060 and LMNOF-6368, when compared to those of LMNOF-4515, suggests that a broader distribution of Li site energies exists in the more highly fluorinated materials.[89]

Based on prior studies investigating the bulk redox processes occurring in LMNOF DRX materials, we ascribe the low-voltage (∼3.5 V vs. Li/Li^+) process in LMNOF-4515 to $Mn^{2+/4+}$ redox and the high-voltage (∼4.4 V vs. Li/Li^+) process to oxygen redox.[52] In contrast, it is challenging to assign based on voltage profile information alone the electrochemical processes occurring in LMNOF-6060 and LMNOF-6368, as the voltage plateaus during cycling are less defined. To further understand and quantify the bulk redox processes supplying electrochemical capacity in these materials, quantitative ex-situ TiMS was employed to measure the amount of oxidized oxygen species in the DRX materials at various states of charge.

3.4.2 Nature of Redox Processes in LMNOF Materials

To elucidate the extent to which $Mn^{2+/4+}$ and oxygen redox contribute to the observed electrochemical capacity, ex-situ acid titrations were conducted using TiMS to analyze DRX cathodes extracted throughout the first charge. Specifically, a pristine cathode containing

the as-synthesized DRX material along with cathodes extracted after charging to 4.4, 4.6, and 4.8 V vs. Li/Li^+ were studied. During TiMS, any oxidized oxygen species present in the bulk of the DRX material will dissolve into the acid solution where they will undergo a disproportionation reaction to yield O_2 gas and H_2O.[25,83] This disproportionation reaction will yield 1 mole of O_2 gas for every 4 moles of electrons extracted during oxidation of the oxide lattice, as described in Section 3.6.1 and demonstrated in previous publications.[37,49] Using the TiMS system, the total amount of O_2 gas evolved from each extracted cathode during acid titration was quantified. Using the stoichiometry associated with the oxygen disproportionation reaction, the amount of O_2 gas evolved was then used to calculate the extent of oxide oxidation and thereby the charge capacity associated with bulk oxygen redox. The total capacity extracted from each electrode, along with the oxygen redox capacity determined by TiMS, were then used to back-calculate the average Mn oxidation state in each cathode according to the composition of each material. The results of this analysis are shown in Figure 3.2. This analysis relies on the assumption that all capacity comes from either Mn or oxygen redox. While a small amount of capacity is inevitably contributed by the irreversible formation processes studied herein, we expect that the error introduced by this assumption is small relative to the large capacity associated with the bulk redox processes.[37] This expectation is further supported by the scale of the degradation reactions observed throughout the rest of this study, which remains small relative to the scale of the bulk electrochemical reactions.

The results in Figure 3.2 demonstrate the mixed contributions of $Mn^{2+/4+}$ and oxygen redox to the charge capacity extracted from the LMNOF materials. Below 4.4 V vs. Li/Li^+, $Mn^{2+/4+}$ redox clearly dominates in LMNOF-4515 because the Mn oxidation state rises linearly with capacity while very little oxygen redox occurs. Above 4.4 V vs. Li/Li^+, oxygen redox begins to dominate in LMNOF-4515 as the Mn oxidation state approaches 4+. In comparison, the majority of charge compensation in LMNOF-6060 appears to come from Mn redox throughout the entire first charge, with very small contributions from oxygen redox above 4.4 V vs. Li/Li^+. The average Mn oxidation state in LMNOF-6060 reaches about 3.5+, indicating that the Mn redox couple is not fully exhausted during charging. Finally, in the case of LMNOF-6368, the entirety of charge compensation during the first charge comes from $Mn^{2+/4+}$ oxidation, with no measurable oxygen redox taking place. At the top of charge, the average Mn oxidation state in LMNOF-6368 is about 3.4+. In total, the amounts of Li deintercalated from the cathodes extracted at 4.8 V vs. Li/Li^+ are 1.02 mol-Li mol-DRX^{-1} for LMNOF-4515, 0.87 mol-Li mol-DRX^{-1} for LMNOF-6060, and 0.85 mol-Li mol-DRX^{-1} for LMNOF-6368. Based on prior replicate experiments, the estimated variability in the amount of Li extracted during charging is 0.02 Li hr^{-1}.

Interpreting the bulk redox contributions from the LMNOF materials relies on an understanding of how much Li extraction per formula unit DRX can be charge compensated by $Mn^{2+/4+}$ oxidation. Increasing fluorination in the LMNOF materials comes with a corresponding increase in Mn content. Because Mn undergoes a 2-electron oxidation from Mn^{2+} to Mn^{4+}, 2 Li may be extracted for every Mn that is fully oxidized. In LMNOF-4515, Mn oxidation can therefore theoretically account for 0.9 mol-Li mol-DRX^{-1}. In LMNOF-6060,

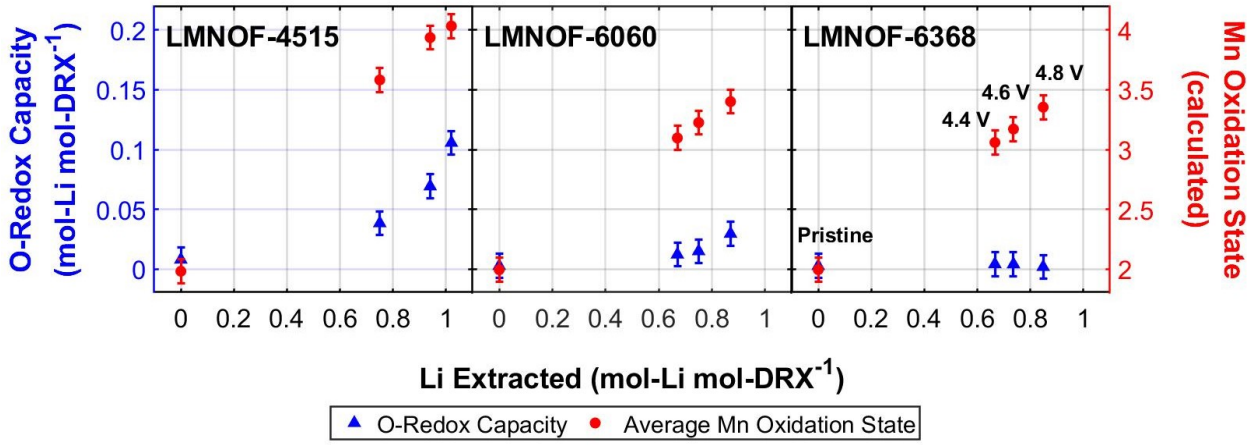

Figure 3.2: Bulk redox analysis for LMNOF materials. The pristine sample is a pristine DRX electrode, and the remaining samples are DRX electrodes charged to the listed cut-off voltage vs. Li/Li^+. Charging consisted of a constant current charge at 0.1 Li hr^{-1} to the listed cut-off voltage vs. Li/Li^+ followed by a potentiostatic hold at the cut-off voltage until the current decayed to 0.01 Li hr^{-1}. After the potentiostatic hold, the cells were allowed to rest on open circuit. The electrolyte was 1M $LiPF_6$ in 1:1 EC:DEC. Data labels are included only for LMNOF-6368, but the order of the data points (in the horizontal direction) with regards to electrode condition is the same for the other two materials. Error bars are based on a standard error of 2.5 mmol-gas mol-DRX^{-1} obtained from prior replicate experiments.

on the other hand, there is exactly enough Mn to provide charge compensation for the removal of the entire amount of Li (1.2 mol-Li mol-DRX^{-1}). Finally, in LMNOF-6368, there is more Mn than is needed to provide charge compensation for the entirety of the Li. This stoichiometry implies that it is impossible to drive complete oxidation to Mn^{4+} via delithiation alone in LMNOF-6368.

Comparing the amount of oxygen redox occurring in these three materials demonstrates the role of fluorination in tuning the bulk redox processes in DRX materials. Increasing the extent of fluorination from 7.5% (LMNOF-4515) to 30% (LMNOF-6060) leads to a significant decrease in the capacity provided by oxygen redox, and further increasing the extent of fluorination to 33.75% (LMNOF-6368) diminishes the oxygen redox process to the point that it does not supply any appreciable capacity. This observation is consistent with previous findings in similar DRX materials that fluorination suppresses oxygen redox.[37,52] As explained earlier, an increase in fluorine content is accompanied by an increase in Mn content, raising the theoretical Mn capacity. This increase in Mn content is likely to reduce the demand placed on oxygen redox to provide charge compensation at the end of charge. Another factor that may contribute to the effect of fluorination on oxygen redox is the amount of Li-O-Li environments present in the DRX material during charging, which will

decrease as the lattice oxygen is increasingly replaced with fluorine.

Despite the associated increase in Mn content, the total Li extracted upon charging to 4.8 V vs. Li/Li^+ decreases slightly with increasing fluorination. The amount of Li extracted during charging is determined by multiple factors, including the amount of percolating Li and the distribution of Li site energies. The effects of increasing fluorination on these factors have previously been investigated by multiple studies. Ouyang et al. reported that increasing fluorination in the material set studied herein increases the amount of percolating Li, thereby improving Li transport.[88] Additionally, Kitchaev et al. showed that increasing fluorine content influences the Li site energy distribution by increasing the amount of Li coordinated to a high number of F anions.[66] Li in these high F-coordination environments would be highly stable and require a potential greater than 4.8 V vs. Li/Li^+ for deintercalation during charge due to strong binding to the F anions. Given that our experimentally observed trend of decreasing capacity with increasing fluorination is inconsistent with the expected change in the amount of percolating Li and consistent with the expected change in the Li site distribution, we conclude that the change in Li site distribution is the primary factor affecting the amount of Li extracted during charging. As a consequence of the decreasing extractable Li and increasing Mn content, the average Mn oxidation state at the top of charge decreases with increasing fluorine content, reflecting decreased fractional utilization of the Mn redox reservoir. An additional factor that may play a role in the observed effects of fluorination is reduced lattice covalency due to poorer metal-ligand orbital overlap.[99,100] Reduced lattice covalency would lower the energy of antibonding TM-d-states, potentially impeding complete utilization of the transition metal redox reservoir. Lastly, we note that the trend of decreasing total charge capacity with increasing fluorination differs from the results presented in Section 3.4.1, which we ascribe to poorer rate control in the experiments in Section 3.4.1 due to the lack of a potentiostatic hold at the end of the constant current charge.

3.4.3 Evolution of Surface Carbonates During Cycling

Lithium carbonate commonly exists in small quantities as an impurity on the surface of all Li-ion cathode active materials, including layered oxides and DRX materials, either as residual precursor from synthesis or as a product of exposure to CO_2 during material handling and processing.[27,49] This species is referred to as native carbonate, referring to the fact that it is present on the as-synthesized material before exposure to the electrolyte. Separately, additional carbonate-like species can form on the surface of DRX materials during cycling as a result of degradation of the electrolyte.[37,49,83] These surface carbonate species, both native and electrolyte-originating, may decompose to evolve gaseous CO_2 due to either electrochemical oxidation or reaction with acidic electrolyte degradation products.[27,49] In addition to the reactions involving these various surface carbonate species, CO_2 can also arise from oxidative electrolyte degradation at the cathode surface.[37,49] While CO_2 evolution can be monitored in-situ using DEMS, it is not possible to decouple electrolyte degradation from surface carbonate degradation as sources of CO_2 using in-situ gas evolution data alone.

To more accurately evaluate the specific processes underlying the observed CO_2 evolution, in-situ DEMS analysis of CO_2 evolution was paired with ex-situ TiMS analysis of surface carbonate species on DRX samples extracted from DEMS cells throughout the first charge. Upon exposure to acid during TiMS, any carbonate-like species on a DRX sample will decompose in the acidic solution to yield CO_2 as described in Section 3.6.1. For each DRX material, CO_2 evolution was measured by TiMS during acid titration of a pristine cathode and cathodes charged to 4.4, 4.6, and 4.8 V vs. Li/Li^+. For the charged samples, charging consisted of a constant current charge at 0.1 Li hr^{-1} to the selected cut-off voltage followed by a potentiostatic hold at the cut-off voltage until the current decayed to 0.01 Li hr^{-1}. For each titration, the CO_2 evolution measured by TiMS was quantified and used to determine the amount of surface carbonate species present on each DRX sample. Under this mode of analysis, surface carbonate decomposition should result in CO_2 evolution during DEMS accompanied by a corresponding decrease in the amount of surface carbonate measured subsequently by TiMS. In contrast, electrolyte degradation should result in CO_2 evolution during DEMS with either increasing or constant amounts of surface carbonate as measured by TiMS. With this insight, the change in surface carbonate measured by TiMS along with the in-situ CO_2 evolution data measured by DEMS can be used to evaluate the extents to which surface carbonate decomposition and electrolyte degradation occur between each cut-off voltage.

The DEMS CO_2 evolution data and corresponding TiMS surface carbonate measurements together reveal the processes underlying CO_2 evolution in the cell. The DEMS CO_2 evolution results for each material when charged to 4.8 V vs. Li/Li^+, along with the carbonate titration results for each cathode studied, are shown in Figure 3.3. The remaining CO_2 evolution results obtained by DEMS for the cathodes charged to 4.4 and 4.6 V vs. Li/Li^+ are shown in Figure 3.9. Furthermore, the cumulative CO_2 evolution results from each DEMS experiment are given in Table 3.1 and the amounts of surface carbonate measured by TiMS for each cathode are given in Table 3.2. During initial charging to 4.4 V vs. Li/Li^+, there is a large amount of CO_2 evolution from all three materials that reaches a maximum at 4.4 V vs. Li/Li^+. The quantity of CO_2 evolved is largest from LMNOF-6368, whereas the quantity evolved is slightly smaller for LMNOF-4515 and LMNOF-6060. Concurrently, there is an increase in the carbonate-like species on the surface of all three DRX materials, which is greatest for LMNOF-4515 and slightly smaller for LMNOF-6060 and LMNOF-6368. These results indicate that there is significant electrolyte degradation leading to CO_2 evolution as well as carbonate deposition on the cathode surface during initial charging to 4.4 V vs. Li/Li^+.

During continued charging of LMNOF-4515 from 4.4 to 4.8 V vs. Li/Li^+, a second peak of CO_2 evolution that reaches a maximum at the start of the voltage hold at 4.8 V vs. Li/Li^+ is observed. LMNOF-6060 and LMNOF-6368, in contrast, do not display this secondary CO_2 evolution peak. Instead, for LMNOF-6060 and LMNOF-6368, the CO_2 evolution rate decreases monotonically to zero after the peak at 4.4 V vs. Li/Li^+. Interestingly, this second peak of CO_2 evolution coincides with a dramatic decrease in surface carbonate content measured using TiMS for LMNOF-4515. As can be seen in Figure 3.3, the amount of surface

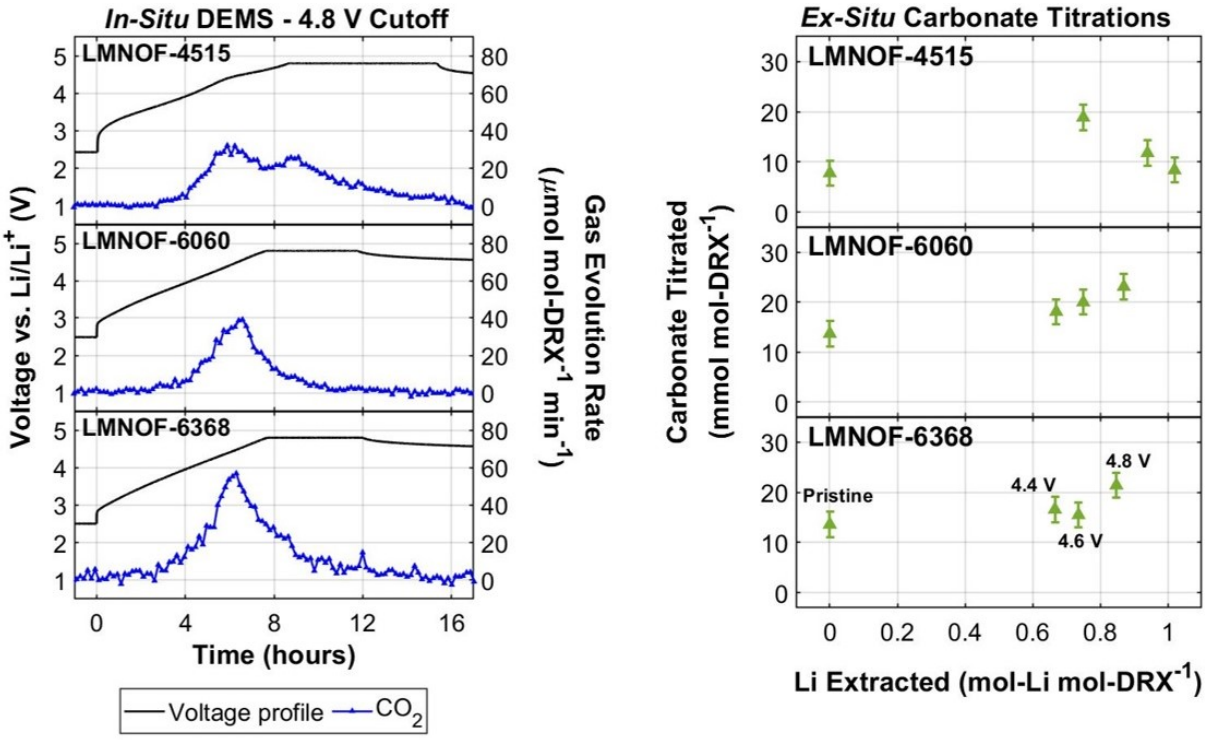

Figure 3.3: In-situ CO_2 evolution during charging of LMNOF materials to 4.8 V vs. Li/Li^+ as measured by DEMS (left) and surface carbonate species on LMNOF materials as measured by ex-situ TiMS (right). For electrode titrations, the pristine sample is a pristine DRX electrode and the remaining samples are DRX electrodes charged to the listed cut-off voltage (vs. Li/Li^+). Charging consisted of a constant current charge at 0.1 Li hr^{-1} to the listed cut-off voltage, followed by a potentiostatic hold at the cut-off voltage until the current decayed to 0.01 Li hr^{-1}. After the potentiostatic hold, the cells were allowed to rest on open circuit. The electrolyte was 1M $LiPF_6$ in 1:1 EC:DEC. Data labels are included only for LMNOF-6368, but the order of the data points (in the horizontal direction) with regards to electrode condition is the same for the other two materials. Error bars are based on a standard error of 2.5 mmol-gas mol-DRX^{-1} obtained from prior replicate experiments.

carbonate decreases consistently from 4.4 to 4.8 V vs. Li/Li^+ for LMNOF-4515 whereas it continues to increase for LMNOF-6060 and LMNOF-6368. These observations therefore indicate that there is significant surface carbonate decomposition occurring on LMNOF-4515 during charging from 4.4 to 4.8 V vs. Li/Li^+, leading to CO_2 evolution and a decrease in the amount of surface carbonate. In contrast, such surface carbonate decomposition does not occur to a significant extent from LMNOF-6060 or LMNOF-6368, causing the observed lack of CO_2 evolution and steady rise in surface carbonate.

The observed differences in electrolyte degradation and surface carbonate decomposition

reveal the important role of DRX surface composition in controlling interfacial reactivity. The lack of surface carbonate decomposition above 4.4 V vs. Li/Li^+ from LMNOF-6060 and LMNOF-6368, despite the presence of carbonate species, indicates that increasing fluorination and the corresponding increase in Mn/Nb ratio plays some role in protecting or otherwise stabilizing carbonate-like species on the surface of DRX cathodes at high voltages.

3.4.4 Outgassing Comparison during Early Cycling

To monitor the extent and persistence of various important degradation reactions involving DRX materials, DEMS outgassing experiments were conducted during cycling of all three LMNOF materials for four full cycles. For these experiments, all materials were charged to an upper cut-off voltage of 4.8 V vs. Li/Li^+ and discharged to a lower cut-off voltage of 1.5 V vs. Li/Li^+. During cycling, the evolution of CO_2, O_2, and H_2 was monitored and quantified. To ensure that electrolyte depletion does not influence the interfacial degradation processes, a large excess of electrolyte (60 μL cm^{-2}) was used in all DEMS cells. The results of these experiments are displayed in Figure 3.4, and cycle-to-cycle cumulative gas evolution quantities are given in Table 3.3.

O_2 evolution is only observed to a very minor extent at the end of the first charge of LMNOF-4515. The lack of O_2 evolution from LMNOF-6060 and LMNOF-6368 indicates that increasing fluorine content suppresses O_2 evolution, a finding that is consistent with previous studies.[34,37] This observation is also supported by the bulk capacity analysis presented earlier in Section 3.4.2, which showed that increasing fluorination reduces the extent of bulk oxygen redox occurring in DRX materials. O_2 evolution occurs as a result of irreversible oxidation of the DRX oxyfluoride surface. Consequently, O_2 evolution is generally observed from lithium-excess oxide or oxyfluoride cathode materials at high states of delithiation wherein significant oxygen redox must occur. By reducing the extent to which the oxide lattice is oxidized during charging, fluorination also reduces the driving force for O_2 evolution. Furthermore, the lack of O_2 evolution from LMNOF-4515 on subsequent cycles indicates that the surface of the material forms a densified outer layer that passivates the material from additional O_2 evolution. A more detailed analysis of the O_2 evolution from the DRX materials is conducted in Section 3.6.4, in which the O_2 evolution during a constant current charge to an upper cut-off voltage of 4.8 V vs. Li/Li^+ followed by a long potentiostatic hold at the cut-off voltage is presented.

H_2 evolution is observed at potentials above 4.0 V vs. Li/Li^+ during high voltage cycling of all three DRX materials throughout all four cycles. Notably, more H_2 evolution is observed from the cells containing LMNOF-6060 and LMNOF-6368 than from the cell containing LMNOF-4515, and the amount of H_2 evolved tends to attenuate only slightly from cycle to cycle for each material. Significant H_2 evolution is not common during comparable cycling of other Mn- and Nb-containing DRX materials with the same electrolyte, eliminating the possibility that H_2 evolution occurs due to residual moisture in the electrolyte.[37] Instead, H_2 evolution is expected to arise from a three step process. First, high-voltage electrolyte oxidation at the DRX surface forms protic degradation products. Second, the

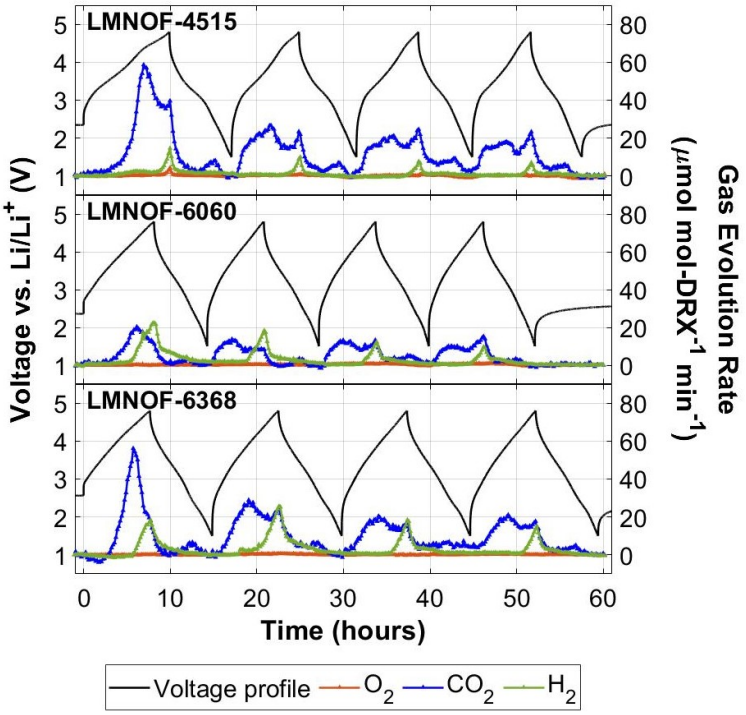

Figure 3.4: DEMS gas evolution results from LMNOF DRX materials during the first four cycles. Cycling consisted of charging to 4.8 V vs. Li/Li^+ and discharging to 1.5 V vs. Li/Li^+ at a constant current of 0.1 Li hr^{-1}. After the fourth cycle, the cells were allowed to rest on open circuit. The electrolyte was 1M $LiPF_6$ in 1:1 EC:DEC.

protic degradation products diffuse across the electrolyte to the anode surface. Third, the protic electrolyte degradation products are reduced at the anode surface to form H_2. Metzger et al. previously demonstrated the occurrence of this process with NMCs by using a specialized two-compartment DEMS cell to show that H_2 evolution does not occur when diffusion of protic species is blocked.[36] Additionally, several other studies have demonstrated that electrolyte oxidation leads to the formation of protic degradation products, supporting the proposed initial step of this process.[101–103] Moreover, the final step of this process is supported by experiments presented in Section 3.6.5, in which delithiated lithium iron phosphate was used in place of Li metal to show that no H_2 occurs when the counter-electrode potential is high enough to prohibit reduction of protic species. Although the nature of this protic electrolyte degradation product remains unclear, we suspect that either of the carbonate solvents in the electrolyte are oxidized to form some sort of organic species like an alcohol or carboxylic acid.

Given that H_2 evolution is not typically observed for other DRX materials, something characteristic to the materials studied herein must lead to elevated interfacial reactivity that

drives the formation of acidic electrolyte degradation products. The materials studied in this work were synthesized via high-energy ball milling to access extremely high levels of fluorination, potentially giving rise to surface damage and other defects or irregularities. In contrast, the DRX materials studied in previous reports in which H_2 was not observed were produced by conventional solid-state synthesis and possess much lower levels of fluorination (0-5%).[37,49] Based on this difference, we hypothesize that either the high fluorine content or the particle morphology and surface composition induced by the high-energy ball milling lead to an elevated interfacial reactivity for the materials studied herein, driving the electrolyte degradation processes underlying high-voltage H_2 evolution. This hypothesis is supported by the fact that both the fluorine content and the milling time were greater for LMNOF-6060 (30% F, 18 hours milling time) and LMNOF-6368 (33.75% F, 20 hours milling time) than for LMNOF-4515 (7.5% F, 10 hours milling time), potentially causing further elevated interfacial reactivity and explaining the increased H_2 evolution from the cells containing LMNOF-6060 and LMNOF-6368.[52] These results motivate further investigation of the effect of material synthesis and resulting particle morphology on interfacial reactivity. Finally, with regard to the slightly decreasing rates of H_2 evolution from cycle to cycle, it is likely that CEI formation and other modes of interfacial passivation cause the cathode surface becomes less reactive towards the electrolyte.

Finally, all three materials exhibit CO_2 evolution during all cycles. On the first charge, in the case of LMNOF-4515, the CO_2 evolution occurs in two separate peaks, the first reaching its maximum around 4.4 V vs. Li/Li^+ and the second reaching its maximum at 4.8 V vs. Li/Li^+ (end of charge). During the first charge of LMNOF-6060 and LMNOF-6368, on the other hand, only the first peak of CO_2 evolution at 4.4 V vs. Li/Li^+ is observed. As discussed previously in Section 3.4.3, the CO_2 evolution peak from all materials at 4.4 V vs. Li/Li^+ is likely caused by electrolyte degradation while the secondary CO_2 evolution peak from LMNOF-4515 at 4.8 V vs. Li/Li^+ is likely caused by surface carbonate decomposition. On subsequent charges, the CO_2 evolution profiles for all three materials exhibit a similar pattern featuring a broad peak around $\sim$4.4 V vs. Li/Li^+ and a sharp peak around 4.8 V vs. Li/Li^+, much like the CO_2 evolution from the first cycle of LMNOF-4515. Based on this similarity to the first cycle CO_2 evolution from LMNOF-4515, it is likely that the CO_2 evolution on subsequent charges from all three materials is driven by the same processes of lower-voltage ($\sim$4.4 V vs. Li/Li^+) electrolyte degradation and higher-voltage ($\sim$4.8 V vs. Li/Li^+) surface carbonate decomposition. Interestingly, the CO_2 evolution occurring at 4.8 V vs. Li/Li^+ attributed to surface carbonate decomposition regularly coincides with H_2 evolution for all three materials, suggesting that the acidic electrolyte degradation products that are reduced to form H_2 may also react at the cathode surface to decompose surface carbonate species. In addition to the CO_2 evolution observed during charging, a small amount of CO_2 evolution was also observed at the bottom of discharge ($<$3 V vs. Li/Li^+) for all three materials for each cycle. We note that this observation is surprising, as CO_2 is generally observed as a product of oxidative degradation at high voltages. While the processes underlying this CO_2 during discharge remain unknown, it is likely that the CO_2 originates from some type of electrolyte degradation. A follow-up study aims to further

investigate this low-voltage activity and its effect on cycling performance, and the results of the study will be summarized in a subsequent report. The cumulative amount of CO_2 evolved over all four cycles is significantly greater than the amount of native carbonate on the pristine sample for each material, as shown in Tables 3.2 and 3.3, indicating that the majority of the CO_2 must originate from the electrolyte. We note that electrolyte-originating CO_2 may still evolve due to solid carbonate decomposition, as electrolyte degradation appears to lead to the formation of solid carbonate species which may subsequently decompose to evolve CO_2. Finally, the total amount of CO_2 evolved during charge decreases from cycle to cycle for all three materials, suggesting a gradual attenuation in interfacial reactivity as the cathode surface becomes progressively more passivated.

Considering the effects of the observed degradation provides insight into the manner in which performance decay occurs in DRX cells. O_2 evolution leaves behind an oxygen-depleted, cation-densified outer layer that cannot be re-intercalated and instead creates a barrier to Li transport.[34,65] The processes that underlie H_2 evolution cause both electrolyte depletion and formation of acidic species that may degrade other cell components. For example, acidic species formed at the cathode surface may drive secondary degradation processes like dissolution of transition metals, hydrolysis of $LiPF_6$, reaction with the separator, and decomposition of passivating species like Li_2CO_3 and LiF on the surface of either electrode.[43,78,102,104] Finally, the electrolyte degradation process resulting in CO_2 evolution inevitably leads to depletion of the electrolyte and deposition of insulating degradation products on the cathode surface.[27,49]

3.4.5 Fluoride-Scavenging DEMS Analysis of Fluorine Dissolution

Another interfacial degradation process of great importance is dissolution of DRX-originating fluorine at the cathode-electrolyte interface. Previous studies have shown that lattice fluorine dissolves from the surface at high voltages.[37] To learn more about the fluorine dissolution process, a modified DEMS technique was used to monitor in-situ the dissolution of DRX-originating fluorine into the electrolyte. By allowing the detection and quantification of gaseous species formed by any reaction occurring within the cell, DEMS can be paired with various additives that drive gas-evolving reactions to provide indirect measurements of the formation of non-gaseous species. Tris(trimethylsilyl) phosphate (TMSPa) is an electrolyte additive that will react with dissolved fluoride ions to yield gaseous trimethylsilyl fluoride (Me_3SiF), which can then be detected and measured using DEMS.[75,76] TMSPa reacts very slowly with solid fluorides, but it reacts much more rapidly with dissolved fluoride in the electrolyte.[95] Furthermore, TMSPa will not abstract fluorine from other fluorine-containing species (i.e. $LiPF_6$, LiTFSI, PVDF) to produce Me_3SiF.[76] Based on these characteristics, we assume that significant Me_3SiF evolution arises only from reaction of TMSPa with dissolved fluoride ions in the electrolyte. Therefore, when DEMS experiments are conducted with electrolyte containing TMSPa, Me_3SiF evolution can be monitored in-situ as a signal to

represent the formation of dissolved fluoride in the electrolyte. This technique, referred to as fluoride-scavenging DEMS, has been used in previous studies to study dissolved fluoride formation originating from both electrolytes and oxyfluoride cathode materials.[37,75,76]

While Me_3SiF evolution measured by fluoride-scavenging DEMS signals the formation of dissolved fluoride species in the electrolyte, additional steps must be taken to exclusively study fluorine dissolution from DRX materials. As previously mentioned, TMSPa will react with dissolved fluoride species (i.e. LiF, HF) in the electrolyte. Consequently, fluoride species formed via degradation of commonly used cell components like $LiPF_6$ salt and polyvinylidene fluoride (PVDF) binder may contribute to any observed Me_3SiF during fluoride-scavenging DEMS. To study the dissolution of DRX-originating fluorine exclusively, all other potential sources of fluoride must therefore be eliminated from the cell. For the fluoride-scavenging DEMS experiments conducted in this section, the PVDF cathode binder was replaced with polyethylene (PE) and the $LiPF_6$ electrolyte salt was replaced with LiTFSI. We note that while LiTFSI still contains fluorine, it does not degrade to form fluoride to any significant extent. Indeed, control experiments in which a fluorine-free TMO cathode material material is charged in LiTFSI-based electrolyte with TMSPa reveal no significant Me_3SiF evolution, as shown and discussed in Section 3.6.6. We therefore conclude that any Me_3SiF evolution observed from cells containing DRX cathodes with PE binder and electrolyte with LiTFSI salt must come from DRX-originating fluorine, allowing us to exclusively study fluorine dissolution from the DRX material.

To study fluorine dissolution from the set of DRX materials during early cycling, fluoride-scavenging DEMS was conducted for all three materials during the first three cycles with cells containing the aforementioned fluorine-free components. All cathodes were charged to an upper cut-off voltage of 4.8 V vs. Li/Li^+ and discharged to a lower cut-off voltage of 1.5 V vs. Li/Li^+ at a constant current rate of 0.1 Li hr^{-1}. After each discharge, the cells were allowed to rest on open circuit for three hours to allow complete evacuation of the gases remaining in the headspace before the next cycle. The results of the fluoride-scavenging DEMS experiment for each DRX material, including the voltage profile and the gas evolution profiles of Me_3SiF and H_2, are shown in Figure 3.5. We include H_2 here given the general coincidence of $mathrmMe_3SiF$ and H_2 evolution. As explained, the observed Me_3SiF evolution serves as an in-situ signal for dissolution of DRX-originating fluorine into the electrolyte. Very little Me_3SiF evolution is observed from LMNOF-4515 throughout all three cycles. In contrast, significant Me_3SiF evolution during cycling of both LMNOF-6060 and LMNOF-6368 occurs during charging above ~4.3 V vs. Li/Li^+ and reaches a maximum at the end of charge (4.8 V vs. Li/Li^+). Furthermore, the amount of Me_3SiF evolved decreases from cycle to cycle. These results show that the dissolution of DRX-originating fluorine occurs from the surface of both LMNOF-6060 and LMNOF-6368, whereas very little fluorine dissolution takes place from the surface of LMNOF-4515. The attenuation in fluorine dissolution from LMNOF-6060 and LMNOF-6368 over cycling, demonstrated by the decreasing extent of Me_3SiF evolution, suggests that a fluorine-depleted region gradually forms near the surface of LMNOF-6060 and LMNOF-6368 during the first few cycles. This fluorine-depleted region is likely to passivate the DRX materials from further fluorine dissolution. The cumulative amounts of Me_3SiF

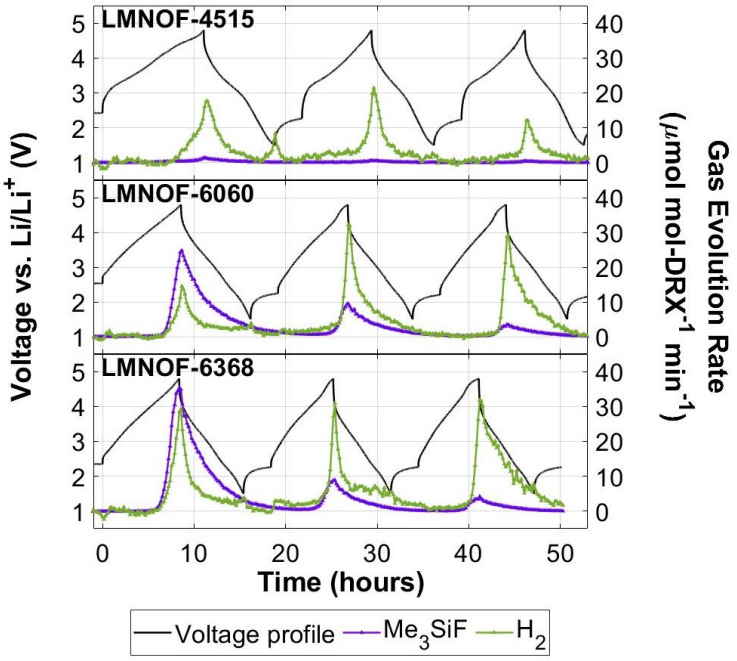

Figure 3.5: Fluoride-scavenging DEMS results from LMNOF DRX materials during the first three cycles. Each cycle consisted of charging to 4.8 V vs. Li/Li^+ and discharging to 1.5 V vs. Li/Li^+ at a constant current of 0.1 Li hr^{-1}. After each discharge, the cells were allowed to rest on open circuit for 3 hours. The electrolyte was 1M LiTFSI in 1:1 EC:DEC with 1vol% TMSPa.

evolved for each material and the corresponding fraction of DRX fluorine dissolved are given in Table 3.4. Importantly, for both LMNOF-6060 and LMNOF-6368, the amount of fluorine dissolved during the first cycle amounts to about 1-2% of the fluorine contained within the DRX material.

The voltage dependence of fluorine dissolution process indicates that the underlying reaction is electrochemical in nature. This observation is further supported by the very low solubility of species like LiF in carbonate solvents, suggesting that some sort of electrochemically-driven process must assist in the dissolution of surface-bound fluorine.[105] The dissolution of surface-bound fluorine species may be activated by the electrochemical formation of other reactive intermediate species. Interestingly, the evolution of Me_3SiF shown in Figure 3.5 appears to generally coincide with H_2 evolution. Most notably, the onsets of Me_3SiF evolution and H_2 evolution occur very closely to one another for LMNOF-6060 and LMNOF-6368 for each cycle. As explained earlier, H_2 evolution occurs due to the formation of protic electrolyte degradation products on the surface of the cathode and subsequent reduction of the protic species to form H_2 at the Li metal anode. Based on these observations, one possible explanation for the electrochemical dependence of fluorine dissolution and the enhanced sol-

ubility of the fluoride species in the electrolyte is that reactive acidic electrolyte degradation products assist in the dissolution of surface-bound fluorine. Previous studies have shown the role of acidic species in driving dissolution of TMO cathode materials, wherein protic species abstract oxide to form water as well as dissolved lithium and/or transition metals.[104,106,107] An analogous reaction, in which protons or protic species abstract surface fluorine to form HF and dissolved lithium and/or transition metals, could be the process underlying the observed fluorine dissolution. Surface dissolution in this manner would inevitably lead to a loss of cathode capacity and may also lead to subsequent reaction of dissolved fluoride species (i.e. HF) with other cell components. This observation provides an important example of how initial electrolyte degradation may cause a cascade of subsequent degradation reactions via the formation of reactive intermediate species like protic electrolyte degradation products.

While the extent of fluorine dissolution does appear to trend with the fluorine content of the DRX material, the stark contrast between the fluorine dissolution from LMNOF-4515 and that from LMNOF-6060 and LMNOF-6368 suggests that the trend is not linear with bulk fluorine content. This strong difference suggests that there is a heightened reactivity of the surface fluorine in the case of LMNOF-6060 and LMNOF-6368, which may indicate the existence of a threshold value for the fluorine content below which the fluorine is largely stable on the DRX surface. Another possible explanation for this elevated reactivity is that the increasing Mn content and decreasing Nb content associated with increasing fluorination lowers the stability of fluorine on the DRX surface. Finally, another alternative explanation is that the extended milling times required to synthesize LMNOF-6060 (18 hours) and LMNOF-6368 (20 hours) relative to that of LMNOF-4515 (10 hours) induces additional surface damage and smaller particle size, leading to more fluorine dissolution from the DRX material.

3.4.6 ICP-OES Analysis of Mn Dissolution

The outgassing observed during cycling of DRX materials demonstrates the various degradation modes that take place at the cathode-electrolyte interface. In particular, the evolution of H_2 indicates that acidic electrolyte degradation products are formed at the cathode surface, as explained in the previous sections. Manganese dissolution is a process known to occur from TMO materials like spinel $LiMn_2O_4$ at high voltages, and many studies have indicated that acidic species formed by high-voltage electrolyte degradation actively drive manganese dissolution. Many of these studies also suggest that Mn dissolves as Mn^{2+}, often first requiring disproportionation of Mn^{3+} to Mn^{2+} and Mn^{4+} or reduction of Mn^{3+} or Mn^{4+} by electrolyte degradation products.[106–108] Once dissolved, the manganese species are likely to either remain dissolved in the electrolyte or migrate across the electrolyte and deposit on the anode.[104] To further investigate the dissolution processes occurring at the DRX surface, ICP-OES was used to quantify manganese species dissolved in the electrolyte or deposited on the surface of the Li metal counter-electrodes used during the first charge of the DRX cathodes. Since no other cell components contain manganese, any manganese detected by ICP-OES must be a product of dissolution from the DRX surface.

For each DRX material, the amount of Mn dissolved from the cathode was quantified after three different procedures: rest at open circuit (OCV), charge to 4.0 V vs. Li/Li^+ (4.0 V), and charge to 4.8 V vs. Li/Li^+ (4.8 V). For the OCV procedure, the cell was simply allowed to rest at open circuit for 24 hours. For the two charge procedures, charging consisted of a constant current charge at 0.1 Li hr^{-1} to the selected cut-off voltage followed by a potentiostatic hold at the cut-off voltage until the current decayed to 0.01 Li hr^{-1}. To control cathode-electrolyte contact time across different procedures, the charged cells were allowed to rest at open circuit until the total time in contact with the electrolyte was 24 hours. For each sample, a propagation of uncertainty analysis was carried out to estimate the error in the calculated amount of Mn dissolution, which results from uncertainty in the cathode loading and the ICP-OES measurement. The results of the Mn dissolution study and corresponding propagation of uncertainty analysis are shown in Figure 3.6. For both LMNOF-4515 and LMNOF-6060, a small amount of Mn dissolution was detected for all three procedures, in each case amounting to approximately 0.1% of the Mn contained in the DRX material In contrast, for LMNOF-6368, a growing amount of Mn dissolution is observed with increasing cut-off voltage. Slightly more Mn dissolution is observed from LMNOF-6368 in the 4.0 V sample (0.68 mmol-Mn mol-DRX^{-1}, ∼0.1% of DRX Mn) than in the OCV sample (0.53 mmol-Mn mol-DRX^{-1}, ∼0.08% of DRX Mn), and significantly greater Mn dissolution is observed in the 4.8 V sample (3.7 mmol-Mn mol-DRX^{-1}, ∼0.6% of DRX Mn).

The small amount of Mn that dissolves from all three materials without any charging may be due to the dissolution of Mn^{2+} species from the DRX surface into the electrolyte in very small quantities. Further, the dramatic increase in Mn dissolution observed from the LMNOF-6368 sample charged to 4.8 V vs. Li/Li^+ suggests that an additional Mn dissolution process sets in during charging of LMNOF-6368 above 4.0 V vs. Li/Li^+. The occurrence of additional manganese dissolution from LMNOF-6368 during charging above 4.0 V vs. Li/Li^+ and lack thereof from LMNOF-4515 and LMNOF-6060 indicates that increasing fluorination and the corresponding shift in Mn/Nb content creates conditions under which Mn dissolution can occur. Given that comparable amounts of H_2 evolution were detected during cycling of all three materials, it is unlikely that this additional high-voltage Mn dissolution from LMNOF-6368 is caused by an increased amount of acidic electrolyte degradation products reacting with the DRX surface. Furthermore, given that the average Mn oxidation state at the end of charge is shown in Figure 3.2 to be very similar in LMNOF-6060 and LMNOF-6368, it is unlikely that the differences in Mn dissolution are caused by a difference in Mn oxidation state between the three materials. As such, the exact cause for the additional Mn dissolution from LMNOF-6368 remains unclear, motivating a more detailed investigation of Mn dissolution from DRX materials.

These results provide an important example of how material composition can influence susceptibility towards high-voltage surface dissolution processes. In addition to causing a direct loss of cathode capacity, Mn dissolution is also likely to result in deleterious reaction of dissolved Mn ions at the anode surface, causing additional degradation and loss in cell capacity.[104] The compounded negative consequences associated with Mn dissolution during high voltage cycling thus make it an important process to study further.

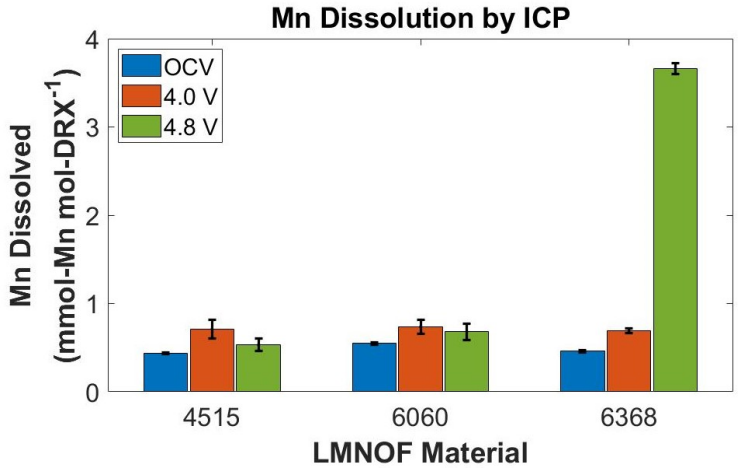

Figure 3.6: Amount of Mn dissolved from LMNOF materials after an open circuit rest period in the electrolyte (OCV), upon charge to 4.0 V vs. Li/Li^+ (4.0 V), and upon charge to 4.8 V vs. Li/Li^+ (4.8 V). Charging consisted of a constant current charge at 0.1 Li hr^{-1} to the selected cut-off voltage followed by a potentiostatic hold at the cut-off voltage until the current decayed to 0.01 Li hr^{-1}. The electrolyte was 1M $LiPF_6$ in 1:1 EC:DEC. To control for cathode-electrolyte contact time, all cathodes spent 24 hours in the cell. Error bars are obtained from a propagation of uncertainty analysis to estimate the error contributed by uncertainty in the cathode loading and the ICP-OES measurement.

3.4.7 XPS Analysis of Cathode Surface Composition

To further investigate the observed interfacial degradation, XPS was used to study the surface composition of DRX cathodes before and after the first charge to 4.8 V vs. Li/Li^+. For each material, the F1s and O1s XPS spectra were measured for both a pristine DRX cathode and a DRX cathode charged to 4.8 V vs. Li/Li^+. For each material, charging consisted of a constant current charge at 0.1 Li hr^{-1} to 4.8 V vs. Li/Li^+ followed by a potentiostatic hold at 4.8 V vs. Li/Li^+ until the current decayed to 0.01 Li hr^{-1}. After charging, the DRX cathodes were harvested from their cells in an Ar-filled glovebox, rinsed with DEC, dried overnight under vacuum, and stored under Ar until XPS analysis. We acknowledge that our set of samples does not allow for the discernment of changes caused by contact with the electrolyte under rest conditions or by extended cycling. Further experimentation examining the surface composition of DRX samples after various extents of electrolyte exposure and electrochemical cycling may provide more detailed information about DRX surface transformation.

O1s XPS

The O1s XPS spectra for all three materials before and after charging are shown in Figure 3.7a. All O1s spectra contain three adjacent peaks. The highest energy peak, shown in blue,

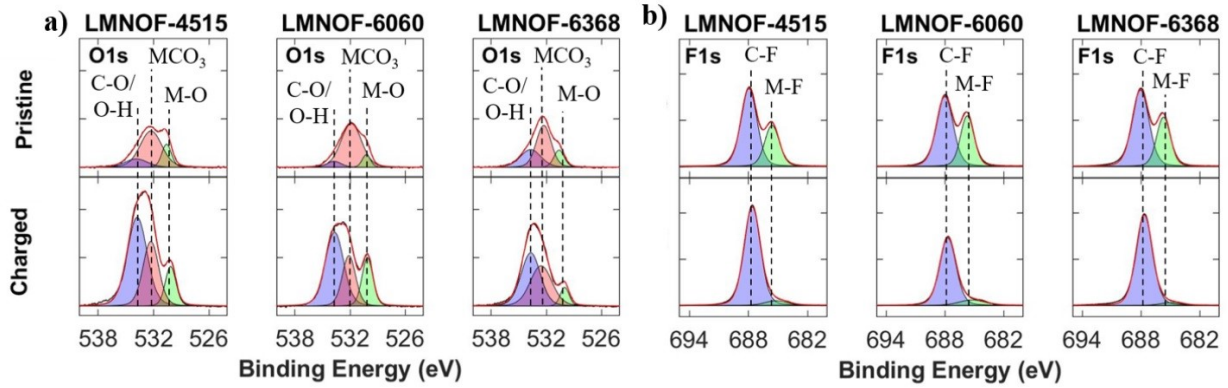

Figure 3.7: O1s (a) and F1s (b) XPS spectra from LMNOF pristine (top) and charged (bottom) cathodes. Charging consisted of a constant current charge at 0.1 Li hr^{-1} to 4.8 V vs. Li/Li^+, followed by a potentiostatic hold at 4.8 V vs. Li/Li^+ until the current decayed to 0.01 Li hr^{-1}. The electrolyte was 1M $LiPF_6$ in 1:1 EC:DEC. After charging, the cathodes were harvested from their cells in an Ar-filled glovebox, rinsed in DEC to remove residual electrolyte, dried under vacuum overnight, and stored under Ar until XPS analysis.

is assigned to either organic C-O groups originating from electrolyte degradation products or O-H groups originating from impurity species like LiOH and $LiHCO_3$. The middle peak, shown in red, is assigned to metal carbonate (MCO3) species like Li_2CO_3 or $MnCO_3$. Finally, the low energy peak, shown in green, is ascribed to the metal-oxygen (M-O) bonds in the DRX lattice. These peak assignments are consistent with those of several previous studies.[109,110] Before charging, the pristine cathodes have small contributions from the C-O/O-H peak and the M-O peak, and the largest contribution is from the MCO_3 peak. This measurement suggests that the pristine cathode surface is initially dominated by metal carbonate species, although these carbonates do not completely cover the DRX surface such that the M-O signal from the DRX lattice is also observed. The small contribution from the C-O/O-H peak before charging (and before exposure to electrolyte) may originate from the O-H bonds in trace impurity species like LiOH or $LiHCO_3$. After charging, the O1s spectra is instead dominated by the C-O/O-H peak, whereas the metal carbonate peak and the metal oxide peak have smaller but still detectable contributions. The growth of the C-O/O-H peak is likely to be caused by deposition of solvent-derived electrolyte degradation products containing C-O bonds on the DRX surface during charging, while the decrease in signal from the metal carbonate species suggests that native metal carbonate species are partially decomposed. The deposition of these solvent-derived electrolyte degradation products during charging is consistent with the extensive electrolyte degradation observed earlier by DEMS (Section 3.4.4). Furthermore, the partial but incomplete decomposition of the metal carbonate species agrees with the findings of the carbonate decomposition studies conducted using DEMS and TiMS (Section 3.4.3), demonstrating that some metal carbonate species remain

after the first charge. Finally, the retained signal from the M-O peak after charging indicates that the metal oxide of the DRX lattice is not completely buried by the cathode-electrolyte interface (CEI) layer. These results demonstrate the transformation of the DRX surface during initial cycling, which consists of the decomposition of native interfacial species and the deposition of electrolyte-derived degradation products. Given the consistency of these results with the outgassing observed over several cycles by DEMS, we expect that these electrolyte degradation processes continue during extended cycling and are therefore representative of the interfacial reactivity that contributes to long-term performance decay.

F1s XPS

The F1s XPS spectra for all three materials before and after charging, all of which contain two adjacent peaks, are shown in Figure 3.7b. The higher-energy peak, shown in blue in each spectrum, is attributed to the C-F groups in the PVDF binder.[111] Meanwhile, the lower-energy peak, shown in green in each spectrum, is attributed to metal-fluorine (M-F) bonds in the DRX lattice.[112,113] For all three materials, the M-F peak stands out clearly in the pristine sample. In contrast, the M-F peak for all three charged samples is faint, suggesting a decrease in fluorine content near the surface of the DRX materials. The decrease in M-F species after the first charge indicates that a loss of fluorine occurs and/or a thick fluorine-free CEI layer is deposited on the surface of the DRX material. Based on the retained signal from the DRX lattice oxide in the O1s spectra after charging, the CEI layer is not expected to be thick enough to fully mask the signal from the DRX anion lattice underneath. Consequently, the disappearance of the M-F peak in the F1s spectra for all three materials is likely to be caused by a loss of fluorine from the DRX surface during the first charge, consistent with the dissolution of DRX originating fluorine observed in the fluoride-scavenging DEMS experiments. It is important to note that the difference in magnitude of fluorine dissolution between materials observed in the fluoride-scavenging DEMS experiments is not captured by these XPS experiments, which show similar extents of fluorine loss for all three materials. This discrepancy is likely to be caused by the fact that the fluoride-scavenging DEMS cells employed a LiTFSI-based electrolyte whereas the cells used for to prepare the cathodes for XPS employed a $LiPF_6$-based electrolyte. As documented in previous reports and demonstrated further in Section 3.6.8, high-voltage cycling with a $LiPF_6$-based electrolyte may result in elevated dissolution of DRX-originating fluorine relative to comparable cycling in a LiTFSI-based electrolyte.[37] The elevated degradation in $LiPF_6$-based electrolyte is likely to be driven by the tendency of the salt anion to form reactive species like HF that are in turn capable of causing DRX dissolution. It is therefore likely that the thickness of the outer fluorine-depleted region formed on the surface of all three DRX materials when cycled in $LiPF_6$-based electrolyte approaches or exceeds the penetration depth of the XPS, causing the M-F peak to nearly disappear for each material. This result highlights the utility of the fluoride-scavenging DEMS results, in which more fluoride dissolution is clearly observed with increasing DRX fluorination.

3.4.8 Solid State NMR of DRX Materials

To further characterize the composition of the DRX cathode materials before and after charging, ^{7}Li and ^{19}F NMR spectra were recorded on LMNOF-4515, LMNOF-6060, and LMNOF-6368 electrodes in the pristine state and after charging to 4.8 V vs. Li/Li^{+}. For all three materials, charging consisted of a constant current charge at 0.1 Li hr^{-1} to 4.8 V vs. Li/Li^{+} followed by a potentiostatic hold at 4.8 V vs. Li/Li^{+} until the current decayed to 0.01 Li hr^{-1} (Figures 3.14 and 3.15, respectively).

^{7}Li NMR

^{7}Li NMR spectra show across all samples a broad and asymmetric line shape spanning a frequency range from 500 to -200 ppm with spinning sidebands on both sides (Figure 3.14). This broad line shape is attributed to the various local Li environments found within the disordered structure of LMNOF electrodes. This attribution is further supported by the fully isotropic ^{7}Li spectrum (projected magic angle turning phase adjusted sideband separation, pj-MATPASS, in grey shadings in Figure 3.14) that highlights a distribution of Li chemical shifts and environments in each LMNOF electrode.

No significant line shape difference is found across pristine electrodes, indicating a similar Li distribution in all pristine compositions. On the other hand, when comparing pristine electrodes to their charged counterparts, the latter exhibit a significant decrease in the overall ^{7}Li signal intensity along with a slight increase in line width (around 60 ppm wider). The decrease in ^{7}Li signal intensity is in line with extraction of Li ions during charge. The slight increase in line width can be attributed to (i) an increase in Li disordering within the DRX structure due to prolonged Li extraction and/or (ii) a modification of the paramagnetic interaction between Mn unpaired electron and ^{7}Li nuclear spin due to the oxidation of Mn ions.

Finally, no sharp signal with an extensive sideband pattern centered at 0 ppm can be observed in the ^{7}Li NMR spectrum, indicating that no significant amount (less than a few percent by weight) of Li-based diamagnetic impurities (e.g. LiF or Li_2CO_3) can be detected in these LMNOF electrodes by NMR. This finding is consistent with the amounts of surface carbonate species as measured by acid titration, which are consistently in the range of 1-2% by weight (see carbonate titration results for pristine materials in Figure 3.3). Furthermore, the minimal amount of Li-based diamagnetic impurities further supports the assumed composition of the ball-milled DRX materials.

^{19}F NMR

The ^{19}F NMR spectra of pristine LMNOF electrodes are composed of two signals centered around –95 ppm and –190 ppm along with their spinning sidebands on both sides (Figures 3.8 and 3.15, Pristine). Since no sharp signal can be detected standing out from the broader DRX signal at –204 ppm, these materials do not contain significant quantities of residual LiF used in the synthesis of LMNOF materials.

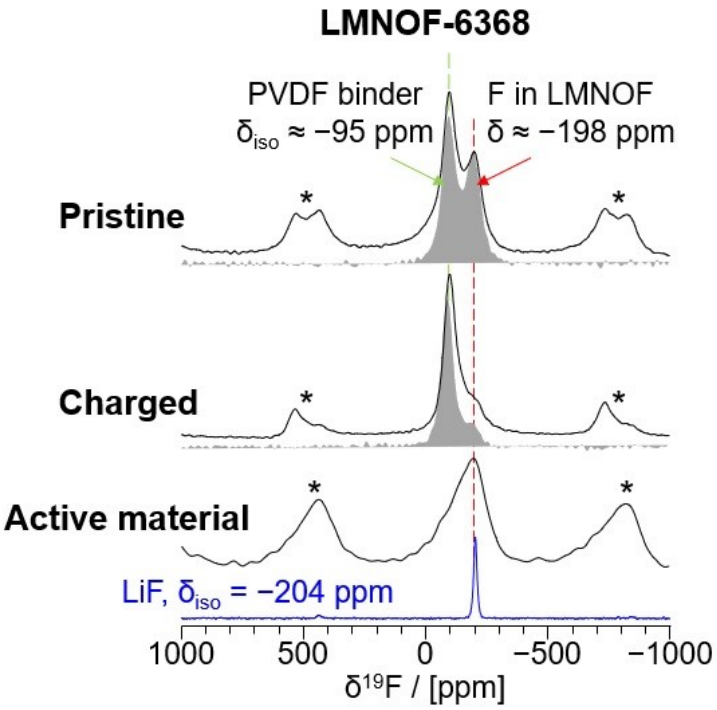

Figure 3.8: ^{19}F NMR spectra (spin echoes in black and isotropic spectra obtained using the pj-MATPASS sequence in grey shading) recorded on pristine and charged LMNOF-6368 electrodes.[96,97] For the charged sample, charging consisted of a constant current charge at 0.1 Li hr^{-1} to 4.8 V vs. Li/Li$^+$ followed by a potentiostatic hold at 4.8 V vs. Li/Li$^+$ until the current decayed to 0.01 Li hr^{-1}. The electrolyte was 1M $LiPF_6$ in 1:1 EC:DEC. ^{19}F spin-echoes of carbon-coated LMNOF-6368 active material without PVDF binder and pure LiF (δ_{iso} = -204 ppm, in blue) are also shown for comparison with LMNOF-6368 electrodes. Spinning sidebands are indicated with asterisks. The isotropic chemical shift of the PVDF binder is highlighted at $\delta_{iso} \sim$ -95 ppm with a green dashed line. The most intense ^{19}F signal coming from F^- ions in the LMNOF-6368 structure is highlighted with a red dashed line along with its observed chemical shift $\delta \sim$ -198 ppm. The intensity of LMNOF electrodes ^{19}F spectra was normalized so that the PVDF signal of each spectrum reaches the same intensity.

The most intense signal at –95 ppm is attributed to the main resonance of -CF_2- in PVDF polymer used as a binder in the LMNOF electrodes.[114] It is worth mentioning that in the LMNOF electrodes, the PVDF signal observed at –95 ppm is overlapping with a significant portion of the LMNOF line shape and only part of the DRX ^{19}F resonance remains visible around –190 ppm (see ^{19}F spectrum of Pristine sample in Figure 3.8). A ^{19}F spin-echo spectrum recorded on the carbon-coated LMNOF-6368 active material (without PVDF binder) is also shown in Figure 3.8 (Active Material sample). Here, a wide and asymmetric ^{19}F line shape is visible, spanning a wide frequency range from 100 to –400 ppm along with spinning sidebands on both sides. This line shape is due to the various local F environments found in the disordered structure of LMNOF electrodes and proves the successful integration of F ions within the DRX structure.

Even though the PVDF signal overlaps with a large portion of the ^{19}F LMNOF electrodes line shape, the ^{19}F signal around –190 ppm can still be used to track the evolution of F^- ions within the LMNOF electrodes before and after a prolonged charge at 4.8 V vs. Li/Li^+. Since each LMNOF electrode was prepared with the same ratio of active material to binder (60:10 wt:wt), the intensity of the PVDF ^{19}F signal can be used as an internal reference to normalize the intensity of all ^{19}F spectra (Figure 3.8, Pristine and Charged, and Figure 3.15). It is clear that the intensity of the –190 ppm signal increases with the amount of F in the pristine LMNOF cathodes (Figure 3.15). Furthermore, as the intensity of the signal for F^- ions within the LMNOF structure increases, the observed chemical shift associated with the F^- ions evolves from –175 ppm (LMNOF-4515) to –185 ppm (LMNOF-6060) and ends up at –198 ppm (LMNOF-6368). This evolution of the ^{19}F chemical shift tends to indicate the formation of larger LiF-rich domains within the LMNOF structure upon increasing fluorine content. As the size of these Li F-rich domains increases, the observed chemical shift moves closer and closer to the isotropic shift of pure LiF at –204 ppm.

After charging, the intensity of the cathode signals centered at about –190 ppm significantly decreases when compared to the –190 ppm signal intensity observed in the spectra collected on the pristine electrodes (Figures 3.8 and 3.15). This signal decay upon charging is particularly pronounced for LMNOF-6368 (Figure 3.8). This change can be explained by either some loss of F^- ions from LiF-rich domains of the DRX structure as Li gets extracted or by cation rearrangements resulting in a greater number of Mn-F bonds in the charged cathode. In the latter case, the strong paramagnetic interactions between ^{19}F nuclei and unpaired electrons from the Mn ions lead to a significantly broader and short-lived ^{19}F NMR signal that is impossible to observe experimentally, resulting in an effective reduction in ^{19}F NMR signal intensity. Finally, after charging, the LMNOF-4515 has the least amount of F^- ions left within the DRX structure. LMNOF-6060 and LMNOF-6368 still exhibit a small signal around –190 ppm, with the intensity in LMNOF-6368 being the highest. These observations are in line with the fluorine losses observed earlier by in-situ fluoride-scavenging DEMS and ex-situ XPS, supporting the observation that significant dissolution of lattice fluorine occurs during high-voltage charging.

3.5 Conclusions

In this work, TiMS was employed to decouple the capacities contributed by $Mn^{2+/4+}$ and oxygen redox during the first charge. This analysis revealed that increasing DRX fluorination from 7.5% to 33.75% deactivates bulk oxygen redox, leaving only $Mn^{2+/4+}$ redox to provide the entirety of the bulk charge compensation. In this context, changing the fluorine content can be seen as a way to tune the extent to which $Mn^{2+/4+}$ and oxygen redox contribute to bulk charge compensation. TiMS was also paired with DEMS to reveal that while all three materials undergo low-voltage (∼4.4 V vs. Li/Li^+) electrolyte degradation during the first charge, only LMNOF-4515 exhibits a high-voltage (∼4.8 V vs. Li/Li^+) surface carbonate decomposition. The DEMS analysis was then extended over the first four cycles to show that O_2 evolution occurs only on the first charge of LMNOF-4515, confirming previous findings that fluorination suppresses high-voltage O_2 evolution. These DEMS experiments also showed that CO_2 and H_2 evolution occur for all three materials to diminishing extents over all four cycles, indicating that multiple routes of degradation associated with high-voltage oxidative electrolyte decomposition occur at the DRX surface. Next, a fluoride-scavenging electrolyte additive was introduced into the DEMS cell, revealing in-situ the dissolution of DRX-originating fluorine from LMNOF-6060 and LMNOF-6368 at high voltages. Finally, ICP-OES, XPS, and SS-NMR were used to demonstrate the occurrence of several changes in DRX composition during charging, including manganese and fluorine dissolution as well as solid organic carbonate deposition.

The results of this study highlight the effects of DRX composition on bulk electrochemistry and interfacial reactivity, ultimately informing material performance in both the short- and long-term. The observed trends indicate that increasing fluorination will suppress oxygen redox, leaving $Mn^{2+/4+}$ redox to provide the majority of bulk charge compensation during cycling. At the same time, increasing fluorination is likely to lead to decreased evolution of O_2 and increased dissolution of Mn and fluorine at high voltages. These observations point to a moderate DRX composition, with fluorine content between that of LMNOF-4515 and LMNOF-6060 (∼10-30%), that may have the optimal compromise of these effects. Furthermore, the occurrence of rarely seen electrolyte degradation processes like high-voltage H_2 evolution and CO_2 evolution near the lower cut-off voltage during discharge motivates investigation of the high-energy ball-milling DRX synthesis and its effect on interfacial reactivity. Inevitably, the high reactivity brought about by accessing high-voltage redox processes with DRX cathode materials necessitates the development of a cathode-electrolyte interface with improved oxidative stability. Potentially promising routes towards achieving a more stable interface include developing electrolytes with increased resistance towards oxidative degradation as well as passivating the surface of DRX materials via coating or washing.

3.6 Supplementary Information

3.6.1 Ex-situ Acid Titration Chemistry

Understanding the chemical reactions that take place during acid titration is crucial for properly interpreting the titration results. There are two primary chemical reactions that occur in the titration solution: carbonate decomposition and oxygen disproportionation. Carbonate decomposition produces CO_2 via the acid-mediated decomposition of surface carbonate species, including either lithium carbonate or organic carbonate-like electrolyte degradation products. The stoichiometry underlying carbonate decomposition is described in Equation 3.1. Using this reaction stoichiometry, the amount of surface carbonate species can be calculated from the measured amount of CO_2 gas evolved during acid titration.

$$CO^{2-}_{3,\,(s)} + 2H^{+}_{(aq)} \rightarrow CO_{2,\,(g)} + H_2O_{(l)} \tag{3.1}$$

Meanwhile, oxygen disproportionation is the solution-state disproportionation of oxidized oxygen species into O_2 gas and H_2O. To understand how the stoichiometry underlying the oxygen disproportionation reaction can be used to interpret O_2 evolution measured by TiMS, two reactions must be considered. The first reaction that must be considered is the reaction in which the oxide lattice is electrochemically oxidized during charging to form oxidized oxygen species, as described in Equation 3.2. The form of the oxidized oxygen species is left generalized in this framework as the product of an n-electron oxidation to demonstrate the applicability of this technique to various or ambiguous forms of oxidized oxygen.

$$O^{2-}_{\text{lattice}} \rightarrow O^{(2-n)-}_{\text{lattice}} + n\ e^- \tag{3.2}$$

The second reaction that must be considered to interpret O_2 evolution measured by TiMS is the solution-state disproportionation of oxidized species to form O_2 gas and H_2O, as shown in Equation 3.3. The disproportionation reaction is thermodynamically driven by the increased stability of oxygen in the 0 and -2 oxidation states, relative to any intermediate value between 0 and -2. Upon dissolution into the acid medium, any oxidized oxygen species with an intermediate oxidation state between 0 and -2 will react amongst themselves to reach these more stable end-member oxidation states while maintaining electroneutrality. We note that this reaction occurs with selectivity relative to other solution-based redox reactions, which we ascribe to the close match in frontier orbital energy and symmetry.

$$O^{(2-n)-}_{\text{lattice}} + (2-n)H^{+}_{(aq)} \rightarrow \frac{n}{4}O_{2,\,(g)} + \frac{2-n}{2}H_2O_{(l)} \tag{3.3}$$

Last, the ratio of O_2 evolved to electrons extracted via oxygen redox can be calculated using the framework set out above, as done in Equation 3.4. This ratio is shown to be 4 e^-/O_2 and is therefore independent of the form of oxidized oxygen species present.

$$\frac{\text{Electrons Extracted}}{O_2\text{ Evolved}} = \frac{(n\ e^-)}{n/4\ O_2} = 4\ \frac{e^-}{O_2} \tag{3.4}$$

3.6.2 Cumulative CO_2 Evolution and Surface Carbonate Quantities

The surface carbonate analysis in Section 3.4.3 of the main text presented titration results for all three DRX materials. For each material, the titration samples consisted of a pristine cathode and cathodes extracted after charging with DEMS to 4.4 V vs. Li/Li^+, 4.6 V vs. Li/Li^+, and 4.8 V vs. Li/Li^+. The CO_2 evolution results obtained during charging of each material to 4.4 V vs. Li/Li^+ and 4.6 V vs. Li/Li^+ are shown in Figure 3.9. Additionally, the integrated amounts of CO_2 evolved from each DEMS experiment are included in Table 3.1, and the amounts of carbonate measured by TiMS for each sample are included in Table 3.2.

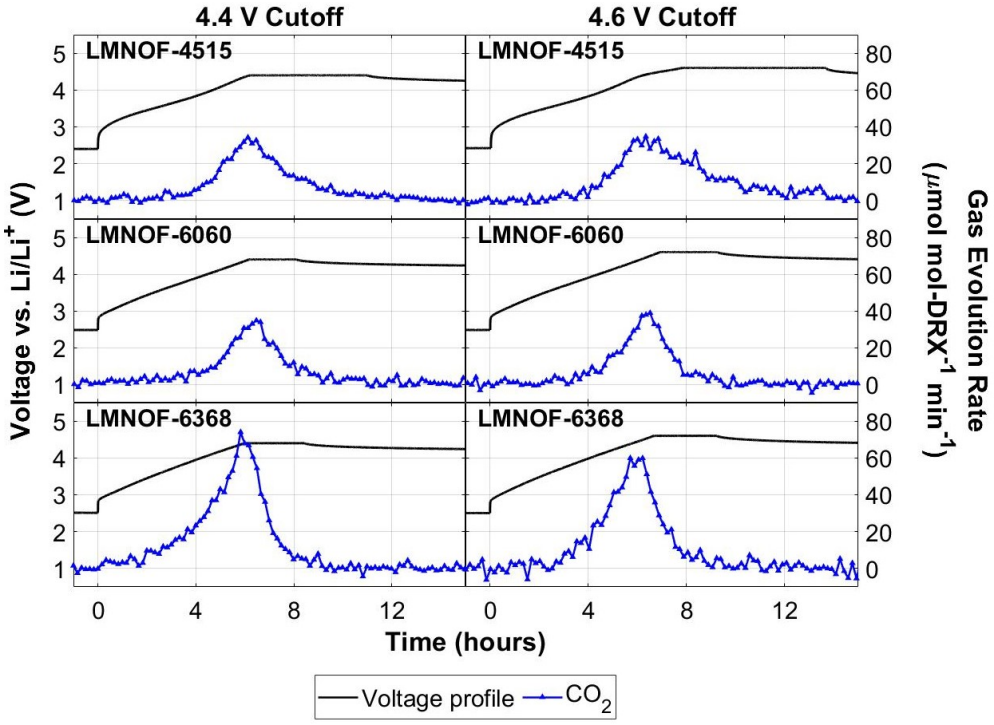

Figure 3.9: CO_2 evolution from LMNOF DRX materials during charge to 4.4 V vs. Li/Li^+ (left) and 4.6 V vs. Li/Li^+ (right). Charging consisted of a constant current charge at 0.1 Li hr^{-1} to the listed cut-off potential followed by a potentiostatic hold at the cut-off potential until the current decayed to 0.01 Li hr^{-1}. After charging, the cells were allowed to rest on open circuit.

Table 3.1: Cumulative CO_2 evolution data from LMNOF materials during charging to cut-off voltages of 4.4 V vs. Li/Li^+, 4.6 V vs. Li/Li^+, and 4.8 V vs. Li/Li^+. Charging consisted of a constant current charge at 0.1 Li hr^{-1} to the listed cut-off potential followed by a potentiostatic hold at the cut-off potential until the current decayed to 0.01 Li hr^{-1}. Error estimates are based on a 6% error obtained from prior replicate DEMS measurements and a minimum error bar size of 0.1 mmol-CO_2 mol-DRX^{-1} obtained from the approximate instrument detection limit.

Material	4.4 V vs. Li/Li^+ (mmol-CO_2 mol-DRX^{-1})	4.6 V vs. Li/Li^+ (mmol-CO_2 mol-DRX^{-1})	4.8 V vs. Li/Li^+ (mmol-CO_2 mol-DRX^{-1})
LMNOF-4515	6.4 ± 0.4	10.2 ± 0.7	11.4 ± 0.7
LMNOF-6060	5.7 ± 0.4	6.2 ± 0.4	7.5 ± 0.5
LMNOF-6368	12.2 ± 0.8	12.4 ± 0.8	13.4 ± 0.9

Table 3.2: Amount of carbonate on DRX cathodes after various extents of charging. Pristine samples were uncharged DRX cathodes that were not exposed to electrolyte. For all charged samples, charging consisted of a constant current charge at 0.1 Li hr^{-1} to the listed cut-off potential followed by a potentiostatic hold at the cut-off potential until the current decayed to 0.01 Li hr^{-1}. After charging, electrodes were harvested from their cells in an Ar filled glovebox, rinsed with DEC, dried overnight under vacuum, and stored under Ar until titration. Error estimates are based on a 2.5 mmol-gas mol-DRX^{-1} standard error obtained from prior replicate TiMS experiments.

Material	As-Synthesized (mmol-CO_3^{2-} mol-DRX^{-1})	4.4 V vs. Li/Li^+ (mmol-CO_3^{2-} mol-DRX^{-1})	4.6 V vs. Li/Li^+ (mmol-CO_3^{2-} mol-DRX^{-1})	4.8 V vs. Li/Li^+ (mmol-CO_3^{2-} mol-DRX^{-1})
LMNOF-4515	7.8 ± 2.5	18.9 ± 2.5	11.8 ± 2.5	8.4 ± 2.5
LMNOF-6060	13.7 ± 2.5	18.1 ± 2.5	20.0 ± 2.5	23.1 ± 2.5
LMNOF-6368	13.6 ± 2.5	16.6 ± 2.5	15.5 ± 2.5	21.4 ± 2.5

The results shown in Figure 3.9 show only a single low-voltage CO_2 evolution process centered around 4.4 V vs. Li/Li^+ for all three materials during both cut-off voltage experiments. As described in the main text, this lower-voltage process is expected to originate from electrolyte degradation at the surface of the DRX cathode. For LMNOF-4515, the second higher-voltage process shown in Figure 3.3 when charging up to 4.8 V vs. Li/Li^+ is not observed. The lack of this second process from LMNOF-4515 when charging to 4.4 V vs. Li/Li^+ and 4.6 V vs. Li/Li^+ is not surprising, however, because the onset of this second process occurs above 4.6 V vs. Li/Li^+.

3.6.3 Cumulative Gas Evolution Quantities from Four-cycle Outgassing Experiments

Table 3.3: Cumulative CO_2, O_2, and H_2 evolution data for the first four cycles of DRX materials. Cycling consisted of charging to 4.8 V vs. Li/Li^+ and discharging to 1.5 V vs. Li/Li^+ at a constant rate of 0.1 Li hr^{-1}. Error estimates are based on a 6% error obtained from prior replicate DEMS measurements and a minimum error bar size of 0.1 mmol-gas mol-DRX^{-1} obtained from the approximate instrument detection limit.

Material	Cumulative Gas Evolved (mmol-gas mol-DRX^{-1})			
	Cycle 1	Cycle 2	Cycle 3	Cycle 4
CO_2				
LMNOF-4515	15.7 ± 1.0	9.8 ± 0.6	9.7 ± 0.6	7.8 ± 0.5
LMNOF-6060	4.7 ± 0.3	3.8 ± 0.3	4.9 ± 0.3	4.2 ± 0.3
LMNOF-6368	9.0 ± 0.6	10.3 ± 0.7	7.0 ± 0.5	7.7 ± 0.5
O_2				
LMNOF-4515	0.4 ± 0.1	∼ 0	∼ 0	∼ 0
LMNOF-6060	∼ 0	∼ 0	∼ 0	∼ 0
LMNOF-6368	∼ 0	∼ 0	∼ 0	∼ 0
H_2				
LMNOF-4515	2.2 ± 0.2	0.8 ± 0.1	0.7 ± 0.1	0.8 ± 0.1
LMNOF-6060	4.8 ± 0.3	2.9 ± 0.2	1.6 ± 0.1	1.4 ± 0.1
LMNOF-6368	2.3 ± 0.2	4.7 ± 0.3	2.5 ± 0.2	1.8 ± 0.2

3.6.4 O_2 Outgassing from DRX Materials during First Charge

O_2 evolution is often observed during charging of DRX materials to high states of delithiation at high voltages, resulting from irreversible oxidation of the DRX lattice. This process degrades the cathode material and has also been shown to lead to the formation of a densified outer layer which may impede Li transport. Previous reports have shown that fluorination suppresses O_2 evolution at high voltages, indicating that fluorine stabilizes the DRX surface against irreversible oxidation. The multiple cycle outgassing comparison in Section 3.4.4 of the main text demonstrated that a small amount of O_2 evolution is observed during charging of LMNOF-4515 to 4.8 V vs. Li/Li^+, whereas no O_2 evolution is observed during charging of LMNOF-6060 and LMNOF-6368 to 4.8 V vs. Li/Li^+. Further, the amount of O_2 evolution observed from LMNOF-4515 is very small compared to the amount of other gases evolved (CO_2, H_2), rendering the O_2 evolution profile very small in comparison. To perform a more detailed analysis of the O_2 evolution occurring during cycling of the LMNOF DRX materials, the O_2 evolution was also monitored by DEMS during a constant current charge to 4.8 V vs. Li/Li^+ at 0.1 Li hr^{-1} followed by a potentiostatic hold at 4.8 V vs. Li/Li^+ until the current decayed to 0.01 Li hr^{-1}.

The results of these experiments are shown in Figure 3.10. Notably, O_2 evolution was detected from LMNOF-4515, beginning at just below 4.8 V vs. Li/Li^+ and subsequently decaying throughout the potentiostatic hold. In contrast, no O_2 evolution is observed from LMNOF-6060 and LMNOF-6368. This observation demonstrates the effect of increasing fluorination in suppressing O_2 evolution during charging to high voltages, a finding consistent with several prior studies investigating reactivity in Mn/Nb-based DRX oxyfluorides.[34,37,52] Although easily detected by DEMS, the total amount of O_2 evolved from LMNOF-4515 is still quite small (3.3 mmol-O_2 mol-DRX^{-1}, ~0.3% of DRX oxygen). As such, the contribution of irreversible oxide oxidation resulting in O_2 loss to the total charge capacity may be neglected.

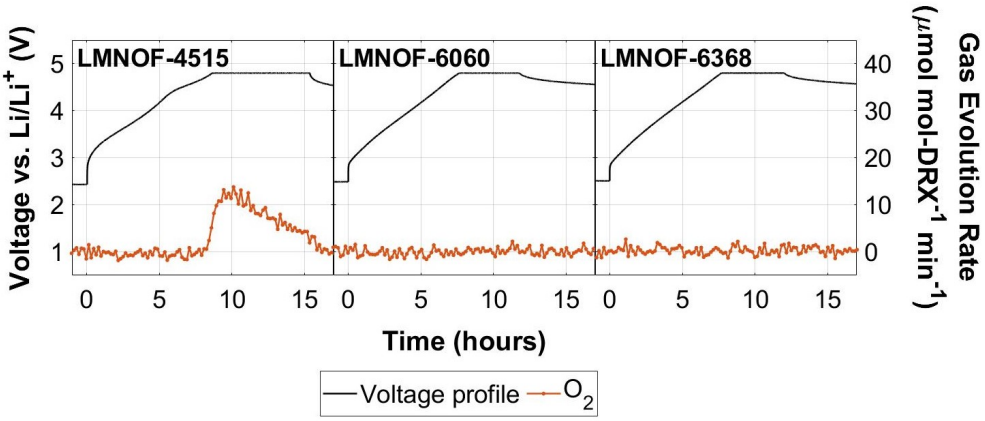

Figure 3.10: DEMS results depicting O_2 evolution from DRX materials during first charge. Charging consisted of a constant current charge at 0.1 Li hr^{-1} to 4.8 V vs. Li/Li^+ followed by a potentiostatic hold at 4.8 V vs. Li/Li^+ until the current decayed to 0.01 Li hr^{-1}. After charging, the cells were allowed to rest on open circuit.

3.6.5 H_2 Evolution – LFP Counter-electrode Experiments

The proposed process underlying H_2 evolution requires crosstalk between two electrodes at significantly different potentials. First, high voltage electrolyte oxidation leads to the formation of protic electrolyte degradation. Next, these protic species diffuse across the electrolyte and arrive at the anode surface, where they are electrochemically reduced at low potentials to form H_2. In order to further investigate this hypothetical process, the Li metal counter electrode was replaced with a delithiated lithium iron phosphate (LFP) electrode.

Delithiated LFP electrodes were prepared by cycling pristine LFP electrodes in a typical DEMS cell setup with a Li metal anode. Each LFP/Li cell was cycled at C/10 (0.23 mA) in the voltage range of 3.0–3.8 V vs. Li/Li^+ for one full cycle to form a stable interface on the LFP surface, after which the cells were charged to 3.8 V at C/10 for a second time. After

the second charge, the cells were dissembled in an Ar filled glovebox and the delithiated LFP electrodes was harvested, rinsed with DEC, and dried overnight under vacuum.

The LFP counter electrode operates stably at a sufficiently high potential (3.3-3.5 V vs. Li/Li^+) that electrochemical reduction of protic species to form H_2 will not occur. The upper and lower cut-off potentials were adjusted to ensure that the DRX cathode operates in roughly the same potential window as it does in the other DEMS experiments: 4.8 V – 1.5 V vs. Li/Li^+. If the actual process leading to H_2 evolution includes reduction of protic species at the anode, then no H_2 evolution will be observed during the DEMS experiment using the LFP counter electrode. If, on the other hand, the process underlying H_2 evolution does not rely on the low-voltage electrochemical reduction of protic species to form H_2, then H_2 evolution should still occur when the LFP counter electrode is used.

The results from the DRX vs. LFP DEMS experiments, including the voltage profiles and the gas evolution profiles for O_2 and H_2, are shown in Figure 3.11. Notably, no H_2 evolution is observed for any of the three materials during charging. The observed O_2 evolution is included to demonstrate that the DRX cathodes exceeded the potential required to drive O_2 evolution from the LMNOF-4515 cathode, a potential at which H_2 evolution is also expected when charging against a Li metal anode. In this context, the lack of H_2 evolution from the cells containing all three DRX materials highlights the importance of a low potential anode surface (i.e. Li metal, graphite) in driving the H_2 evolution process.

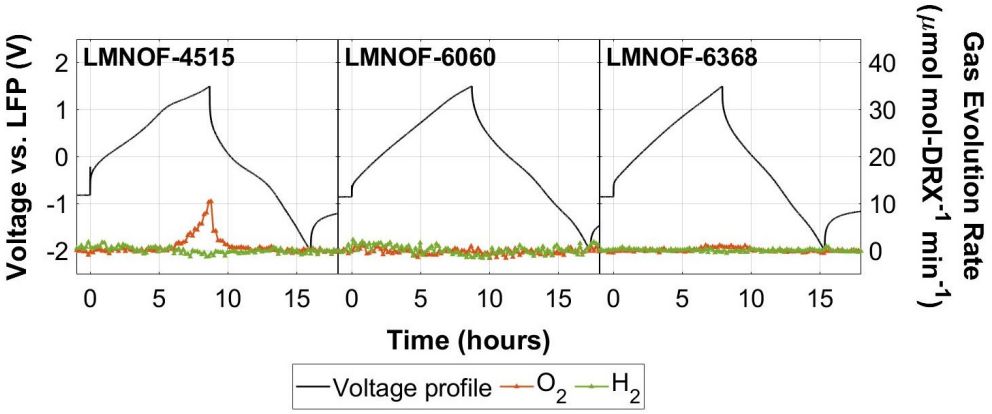

Figure 3.11: DEMS results depicting O_2 and H_2 evolution from DRX materials during first cycle against delithiated LFP, which operates in the range of 3.3-3.5 V vs. Li/Li^+. Cycling was conducted at a constant current of 0.1 Li hr^{-1}. Cell potential cut-offs are set such that the DRX cathode potential is roughly the same range as the other cells: 4.8 V – 1.5 V vs. Li/Li^+.

3.6.6 Evaluating the Stability of LiTFSI for Fluoride-Scavenging

In order to determine the stability of LiTFSI-based electrolytes towards fluoride-scavenging, we conducted a fluoride-scavenging DEMS experiment using a $Li(Ni_{1/3}Mn_{1/3}Co_{1/3})O_2$ (NMC-111, TCI America) cathode, such that the only source of fluorine was the LiTFSI salt in the electrolyte. The NMC-111 cathode was made using the same fabrication technique and non-active components (stainless steel mesh current collector, acetylene black carbon, and polyethylene binder) as those used for the DRX cathodes used in the fluoride-scavenging experiments in the main text. Furthermore, the cell used in this experiment contained the same cell components (electrolyte, separator, anode) as the fluoride-scavenging experiments conducted in the main text. Consequently, the only difference between the NMC-111 cell and the cells used in the fluoride-scavenging experiments in the main text was that the cathode active material was an NMC-111 oxide instead of a DRX oxyfluoride. Since all sources of fluorine aside from the LiTFSI-based electrolyte are eliminated from the cell, any observed Me_3SiF must originate from the fluoride-scavenging reaction of TMSPa with any LiTFSI-originating fluorine.

The results of this fluoride-scavenging control experiment are shown in Figure 3.12. The gas evolution profile is plotted on the same scale as those in the main text to facilitate comparisons between active materials. Importantly, no significant Me_3SiF evolution is observed during the charge to 4.8 V vs. Li/Li^+. The lack of Me_3SiF evolution indicates that TMSPa has not reacted with any fluoride in the electrolyte throughout the first cycle, demonstrating that LiTFSI is stable towards fluoride-scavenging within the voltage window used for all fluoride-scavenging experiments. Based on this observation, we assume that any Me_3SiF evolved during fluoride-scavenging DEMS experiments with DRX oxyfluorides originates from reaction of TMSPa with DRX-originating fluoride in the electrolyte.

While the findings of this control experiment demonstrate that LiTFSI is stable with respect to fluoride formation at the NMC-111 surface up to 4.8 V vs. Li/Li^+, the question remains as to whether or not the reactivity of LiTFSI may differ for Mn/Nb-based DRX oxyfluorides. To this end, the very small amount of Me_3SiF evolution detected during the cycling of LMNOF-4515 (Figure 3.5) also further supports the observation that LiTFSI does not degrade to form fluoride to a significant extent during cycling. The small amount of Me_3SiF evolved during cycling of LMNOF-4515 in LiTFSI-based electrolyte with TMSPa is assumed to originate from the DRX lattice. However, the extent of Me_3SiF evolution with LMNOF-4515 is so small relative to the that with LMNOF-6060 and LMNOF-6368 that, even if the Me_3SiF evolution observed with LMNOF-4515 is LiTFSI-originating, LiTFSI can still be considered stable on the scale of the Me_3SiF evolution observed with LMNOF-6060 and LMNOF-6368.

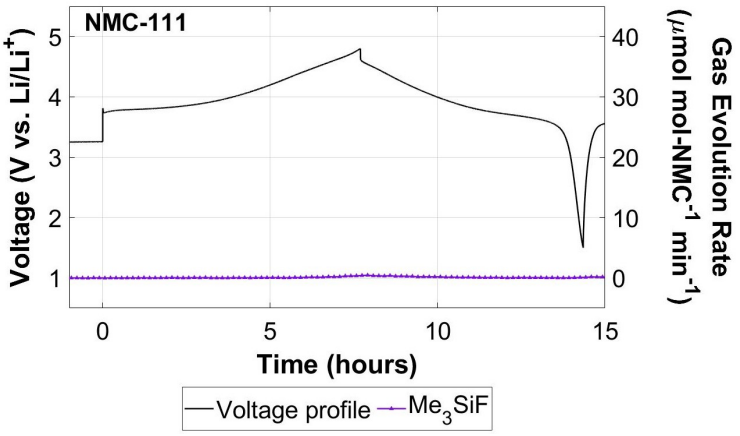

Figure 3.12: In-situ fluoride-scavenging DEMS of NMC-111 cathode over the first cycle using LiTFSI-based electrolyte. Cycling consisted of charge to 4.8 V vs. Li/Li^+ and a discharge to 1.5 V vs. Li/Li^+, each at a constant current of 0.1 Li hr^{-1}. Before and after cycling, the cell was allowed to rest at open circuit.

3.6.7 Cumulative Gas Evolution Quantities from Fluoride-Scavenging DEMS Experiments with LiTFSI-based Electrolyte

Table 3.4: Cumulative Me_3SiF evolution quantities measured by fluoride-scavenging DEMS and corresponding fractions of DRX-originating fluorine dissolved for each DRX material during the first three cycles. The electrolyte was 1M LiTFSI in 1:1 EC:DEC with 1vol% TMSPa additive. Materials were cycled between 4.8 V vs. Li/Li^+ and 1.5 V vs. Li/Li^+ at a constant current of 0.1 Li hr^{-1}. Error estimates are based on a 6% error obtained from prior replicate DEMS measurements and a minimum error of 0.1 mmol-gas mol-DRX^{-1} obtained from the approximate instrument detection limit.

Material	Cycle 1	Cycle 2	Cycle 3
Cumulative Me_3SiF Evolved (mmol mol-DRX^{-1})			
LMNOF-4515	0.4 ± 0.1	0.2 ± 0.1	0.1 ± 0.1
LMNOF-6060	6.4 ± 0.4	2.4 ± 0.2	0.9 ± 0.1
LMNOF-6368	8.5 ± 0.6	2.0 ± 0.2	0.9 ± 0.1
Fraction of DRX Fluorine Dissolved (%)			
LMNOF-4515	0.3 ± 0.07	0.1 ± 0.07	0.07 ± 0.07
LMNOF-6060	1.1 ± 0.07	0.4 ± 0.03	0.2 ± 0.02
LMNOF-6368	1.3 ± 0.09	0.3 ± 0.03	0.1 ± 0.01

3.6.8 Fluoride-Scavenging DEMS with $LiPF_6$-based Electrolyte

To examine the effect of the electrolyte salt on fluoride formation in the electrolyte, fluoride-scavenging DEMS using an $LiPF_6$-based electrolyte was conducted with the LMNOF materials as well as a fluorine-free DRX oxide (LMNO-6000: $Li_{1.2}Mn_{0.60}Nb_{0.20}O_2$). LMNO-6000, which has been characterized in previous reports, is a Mn/Nb-based DRX oxide that utilizes $Mn^{3+/4+}$ and oxygen redox, making it the one of the best available materials to serve as a fluorine-free analog to the DRX materials studied in this work.[32,37] The electrolyte used for these experiments was 1M $LiPF_6$ in 1:1 EC:DEC with 1vol% TMSPa. Since $LiPF_6$ commonly degrades to form fluoride species like LiF and HF, Me_3SiF evolution in a cell with an $LiPF_6$-based electrolyte can originate from reaction of TMSPa with fluoride that forms in the electrolyte due to either dissolution of DRX-originating fluorine or degradation of the $LiPF_6$ electrolyte. Because LMNO-6000 contains no fluorine, the fluoride-scavenging DEMS experiment with LMNO-6000 serves as an approximate control for the amount of fluoride that forms due to degradation of $LiPF_6$ during cycling of the LMNOF materials. However, LMNO-6000 is likely to possess slightly different interfacial reactivity than the LMNOF materials studied herein, owing to the fact that it is fluorine-free and synthesized by solid-state synthesis instead of high-energy ball-milling. As such, the use of LMNO-6000 to approximate the extent of $LiPF_6$ degradation in the LMNOF materials must be done with caution.

The results of fluoride-scavenging DEMS experiments using $LiPF_6$-based electrolyte are shown in Figure 3.13 and the cumulative amounts of Me_3SiF evolved are given in Table 3.5. For all four materials, extensive Me_3SiF evolution is observed with an onset voltage around 4.2 V vs. Li/Li^+. In the case of LMNO-6000, the fluoride that reacts with TMSPa must originate entirely from $LiPF_6$ degradation. The total amount of Me_3SiF evolved during charging of LMNO-6000 therefore provides a rough estimate for the amount of Me_3SiF that may evolve due to $LiPF_6$ degradation alone during cycling of the other DRX materials. For all three LMNOF materials studied in this work, the amount of Me_3SiF evolved during the first cycle in $LiPF_6$-based electrolyte is much greater than the amount evolved during the analogous experiment with LiTFSI-based electrolyte (given previously in Table 3.4). Furthermore, the difference in Me_3SiF evolution between the two experiments is more than can be accounted for by the $LiPF_6$ degradation observed in the LMNO-6000 experiment, suggesting that the $LiPF_6$-based electrolyte increases the extent of fluorine dissolution from the DRX lattice. This observation may explain the difference in magnitude of fluorine dissolution demonstrated by fluoride-scavenging DEMS and XPS, as an LiTFSI-based electrolyte was used in fluoride-scavenging DEMS whereas an $LiPF_6$-based electrolyte was used in the preparation of XPS samples.

We note that in the case of the ball-milled DRX oxyfluorides, H_2 evolution coincides with Me_3SiF evolution. This behavior is similar to the outgassing observed in the LiTFSI-based fluoride-scavenging experiments. As was explained in Section 3.4.5, the acidic species that underlie the observed H_2 evolution may assist in the dissolution of fluoride from the cathode surface. Since reaction between $LiPF_6$ and acidic protons is known to produce fluoride, however, an alternative explanation for this behavior in the $LiPF_6$-based electrolyte

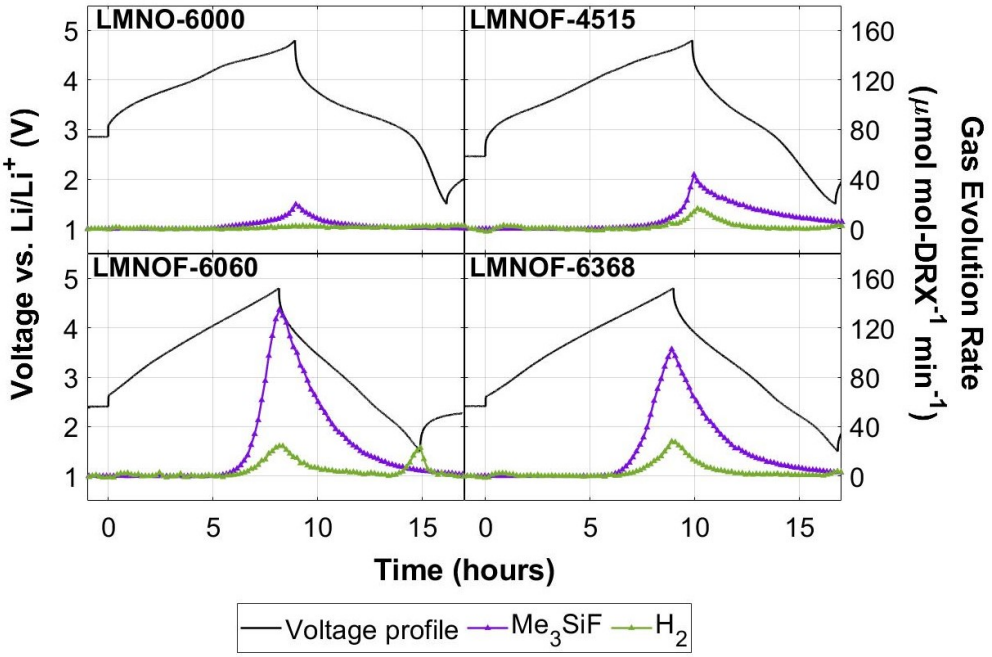

Figure 3.13: In-situ fluoride-scavenging DEMS of LMNO-6000, LMNOF-4515, LMNOF-6060, and LMNOF-6368 using $LiPF_6$-based electrolyte. Cycling consisted of charge to 4.8 V vs. Li/Li^+ and a discharge to 1.5 V vs. Li/Li^+, each at a constant current of 0.1 Li hr^{-1}. Before and after cycling, the cell was allowed to rest at open circuit. The electrolyte was 1M $LiPF_6$ in 1:1 EC:DEC with 1% TMSPa.

is that the acidic electrolyte degradation products formed at the ball-milled DRX surface subsequently react with $LiPF_6$ to form additional fluoride in the electrolyte.[78] This $LiPF_6$-originating fluoride would then be scavenged by TMSPa, evolving Me_3SiF as observed. In contrast, H_2 evolution is not detected from the cell containing LMNO-6000, indicating that acidic electrolyte degradation products are not formed at the cathode surface. As such, it is possible that the control experiment using LMNO-6000 to estimate the amount of fluoride formed by $LiPF_6$ degradation underestimates the extent of $LiPF_6$ degradation occurring in cells with the ball-milled oxyfluoride materials due to the lack of acidic degradation products formed at the LMNO-6000 surface. This confluence of factors highlights the complexity of the system under investigation and the need for cautious interpretation of the results obtained.

Table 3.5: Amount of Me_3SiF evolved from DRX materials during first cycle in 1M $LiPF_6$ in 1:1 EC:DEC with 1vol% TMSPa additive. Materials were cycled between 4.8 V vs. Li/Li^+ and 1.5 V vs. Li/Li^+ at a constant current of 0.1 Li hr^{-1}. Error estimates are based on a 6% error estimate obtained from prior replicate DEMS measurements.

Material	Cumulative Me_3SiF Evolved (mmol mol-DRX^{-1})
LMNO-6000	2.9 ± 0.2
LMNOF-4515	9.1 ± 0.6
LMNOF-6060	24.5 ± 1.5
LMNOF-6368	20.7 ± 1.3

3.6.9 Solid State NMR

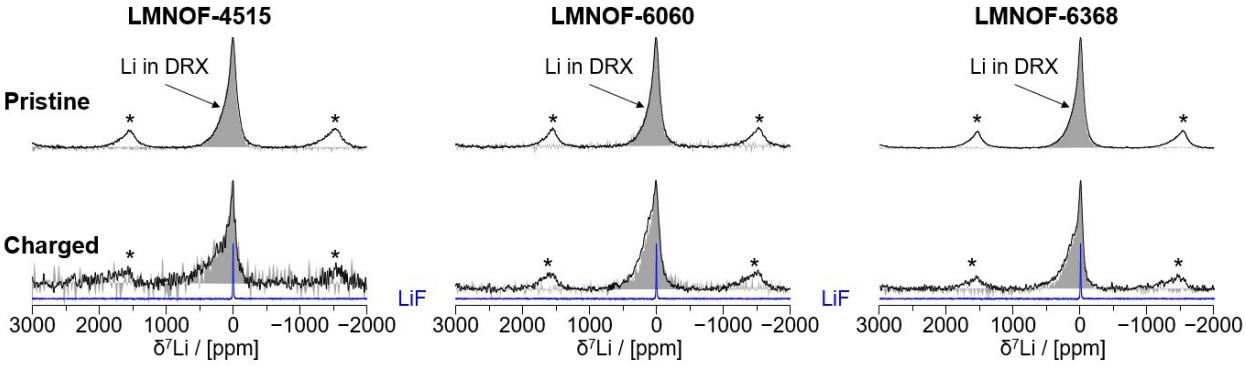

Figure 3.14: ^{7}Li NMR spectra (spin echoes in black and isotropic spectra obtained using the pj-MATPASS sequence in grey shading) recorded on pristine (top) or charged (bottom) LMNOF electrodes (from left to right: LMNOF-4515, LMNOF-6060, and LMNOF-6368) at B_0 = 2.35 T with a sample spinning speed ν_R = 60 kHz.[96,97] The intensity of LMNOF ^{7}Li spectra was normalized so that each spectrum reaches the same intensity. ^{7}Li spectrum of pure LiF is also shown (δ_{iso} = -1 ppm, in blue) for comparison with LMNOF electrodes. Spinning sidebands are indicated with asterisks. Charging consisted of a constant current charge at 0.1 Li hr^{-1} to 4.8 V vs. Li/Li^+ followed by a potentiostatic hold at 4.8 V vs. Li/Li^+ until the current decayed to 0.01 Li hr^{-1}. The electrolyte was 1M $LiPF_6$ in EC:DEC.

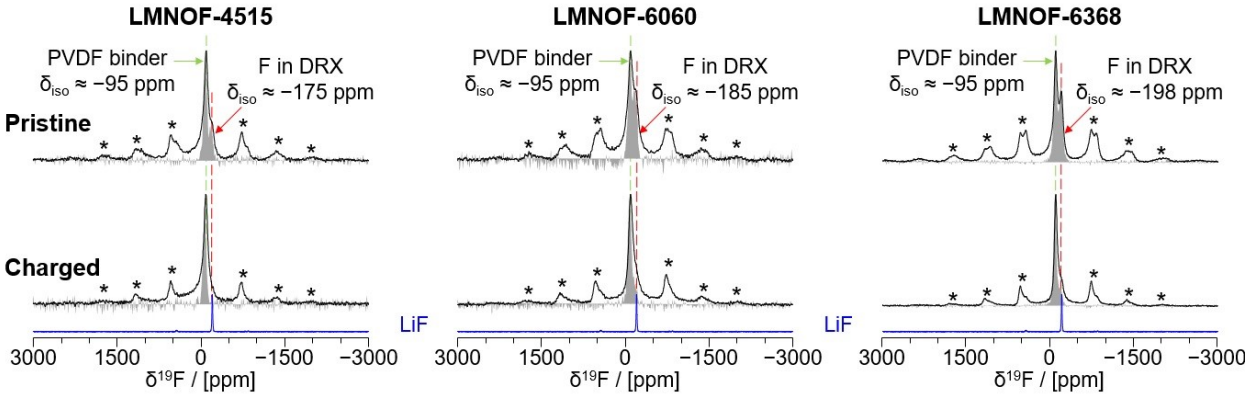

Figure 3.15: ^{19}F NMR spectra (spin echoes in black and isotropic spectra obtained using the pj-MATPASS sequence in grey shading) recorded on pristine (top) or charged (bottom) LMNOF electrodes (from left to right: LMNOF-4515, LMNOF-6060, and LMNOF-6368) at B_0 = 2.35 T with a sample spinning speed ν_R = 60 kHz.[96,97] ^{19}F spectrum of pure LiF is also shown (δ_{iso} = -204 ppm) for comparison with LMNOF electrodes. Spinning sidebands are indicated with asterisks. The isotropic chemical shift of the PVDF binder is highlighted at $\delta_{iso} \sim$ -95 ppm with a green dashed line. The most intense ^{19}F signal coming from F^- ions in the LMNOF structure is highlighted with a red dashed line along with its observed chemical shift δ. The intensity of LMNOF ^{19}F spectra was normalized so that the PVDF signal of each spectrum reaches the same intensity.

Chapter 4

Reconciling Interfacial Degradation and Cycling Performance Decay for Cation-Disordered Rocksalt Cathodes

4.1 Abstract

Li-excess, cation-disordered rocksalt (DRX) cathode materials possess promising electrochemical properties and resource-friendly compositions, making them attractive candidates for advanced Li-ion cathode materials. A key drawback is high reactivity at the cathode-electrolyte interface, which leads to electrolyte degradation processes that persist throughout extended cycling. This sustained degradation causes a decay in cell performance, ultimately compromising energy density and rate capability. In this work, differential electrochemical mass spectrometry (DEMS) is used to reveal the nature and magnitude of electrolyte degradation processes that occur during initial cycling of DRX cathodes. Specifically, DEMS is applied to the cycling of DRX cathodes in different voltage windows, demonstrating the manner in which high- and low-voltage processes separately contribute to degradation at the cathode-electrolyte interface. Subsequently, extended cycling experiments are employed to examine the performance retention of DRX cathodes in electrolyte-lean DRX-graphite full-cells with the same set of voltage windows, showing that performance decay is exacerbated by cycling in voltage ranges that induce interfacial degradation. Finally, we conduct post-mortem analyses of the full-cells after cycling to examine the cell degradation that underlies performance decay, revealing the loss of active Li and the dissolution of Mn and Ti from the DRX cathode. Combining the results of these different analyses, we demonstrate a clear link between electrolyte degradation and performance decay during cycling of DRX materials. This work highlights the necessity of voltage window optimization to maximize DRX cycling performance and the importance of cell design when evaluating cycling stability.*

*This chapter is largely adapted, with permission from all co-authors, from: Crafton et al. *In Prep* **2023**.

4.2 Introduction

The rapid growth in demand for electrochemical energy storage technologies, spurred on by the burgeoning electric vehicle and portable electronic industries, has created a tremendous need for low-cost, high energy density, resource-friendly batteries. To date, this demand has largely been met by Li-ion batteries. However, the cathode materials used in conventional Li-ion batteries remain a significantly limiting factor when it comes to the metrics of cost, resource abundance, and energy density.[4,11] Layered transition metal oxides (TMOs) provide relatively high energy density when paired with conventional anodes, but they rely on scarce and expensive transition metals like Co and Ni for charge compensation during electrochemical cycling.[15] On the other hand, lithium iron phosphate is inexpensive and contains earth-abundant elements, but it provides a relatively low energy density when paired with conventional anodes.[4] Consequently, Li-ion batteries tend to get split into two camps based on their cathode material: high energy density batteries that are expensive and contain scarce elements, and low energy density batteries that are inexpensive and contain earth-abundant elements. To circumvent this tradeoff, new cathode materials that unlock a favorable combination of all three metrics (cost, energy density, resource abundance) must be developed. To this end, lithium-excess, cation-disordered rocksalt (DRX) cathode materials have become a leading candidate to provide a solution to this problem due to their compositional flexibility and high capacity.[44]

DRX materials possess a rocksalt structure similar to that of layered TMOs. However, unlike layered TMOs, the lithium and transition metals within the DRX cation sublattice possess no long-range order. Without the requirement to form and maintain a layered or otherwise long-range ordered cation sublattice, a wide variety of redox-active transition metal centers can be incorporated into DRX materials, including Mn, Fe, Ni, V, and Cr.[44] Importantly, this compositional flexibility enables the formulation of resource-friendly, low-cost cathode materials by the incorporation of earth-abundant transition metal redox centers like $Mn^{3+/4+}$.[32,34] Along the same lines, the cation-disordered nature of DRX materials also allows for the incorporation of fluorine into the anion lattice.[66,91] Fluorination has been shown in previous reports to confer several advantages, including increasing the fraction of redox-active transition metals and stabilizing the DRX surface at high-voltages.[34,37,93]

As designated by the term 'Li-excess', DRX materials also possess a Li-rich composition, often containing 10-30% more Li than a 'Li-stoichiometric' TMO like $LiCoO_2$.[64,99] Given that the disordered cation sublattice possesses a statistical distribution of local coordination environments determined by the DRX composition,[89] this Li-excess composition leads to a high concentration of so-called Li-O-Li configurations in which two Li ions are bonded to an oxygen atom on opposite sides from one another.[44] Li-O-Li configurations have been shown to give rise to an electronic structure that is conducive to reversible oxygen redox, thereby poising a secondary bulk redox process to provide additional charge compensation beyond that which can be provided by transition metal redox alone.[23] Consequently, the oxygen redox process that is enabled by the Li-excess composition and disordered cation sublattice raises the achievable capacity of DRX materials to values as high as 300-350 mAh

g^{-1}, exceeding the capacities of traditional layered TMOs.[32,66]

These two characteristics, compositional flexibility and high capacity, make DRX materials uniquely suited to enable the development of improved Li-ion batteries with high energy density, low-cost, and resource-friendly composition. Unfortunately, DRX materials suffer from extremely high interfacial reactivity that leads to sustained electrolyte degradation during electrochemical cycling.[32,37] In addition to simply depleting the electrolyte, this degradation initiates a cascade of deleterious processes driven by the reaction of electrolyte degradation products with other cell components.[35] While this degradation is known to lead to performance decay, there has yet to be a comprehensive study investigating the role of interfacial degradation in long-term performance decay for DRX materials. In fact, many of the studies that have looked at the cycling performance of DRX materials have employed electrolyte-flooded half-cells.[34,52–54] While these cell characteristics aid in the investigation of DRX bulk electrochemistry, the large excess of electrolyte and the large reservoir of active lithium in the lithium metal counter-electrode mask the effects of electrolyte degradation. Consequently, the exact nature of performance decay driven by interfacial degradation during cycling of DRX cathodes remains relatively unexplored.

In this work, we seek to characterize the extent to which electrolyte degradation contributes to performance decay during cycling of a DRX oxide, $Li_{1.2}Mn_{0.4}Ti_{0.4}O_2$ (LMTO). First, differential electrochemical mass spectrometry (DEMS) is used to measure the extent of electrolyte degradation that occurs during early cycling of a LMTO cathodes in a set of different voltage windows. Next, the cycling performance of LMTO cathodes in the same voltage windows is examined using a custom-designed full-cell configuration that exposes the effects of interfacial degradation. Specifically, the full-cell is an electrolyte-lean coin cell with an LMTO cathode and a pre-formed, partially pre-lithiated graphite anode. Lastly, we follow up with a 'post-mortem' analysis of each full-cell after cycling by disassembling each cell, examining the electrochemical performance and interfacial reactivity of each electrode, quantifying various forms of inactive Li on the graphite surface, and measuring the amount of transition metals dissolved from the cathode. By comparing electrolyte degradation during early cycling with the performance retention over long-term cycling for the different voltage windows, we demonstrate a clear correlation between electrolyte degradation and performance decay. Furthermore, with the information obtained from the post-mortem analysis, we reveal details about the specific degradation processes that most critically contribute to performance decay.

4.3 Experimental Methods

4.3.1 LMTO Material Synthesis

LMTO ($Li_{1.2}Mn_{0.4}Ti_{0.4}O_2$) was synthesized by a traditional solid-state method. Li_2CO_3 (Sigma, 99%), Mn_2O_3 (Alfa Aesar, 99.9%) and TiO_2 (Alfa Aesar, 99.9%) were used as precursors. All the precursors were stoichiometrically mixed in ethanol with a Retsch PM

200 planetary ball mill at a rate of 250 rpm for 12 hr. 10% excess Li_2CO_3 was added to compensate for possible loss during synthesis at high temperature. The precursors were then dried in an oven at 70°C overnight and pelletized. The precursor pellets were heated to 1100°C at a rate of 9°C min^{-1} under Ar gas flow and held for 20 min followed by cooling naturally in the furnace.

4.3.2 LMTO Electrode Fabrication

As-synthesized LMTO and SuperP C65 Carbon Black (Timcal) were mixed to yield an LMTO:C ratio of 70:20 (wt), and the resulting mixture was shaker-milled with for 1 hour in an Argon atmosphere using a SPEX 8000M mixer/miller. The LMTO:C mixture was then mixed with additional SuperP Graphite Carbon Black (Timcal) to yield a LMTO:C ratio of 62:28 (wt), and the resulting mixture was ground in a mortar and pestle. Next, the LMTO:C mixture was mixed with a solution of 10wt% polyvinylidene fluoride (PVDF, Solef 6010/1001, Solvay) in N-methyl-2-pyrrolidone (anhydrous, 99.5%, Sigma-Aldrich) to yield a LMTO:C:PVDF (wt) ratio of 62:28:10. The resulting slurry was then spread onto 1/2-inch stainless steel mesh discs using a doctor blade. The resulting electrodes were then dried using a two-step method, consisting of a brief initial drying on a hot plate at 90°C for 30 minutes followed by a more thorough drying at 120°C under vacuum overnight. The average electrode loading was approximately 5 mg-LMTO cm^{-2}.

4.3.3 Differential Electrochemical Mass Spectrometry (DEMS)

Custom-built Swagelok cells were used as described previously.[80–82] The anode was 11 mm Li foil and the cathode was an LMTO electrode (pristine for initial cycling DEMS, extracted from full-cell for post-mortem DEMS). The separator was composed of 1 sheet of quartz fiber filter paper (Whatman QM-A) on the Li metal side and 1 sheet of polypropylene (Celgard 2500) on the LMTO side. The electrolyte was 1M lithium hexafluorophosphate ($LiPF_6$, BASF) in 3:7 (vol) mixture of ethylene carbonate (EC, Gotion):ethyl methyl carbonate (EMC, Gotion), and the electrolyte loading was 60 μL cm^{-2}. After assembly in an Argon atmosphere glovebox, the hermetically-sealed, custom-built Swagelok cells were appropriately attached to the DEMS apparatus to avoid air exposure. The custom-built DEMS instrument and its operation was described in previous publications.[80–82] The cells were cycled on a Bio-Logic VSP-series potentiostat under positive Ar pressure (approximately 1.2 bar). For all DEMS experiments, cells were cycled at a current of 0.1 Li hr^{-1} (32.9 mA g-$LMTO^{-1}$) in the voltage windows listed with each experiment. After each discharge, the cells were allowed to rest on open circuit for a period of 2-5 hours, depending on the experiment. For initial cycling DEMS experiments, the rest period was 2 hours. For post-mortem DEMS experiments, the rest period was 5 hours. Throughout the experiment, the cell headspace was purged with 500 μL of Ar by the DEMS instrument every 10 minutes and any accumulated gases were swept to the mass spectrometer chamber for analysis. The apparatus is calibrated for O_2, CO_2, and H_2 in Ar, allowing for the determination of the

partial pressures of each analyte. The amount of each gas evolved was then quantified using the known volume, temperature, and partial pressure of the gas in each sample through the ideal gas law.

4.3.4 Coin Cell Cycling

Coin cells were assembled inside an Argon atmosphere glovebox using Hohsen CR2032 coin cell parts. For all coin cells, the separator was a single sheet of polypropylene (Celgard 2500), and 40 μL of 1M $LiPF_6$ in 3:7 (vol) EC:EMC was used as the electrolyte. The electrolyte loading was approximately 30 μL cm^{-2}. After assembly, the cells were placed in CCH-8 coin cell holders inside an environmental chamber (Thermotron) set to 30°C. Electrochemical cycling was performed with a Biologic MPG-200 potentiostat.

For the cells in which pre-lithiated graphite electrodes where prepared, the electrodes were 15 mm graphite electrodes (3.1 mAh cm^{-2}, Argonne National Laboratory CAMP Facility, 91.83wt% Superior Graphite SLC 1406T, 2wt% Timcal C45 carbon, 6wt% Kureha 9300 PVDF binder, 0.17wt% Oxalic Acid on 10μm Cu foil) and 15 mm Li foil discs. These cells underwent three formation cycles in the voltage window of 1.5 - 0.01 V, with graphite lithiation and delithiation occurring at a constant rates of 0.56 mA and 1.12 mA, respectively. The total graphite capacity on the final formation cycle was approximately 5.9 mAh. The graphite electrodes were then lithiated at a rate of 0.56 mA until the graphite was 40% lithiated (based on the capacity of the final formation cycle), corresponding to a lithiation capacity of approximately 2.35 mAh. The potential of the graphite electrodes at this state of lithiation was roughly 0.1 V vs. Li/Li^+.

For the full-cells, the electrodes were an LMTO electrode and a formed, 40% pre-lithiated graphite electrode. Importantly, the 40% pre-lithiation of the graphite electrodes left 60% of the graphite capacity, or roughly ∼3.55 mAh, available for lithiation during the first charge of the full-cells. This additional capacity was comfortably greater than the capacities obtained during the first charge of LMTO cathodes, which were in the range of 1.8-2.1 mAh for the cells charged to 4.8 V and 1.5-1.7 mAh for the cells charged to 4.6 V, ensuring that the pre-lithiated graphite electrodes can accommodate the first charge of the full-cell. Furthermore, this portion of the graphite capacity has a voltage range of 0.1-0.01 V vs. Li/Li^+, which we consider suitably low enough that the cell potential may be used to approximate the potential of the LMTO cathode during initial cycling. The cells underwent long-term cycling in the voltage window listed with each experiment for a total of 204 cycles. The first three cycles were conducted at a slow rate of 10 mA g-LMTO^{-1} to allow for LMTO-electrolyte interface formation, and the subsequent extended cycling was conducted at a rate of 0.1 Li hr^{-1} (32.9 mA g-LMTO^{-1}). Starting on the first cycle at 0.1 Li hr^{-1}, which was the fourth cycle overall, electrochemical impedance spectroscopy (EIS) measurements were taken every ten cycles in the fully charged and discharged states. The EIS measurements were taken with an impedance range of 20 kHz to 100 mHz and a voltage amplitude of 5 mV. For cycles on which EIS measurements were not taken, the cell was allowed to rest for two hours after each discharge. For cycles on which EIS measurements were taken (4th, 14th, 24th,...), the cell

was allowed to rest on open-circuit for four hours after each charge and discharge before the EIS measurement was taken to allow the cell voltage to stabilize. Consequently, the cycles in which EIS scans were taken employ an additional rest in the charged state that was not included in the other cycles.

For cells used to examine the post-mortem performance of graphite electrode, the electrodes were cycled graphite electrodes extracted from full-cells and 15 mm Li foil discs. The graphite electrodes underwent three slow cycles in the voltage window of 1.5 - 0.01 V, with graphite delithiation occurring first. Each of the delithiation and lithiation steps consisted of a constant current portion at a rate of 100 μA until the cell reached the relevant cut-off voltage followed by a potentiostatic hold at the cut-off voltage for 5 hours.

4.3.5 Extraction of Cell Components

After completion of electrochemical cycling, cells were returned to an Argon atmosphere glovebox. Coin cells were de-crimped, while Swagelok-style DEMS cells were disassembled. Any cell components to be extracted, including electrodes and separators, were then removed and placed in glass vials. Once extracted, electrodes (LMTO or graphite) were rinsed with 600 μL of dimethyl carbonate (DMC) in two 300 μL aliquots. Last, all cell components were dried under vacuum at room temperature overnight. After drying, all cell samples were stored for the subsequent experiment.

4.3.6 Titration Mass Spectrometry Analysis of Graphite Electrodes

The design and operation of the custom-built titration mass spectrometry (TiMS) instrument is nearly identical to that of the DEMS instrument, as described in previous publications.[49,80–82] Graphite electrode samples were placed in a custom-built, hermetically sealed titration vessel. This vessel was then appropriately connected to the TiMS apparatus to avoid air exposure. During the experiment, the cell headspace was purged with 2 mL of Ar by the TiMS instrument every 2 minutes and any accumulated gases were swept to the mass spectrometer chamber for analysis. After establishing baseline levels for gases of interest, 2 mL of N_2-sparged 3.5M H_2SO_4 was injected into the titration vessel through a septum-sealed injection port. The resulting mixture was mixed with a magnetic stir bar. Gas samples were taken until the reaction was completed, as determined by the return of any analyte signals to their baseline levels. The apparatus is calibrated for O_2, CO_2, and H_2 in Ar, allowing for the determination of the partial pressures of each analyte. The amount of each gas evolved was then quantified using the known volume, temperature, and partial pressure of the gas in each sample through the ideal gas law.

4.3.7 ICP-OES Analysis of Mn and Ti Dissolution

Inductively coupled plasma optical emission spectroscopy (ICP-OES) measurements were performed using a Perkin Elmer 5300 DV optical emission inductively coupled plasma spectrometer with an auto sampler. For all samples and standards, a matrix solution consisting of 2wt% HNO_3 (70%, Sigma Aldrich) and 0.1wt% $H_2C_2O_4$ (oxalic acid dihydrate, Suprapur, Sigma Aldrich) in deionized water was used. Manganese and titanium standard solutions for ICP-OES (Sigma Aldrich) were diluted with matrix solution to eight different concentrations to calibrate manganese between 0-100 mg L^{-1}, and all sample measurements fell within the calibrated range. For the LMTO cathodes and separators, samples were separately soaked in 20 mL of matrix solution. For graphite electrodes, 1.9 mL of the the acidic solution leftover after TiMS analysis was instead dissolved into 18.1 mL of ICP matrix. The resulting solutions were stored for three days to allow for full dissolution of Mn and Ti ions, after which the solutions were filtered. The concentration of Mn and Ti ions in the resulting filtered solutions were then analyzed by ICP-OES, and the amounts of each metal in each cell component were calculated using the measured concentration and the solution volume. Last, the LMTO-normalized fractions of each metal in each cell component were calculated using the amounts of each metal in each cell component and the corresponding pristine LMTO cathode loading.

4.4 Results and Discussion

4.4.1 Outgassing During Early Cycling

Many of the interfacial degradation processes that occur during cycling of DRX materials result in the evolution of gaseous degradation products. O_2 evolution, a process typically confined to the first charge, commonly occurs due to irreversible oxidation of DRX surface.[34,35,37] Furthermore, CO_2 evolution is typically observed due to decomposition of carbonate species within the cell at the DRX surface. These carbonates may be either native carbonate species on the DRX surface or the organic carbonate solvents used in the electrolyte. Native surface carbonate species are inevitably present in small quantities on the DRX surface, either as residual precursor from synthesis or the product of reaction between the DRX and ambient CO_2 during material handling. Previous work has demonstrated that these native carbonates can decompose to evolve CO_2 via both chemical and electrochemical processes at potentials above 3.8 V vs. Li/Li^+.[27,84,102,115] The organic carbonate solvents used in the electrolyte in this work are ethylene carbonate (EC) and ethyl methyl carbonate (EMC), both of which are prone to decomposition evolving CO_2 at potentials above ~4.0 V vs. Li/Li^+.[35,37,116,117]

To examine the nature and extent of the interfacial degradation that occurs during initial cycling of DRX materials, outgassing was measured using differential electrochemical mass spectrometry (DEMS). LMTO electrodes were cycled against Li metal counter-electrodes for four cycles in a set of different voltage windows while outgassing was measured. The upper cut-off voltages employed were 4.6 and 4.8 V vs. Li/Li^+, and the lower cut-off voltages

employed were 1.5, 1.85, and 2.0 V vs. Li/Li^+. Each combination of upper and lower cut-off voltages was studied, resulting in six unique experiments. The results of these experiments, depicting the gas evolution profiles for O_2 and CO_2 alongside the cell voltage profiles, are shown in Figure 4.1. Furthermore, the cumulative O_2 and CO_2 evolution quantities for each experiment are given, on a per-cycle basis, in Table 4.1.

O_2 evolution is observed in similar quantities for the three voltage windows with an upper cut-off voltage of 4.8 V. In contrast, negligible O_2 evolution is observed during the first charge for the three voltage windows with an upper cut-off voltage of 4.6 V. This result demonstrates that oxygen loss from the LMTO surface occurs at potentials above 4.6 V during the first charge. The lack of O_2 evolution on the subsequent charges to 4.8 V indicates that an oxygen-depleted region forms near the surface of LMTO, passivating the material from further O_2 loss. Furthermore, the lack of dependence on lower cut-off voltage is not surprising, as the surface oxidation underlying O_2 evolution is dependent only on the conditions of the first charge.[37]

CO_2 evolution is observed during charging for all four cycles of LMTO with a strong dependence on both the cycle number and the voltage window. Referring to the CO_2 evolution observed during the first charge in each voltage window, it can be seen that relatively large quantities of CO_2 evolution, arranged in two distinct peaks, are observed. The first peak begins to grow around 3.8 V and reaches a maximum around 4.4 V. The second peak begins to stand out from the first peak at around 4.5 V and continues to grow with charging, reaching a maximum at the end of charge. For the experiments with an upper cut-off voltage of 4.6 V, the CO_2 evolution rate at the end of charge is roughly equivalent to the rate at the top of the first CO_2 evolution peak. In contrast, for the experiments with an upper cut-off voltage of 4.8 V, the CO_2 evolution rate grows dramatically above 4.6 V, ultimately reaching a value at the end of charge that is roughly double the rate at the top of the first CO_2 evolution peak. Based on CO_2 evolution alone, it is impossible to assess the extent to which native carbonate decomposition and electrolyte degradation contribute to the CO_2 evolution observed on the first charge. However, previous work has indicated that native carbonate decomposition contributes most significantly to the high-voltage CO_2 evolution peak at the end of charge.[35]

The CO_2 evolution observed during charging for the subsequent cycles, which is expected to originate primarily from electrolyte degradation, depends strongly on both the upper and lower cut-off voltages. For the cells discharged to 1.5 V, CO_2 evolution begins immediately upon the start of the subsequent charge. This early CO_2 evolution from these cells continues to grow during charging, resulting in a broad CO_2 evolution peak that reaches a maximum around 4.0 V. For the 4.6 – 1.5 V cell, little additional CO_2 evolution is observed outside of this broad CO_2 evolution peak. For the 4.8 – 1.5 V cell, an additional sharp peak of CO_2 evolution is observed at the end of charge, reaching a maximum CO_2 evolution rate that is roughly the same as the maximum CO_2 evolution rate of the first peak.

For the cells discharged to 1.85 V vs. Li/Li^+, CO_2 evolution also begins immediately upon the start of the subsequent charge, although to a notably lesser extent than for the cells discharged to 1.5 V. The CO_2 evolution rate during early charging (<4.6 V) barely stands

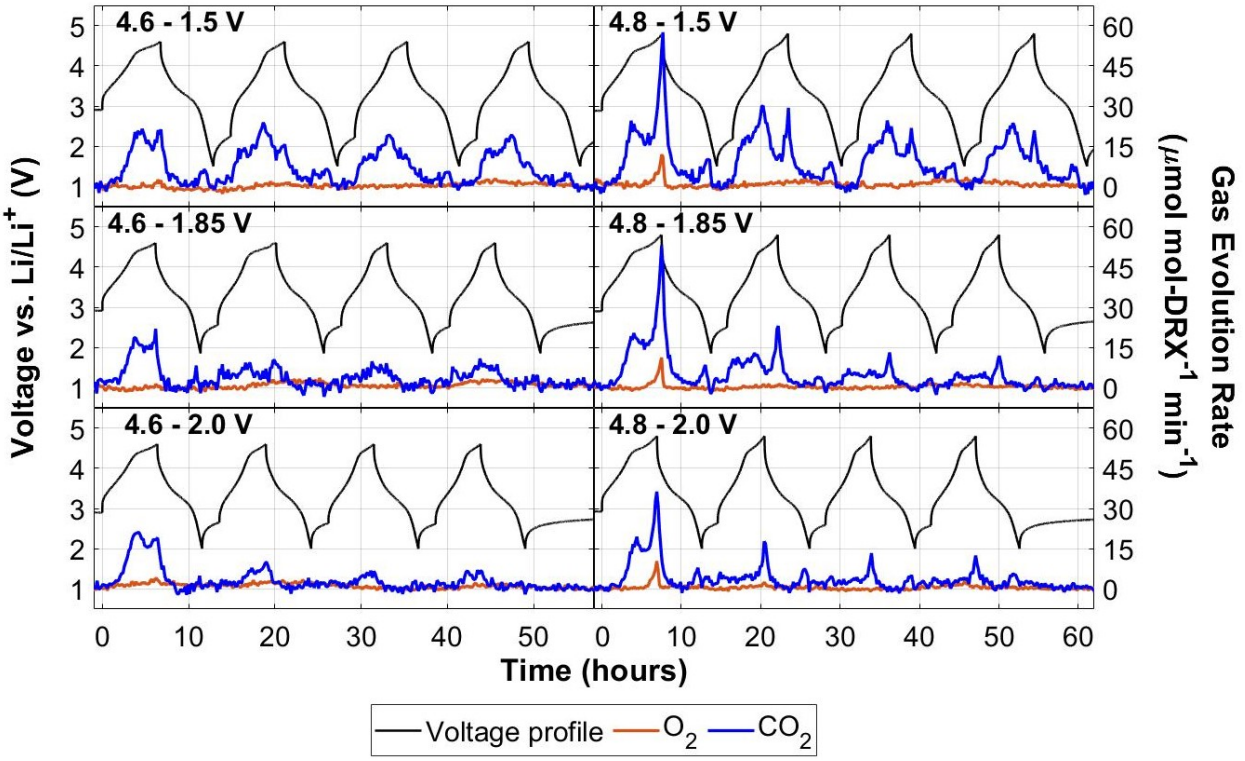

Figure 4.1: O_2 and CO_2 evolution results measured by DEMS during the first four cycles of LMTO in six unique voltage windows. The voltage windows selected are each combination of two charging cut-off voltages (4.6 V, 4.8 V) and three discharging cut-off voltages (1.5, 1.85, 2.0 V). All cells were cycled at a constant current of 0.1 Li hr^{-1} (32.9 mA g-LMTO^{-1}). The electrolyte was 1M $LiPF_6$ in 3:7 EC:EMC.

out from the baseline, resulting in a small, broad peak of CO_2 evolution. For the 4.6 – 1.85 V cell, no additional CO_2 evolution is observed outside of the broad CO_2 evolution peak. For the 4.8 – 1.85 V cell, an additional sharp peak of CO_2 evolution is observed at the end of charge that resembles the end-of-charge CO_2 evolution peak in the 4.8 – 1.5 V cell.

Lastly, for the cells discharged to 2.0 V, there is negligible CO_2 evolution at voltages below 4.0 V during the subsequent charges. For the 4.6 – 2.0 V cell, a small broad CO_2 evolution peak is observed above 4.0 V. For the 4.8 – 2.0 V cell, a sharp peak of CO_2 evolution is observed at the end of charge that resembles the end-of-charge CO_2 evolution peak in the 4.8 – 1.5 V and 4.8 – 1.85 V cells.

Given that electrolyte degradation has far more significant implications than native carbonate decomposition for the long-term cycling stability of DRX materials, herein we focus our analysis on the CO_2 evolved after the first cycle. We posit that the CO_2 evolution observed during the second, third, and fourth charges can be divided into two categories:

high-voltage CO_2 evolution that is driven by purely oxidative conditions at the DRX surface during high-voltage charging, and mid-voltage CO_2 evolution which is exacerbated by low-voltage discharging on the previous cycle. The high-voltage CO_2 evolution fits within the typical understanding of CO_2 evolution driven by oxidative electrolyte degradation. This mode of CO_2 evolution can be clearly seen in the sharp high-voltage peaks of CO_2 evolution which only occur during charging above 4.6 V. In contrast, the mid-voltage CO_2 evolution is distinctly different from conventionally observed high-voltage CO_2. This additional mode of CO_2 evolution can be seen in the broad peaks of CO_2 evolution occurring early during charging which arise only after discharging below 2.0 V, with the magnitude of mid-voltage CO_2 evolution growing with decreasing lower cut-off voltage.

The dependence of the mid-voltage CO_2 evolution on a low-voltage discharge in the prior cycle indicates that some sort of reductive process occurs at the DRX surface at the end of discharge which leads to the mid-voltage CO_2 evolution on the following charge. Specifically, we hypothesize that this process may be reduction of ethylene carbonate to form some sort of solid carbonate-like species which gets deposited on the DRX surface. Depending on their exact nature, these reduced species on the DRX surface may subsequently be oxidized to evolve CO_2 during the following charge.

In addition to the CO_2 evolution observed during charging, we also observe a small amount of low-voltage CO_2 evolved at the end of discharge for all cells except the 4.6 - 2.0 V cell. Although this low-voltage CO_2 evolution has been observed before during cycling of Mn-based DRX materials, the reactivity underlying its occurrence remains unknown.[35] However, given our suspicion of some sort of reductive electrolyte degradation process occurring at the bottom of discharge, we suggest that the low-voltage CO_2 evolution arises due to the same reductive degradation that precedes the mid-voltage CO_2 evolution observed on the subsequent charge. This suggestion is further supported by the general coincidence of low-voltage CO_2 at the bottom of discharge and mid-voltage CO_2 on the subsequent charge. In other words, it would appear that both low-voltage and mid-voltage CO_2 arise due to low-voltage (1.5 - 2.0 V) instability at the cathode-electrolyte interface near the end of discharge.

Importantly, the CO_2 evolution originating from electrolyte degradation after the first cycle appears to persist with minimal attenuation during early cycling of LMTO, indicating that LMTO does not passivate with respect to the electrolyte degradation. This sustained electrolyte degradation is likely to drive a number of deleterious processes within the cell, including depletion of the electrolyte, deposition of insulating degradation products, and formation of reactive degradation products which may drive downstream degradation of other cell components. Ultimately, when allowed to persist over hundreds of cycles, it is likely that this degradation will cause significant performance decay in cells containing LMTO cathodes.

4.4.2 Extended Cycling in Electrolyte-lean Full-Cells

Given the sustained electrolyte degradation observed during early cycling and its strong dependence on voltage window, extended cycling experiments in customized electrolyte-lean full-cells were conducted to examine the extent to which electrolyte degradation contributes

to performance decay. Specifically, LMTO full-cells were cycled in the same voltage windows that were used for the DEMS experiments in Section 4.4.1 (4.6/4.8 - 1.5/1.85/2.0 V vs. Li/Li^+). If the differences in interfacial degradation observed between the different voltage windows via DEMS have a strong impact on the cycling performance, then corresponding differences in performance decay between the voltage windows should be observed over long-term cycling.

Full-Cell Design

The customized electrolyte-lean full-cells were assembled in coin cells. The anode was a pre-formed, 40% pre-lithiated graphite electrode with a total capacity roughly three times greater than the capacity of the DRX cathodes studied in this work. Graphite was chosen given its standard use in Li-ion batteries, as well as its ability to serve as a low-voltage electrode material with a relatively stable potential. The graphite electrodes first underwent formation cycling in half-cells to minimize the effects of graphite interfacial formation during full-cell cycling, and they were left in a 40% pre-lithiated state to anchor the graphite electrode at a low potential (0.1 - 0.01 V vs. Li/Li^+) so that the cell potential could be used to estimate the DRX potential during cycling. For all full-cells, the electrolyte was 1M $LiPF_6$ in 3:7 EC:EMC with a loading of 30 μL cm^{-2} (relative to the cathode area), which is roughly half of the electrolyte loading used in the DEMS cells discussed previously. Additionally, the separator consisted of a single sheet of polypropylene. The results of the formation and pre-lithiation of the graphite electrodes are presented in Section 4.6.2.

These customized electrolyte-lean full-cells, as opposed to the electrolyte-flooded half-cells used in the DEMS experiments, were selected for the long-term cycling experiments in order to expose the effects of interfacial degradation on cycling performance. In electrolyte-flooded half-cells, the Li metal anode provides a large reservoir of active Li to replace any Li lost to degradation products (i.e. LiF, Li_2CO_3), and the large excess of electrolyte serves to mitigate the effects of electrolyte depletion and dilute any reactive degradation products formed. These features are well suited for the investigation of interfacial degradation processes during initial cycling via DEMS, but they are poorly suited for exposing the effects of this degradation on extended cycling performance. In the customized electrolyte-lean full-cells, on the other hand, a partially pre-lithiated graphite provides just a small amount of excess active Li, and the reduced amount of electrolyte is more sensitive to electrolyte degradation. Another key difference between full cells housed in coin cells and DEMS half cells is that any gases evolved during a DEMS measurement are swept out of the cell during gas analysis, whereas coin cells are hermetically sealed, allowing gases to accumulate and participate in electrochemical processes during cycling. These characteristics make the electrolyte-lean full-cells better suited to expose the effects of interfacial degradation on performance decay.

Capacity Retention Analysis

The discharge capacities in each voltage window during extended cycling are shown in Figure 4.2. The discharge capacities during the first three cycles are notably higher during than those during the remaining cycles, which is expected given the slower rate and reduced overpotentials. On the fourth cycle, for which the cycling rate is raised to 0.1 Li hr^{-1}, the discharge capacities are in the range of 160-225 mAh g-$LMTO^{-1}$. The relative capacities of the six cells are consistent with what would be expected based on the different voltage windows, with the 4.8 - 1.5 V cell showing the highest initial capacity and the 4.6 - 2.0 V cells showing the lowest initial capacity. The charge capacities are omitted from Figure 4.2 for clarity, but they closely follow the discharge capacities for each cell throughout the entire experiment. We note that there are regularly occurring data points showing reduced discharge capacity for all six cells. These data points are from the cycles in which EIS measurements were taken, indicating that the different rest procedure employed on these cycles interfered with the dynamics of the cell. Given the return of the cell capacity to its original trajectory on the next cycle, we expect that this interference had a negligible impact on the outcome of the cycling experiment.

During extended cycling, all six cells suffer significant capacity decay. During the first 30 cycles, all cells show a gradual loss in capacity of roughly 20 mAh g-$LMTO^{-1}$. Starting around the 30th cycle, however, the capacity retention of the cells begins to diverge. The cells charged to 4.8 V show the most significant capacity decay. The cell cycled in the voltage window of 4.8 - 1.5 V shows the earliest and greatest loss in capacity, with a rapid drop in capacity from ∼200 to ∼50 mAh g-$LMTO^{-1}$ taking place between the 30th and the 100th cycle. The cells cycled in the voltage windows of 4.8 - 1.85 V and 4.8 - 2.0 V show a more delayed decay in capacity, with a drop in capacity from ∼180 to ∼50 mAh g-$LMTO^{-1}$ taking place between the 30th and the 140th cycle. Compared to the cells charged to 4.8 V, the cells charged to 4.6 V possess significantly improved stability. The cell cycled in the voltage window of 4.6 - 1.5 V maintains a gradual decay in capacity up to the 80th cycle, at which point the capacity begins to decline more rapidly, falling from ∼160 to ∼100 mAh g-$LMTO^{-1}$ from the 80th to the 204th cycle. Finally, the cells cycled in the voltage windows of 4.6 - 1.85 V and 4.6 - 2.0 V exhibit a gradual rate of capacity decay throughout the cycling experiment, maintaining a capacity of ∼110 mAh g-$LMTO^{-1}$ after 204 cycles. Notably, the cells with the narrowest voltage windows (4.6 - 1.85 V and 4.6 - 2.0 V) and lowest initial capacities possess the highest capacities after 204 cycles.

Based on these results, it is clear that the voltage windows studied in this work have a strong impact on capacity decay during cycling. For the voltage windows studied herein, the rate of capacity decay increases with increasing upper cut-off voltage and decreasing lower cut-off voltage. Increasing the upper cut-off voltage has the most deleterious effect on capacity decay, as all of the cells charged to 4.8 V show faster and greater capacity decay than any of the cells charged to 4.6 V. The effect of decreasing the lower cut-off voltage can be seen in the way that, for a given upper cut-off voltage, the rate of capacity decay increases with decreasing lower cut-off voltage. This effect appears particularly pronounced

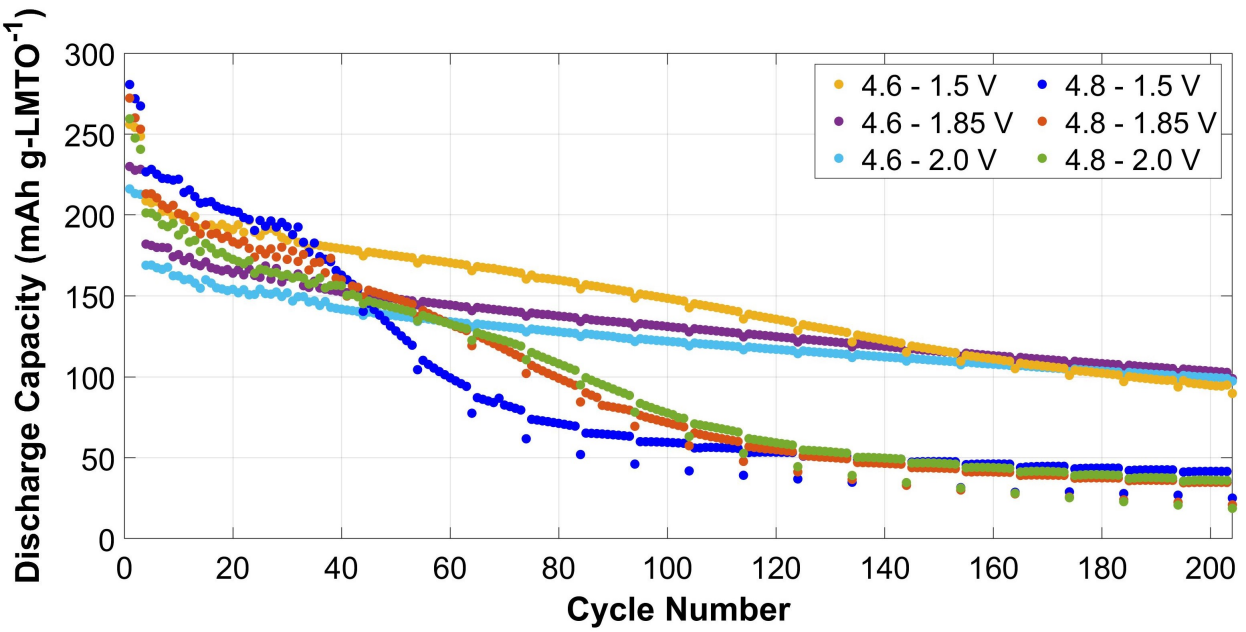

Figure 4.2: Discharge capacities of LMTO-graphite full-cells during constant current cycling in different voltage windows. The first three cycles were conducted at a slow rate of 10 mA g-LMTO^{-1}, and the remaining cycles were conducted at a rate of 0.1 Li hr^{-1} (32.9 mA g-LMTO^{-1}). After each discharge, the cell was allowed to rest on open circuit for two hours before the subsequent charge began. For all cells, the electrolyte was 1M $LiPF_6$ in 3:7 EC:EMC.

for the cells discharged to 1.5 V, whereas the differences in capacity decay between cells with the same upper cut-off voltage and lower cut-off voltages of 1.85 and 2.0 V are not as severe. These trends indicate that additional degradation takes place as a result of charging above 4.6 V and discharging below 2.0 V, which is fully consistent with the outgassing results presented in Section 4.4.1. Therefore, we hypothesize that the additional electrolyte degradation brought about by cycling to the extreme ends of the voltage window are the cause of the elevated capacity loss when charging above 4.6 V or discharging below 2.0 V.

Differential Capacity Analysis

The electrochemical performance of the full-cells during cycling can be further analyzed by plotting differential capacity profiles (dQ dV^{-1} vs. V, where Q is capacity) from selected cycles throughout the experiment. Figure 4.3 shows the differential capacity profiles for all six cells on the 5th, 40th, 80th, 120th, 160th, and 200th cycles. The fifth cycle was selected as it corresponds to the first cycle at the increased rate (0.1 Li hr^{-1}) with a standard rest procedure (no EIS measurements), and the remaining cycles were selected to evenly sample

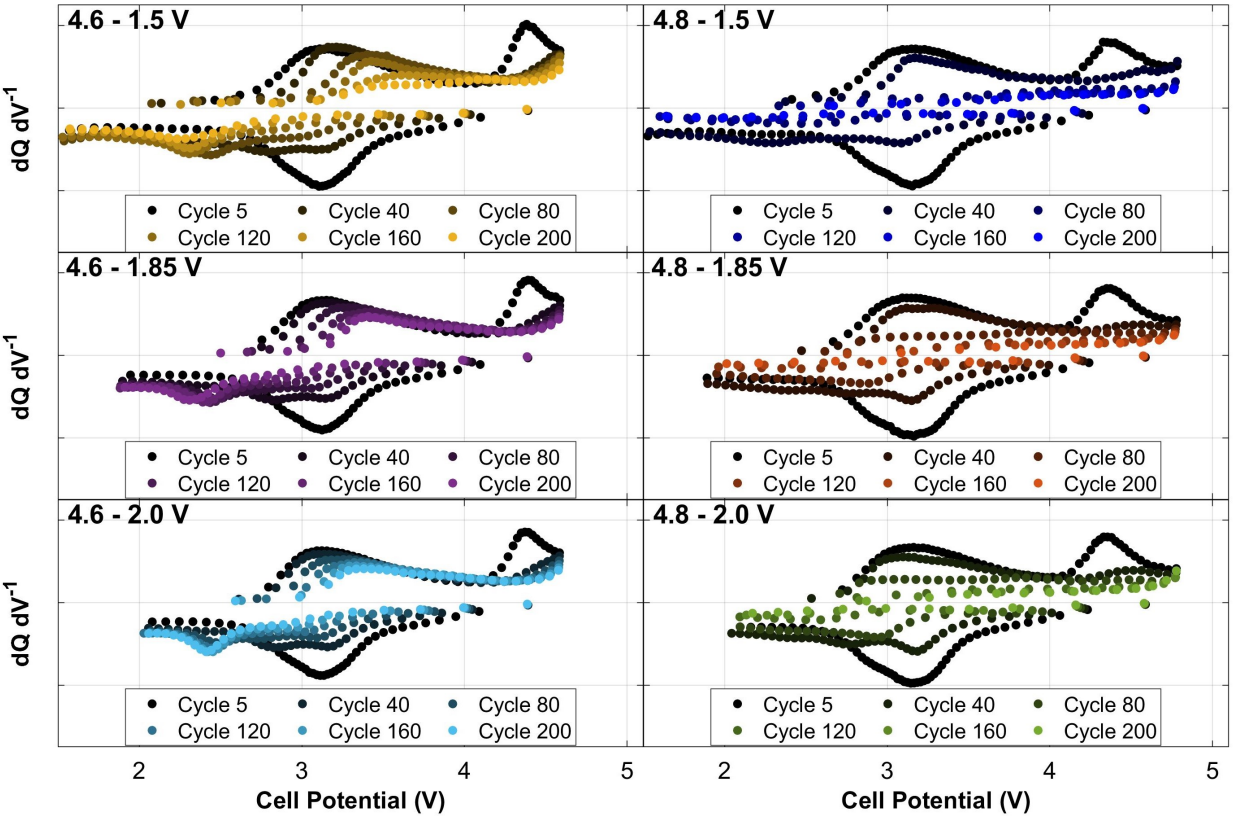

Figure 4.3: Differential capacity profiles in different voltage windows on selected cycles. For all cycles depicted, constant current cycling at a rate of 0.1 Li hr^{-1} was conducted in the listed voltage profile. The electrolyte for all cells was 1M $LiPF_6$ in 3:7 EC:EMC.

the entire cycling experiment. On the fifth charge, all six cells show two major oxidative peaks centered around 3.2 and 4.4 V, which correspond to bulk $Mn^{3+/4+}$ and oxygen redox, respectively. On the fifth discharge, all cells show one broad reductive peak centered around 4.1 V vs. Li/Li^+, which is considered to correspond to intermixed $Mn^{3+/4+}$ and oxygen redox processes.[55] The differential capacity profiles for the six cells on the 5th cycle closely resemble one another, with minor differences at the ends of the voltage windows due to the differences in cut-off voltages. The similarity of the 5th cycle differential capacity profiles for the different cells demonstrates that initial cell-to-cell variation is small.

By the 40th cycle, diverging cell performance driven by differences in interfacial degradation is clearly observed. Growing cell polarization and a loss in low voltage capacity are clearly seen by tracking the transformation of the oxidative $Mn^{3+/4+}$ peak for each cell. For the cells charged to 4.8 V, the oxidative $Mn^{3+/4+}$ peak quickly diminishes in size and shifts towards higher voltages. Within this subset, the cell cycled in the window of 4.8 - 1.5 V appears to decrease most in size and shift the most towards higher voltages. This effect is

observed in the cells charged to 4.6 V as well, although it occurs more slowly with cycling.

As cycling continues, these effects grow stronger. By the 80th cycle, the cells charged to 4.8 V have lost the majority of their low-voltage capacity associated with Mn^{3+} oxidation, causing the oxidative $Mn^{3+/4+}$ peak to transform into a flattened plateau. While performance decay occurs at a slower rate during cycling for the cells charged to 4.6 V, the loss in capacity and increasing cell polarization are still evident. The oxidative and reductive peaks continue to shrink in size and shift towards higher and lower voltages, respectively. Of the cells charged to 4.6 V, this effect is most pronounced in the 4.6 - 1.5 V cell, reflecting the elevated degradation brought about by the low-voltage discharge.

Throughout the remainder of the cycling experiment, the symptoms of cell degradation grow stronger. The oxidative and reductive features of each differential capacity profile continue to grow flatter and shift towards higher and lower voltages, respectively. By the 200th cycle, all three cells charged to 4.8 V show very flat differential capacity profiles with little to no definition. At the same point, the cells charged to 4.6 V all show significant polarization. Furthermore, the 4.6 - 1.5 V cell suffers a significant loss in capacity in the voltage range of 3.2 - 3.8 V between cycles 120 and 200, consistent with the cell's decline in total discharge capacity shown in Figure 4.2.

The differential capacity analysis lends additional information that cannot be gleaned from the capacity retention data shown in Figure 4.2 alone. Based on the transformations observed in the differential capacity profiles during cycling, it appears that the loss in total discharge capacity stems from a loss in low-voltage capacity and an increase in cell polarization. Based on the correlation of these symptoms with the electrolyte degradation observed via outgassing across different voltage windows, we expect that electrolyte degradation leads to the formation and deposition of insulating, inactive, Li-containing species (i.e. LiF, Li_2CO_3). The formation of these inactive Li-containing species would deplete the amount of active Li in the cell, thereby preventing full re-lithiation of the cathode on discharge and making the low-voltage capacity inaccessible. Furthermore, these inactive Li-containing species would likely deposit on the surfaces of the electrodes, leading to impedance rise in the cell and increasing the polarization observed during cycling.

Comparison of Cell Impedance Growth in Different Voltage Windows

Alongside the differential capacity analysis, examining changes in the cell impedance using the results of the EIS measurements sheds additional light on the manner in which performance decay occurs during cycling. Figures 4.4 and 4.11 display the Nyquist plots obtained from EIS measurements from selected cycles of each cell in the charged and discharged states, respectively. All EIS measurements show a single semicircle at high frequencies and a Warburg impedance tail at low frequencies. Importantly, the size of the semicircle indicates the magnitude of interfacial and charge-transfer resistance within the cell.[39,117] While the cell impedance grows steadily with cycling for all six cells, the rates of impedance growth are drastically different depending on the voltage window. The cells charged to 4.8 V show the highest rates of impedance growth, and among these cells the rate of impedance growth

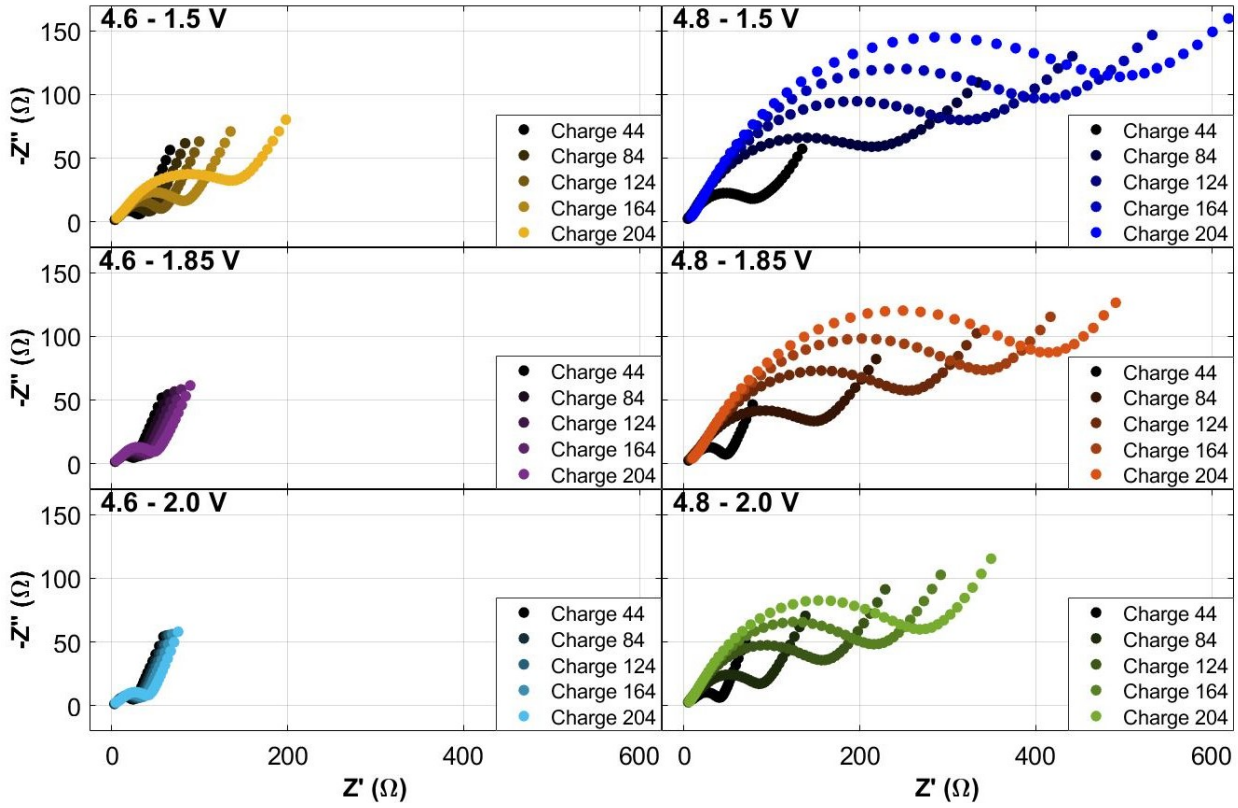

Figure 4.4: Nyquist plots obtained from EIS measurements of each cell on selected cycles, taken in the charged state. EIS spectra were collected with a voltage amplitude of 5 mV in the frequency range of 20 kHz to 100 mHz. For each cycle, three scans were taken and averaged together to minimize error. The electrolyte used in all experiments was 1M $LiPF_6$ in 3:7 EC:EMC.

increases with decreasing lower cut-off voltage. For the cells charged to 4.6 V, the 4.6 - 1.5 V cell shows a significantly higher rate of impedance growth than the 4.6 - 1.85 V and 4.6 - 2.0 V cells. Interestingly, the 4.6 - 1.85 V and 4.6 - 2.0 V cells show very similar rates of impedance growth. Clearly, charging to 4.8 V and discharging to 1.5 V both lead to greatly increased rates of impedance growth over cycling. Given that the rate of impedance growth is greater for the 4.8 - 2.0 V cell than for the 4.6 - 1.5 V cell, it appears that charging to 4.8 V is more deleterious with respect to impedance growth than discharging to 1.5 V.

The observed dependence of impedance growth on voltage window indicates that cycling to the extreme voltages incurs an elevated rise in impedance. This finding is fully consistent with the changes in cell polarization observed in the differential capacity analysis. Given the occurrence of this additional performance decay in voltage windows that also exhibited elevated electrolyte degradation (as demonstrated in Section 4.4.1), we expect that the ac-

celerated rise in cell impedance is driven by the heightened electrolyte degradation at the cathode-electrolyte interface. As discussed previously with regard to the differential capacity analysis, it is likely that electrolyte degradation leads to the deposition of insulating species, such as Li_2CO_3 and LiF, on the surfaces of the electrodes. This additional layer of insulating electrolyte degradation products would impede Li transport across the electrode-electrolyte interfaces, raising the cell impedance as observed.

4.4.3 Post-Mortem Cell Analysis

Following completion of the long-term cycling experiments, all six full-cells were disassembled to allow for 'post-mortem' analysis of the individual cell components. Both electrodes were extracted from each coin cell, rinsed with DMC, and dried under vacuum at room temperature. Half-cell cycling experiments were performed with both the cathode and anode from each cell, and the cathode half-cell cycling was conducted using the DEMS instrument to examine outgassing during cycling. Additionally, ICP-OES was used to quantify the amount of Mn and Ti in the cathode, separator, and anode, providing information about the extent of transition metal dissolution in each cell.

Post-Mortem DEMS with LMTO Cathodes

During the post-mortem DEMS experiments, the LMTO electrodes extracted from full-cells after long-term cycling were cycled for 5 full cycles against Li metal with the same voltage window and current used during the long-term cycling experiments. The results of the post-mortem DEMS experiments, including the cell voltage profiles and gas evolution profiles for CO_2 and H_2, are displayed in Figure 4.5.

Before focusing on the gas evolution, we examine the electrochemical performance of the DRX cathodes in the post-mortem DEMS half-cells. Of note, the first discharge capacity is higher than the first charge capacity for each LMTO cathode, indicating that the cathodes become partially relithiated during cycling in the half-cell used for DEMS. This can be seen by comparing the voltage profiles for first charge and discharge for each electrode in Figure 4.5, which are also plotted clearly in Figure 4.12. The partial relithiation of the LMTO cathodes during cycling in half-cells with fresh electrolyte indicates that a key limitation for the capacity during full-cell cycling was the supply of active Li. With limited amounts of active Li in the full-cell after extensive degradation, the graphite electrode becomes delithiated at the end of discharge, and its rising potential causes the cell to reach its lower cut-off potential with the cathode potential well above the originally intended lower cut-off voltage. Upon switching to the half-cell in which the Li metal anode supplies a large excess of Li pinned at a potential of $\sim$0 V vs. Li/Li^+, the LMTO cathode is able to reach the state of lithiation associated with its originally intended lower cut-off voltage, resulting in partial relithation during cycling. Despite this partial relithiation, the LMTO cathodes do not recover their full capacities. After several cycles in the half-cells, the LMTO capacities stabilize in the range of 75-90 mAh g-$LMTO^{-1}$ for all six electrodes. These capacities are roughly 30-50% of the

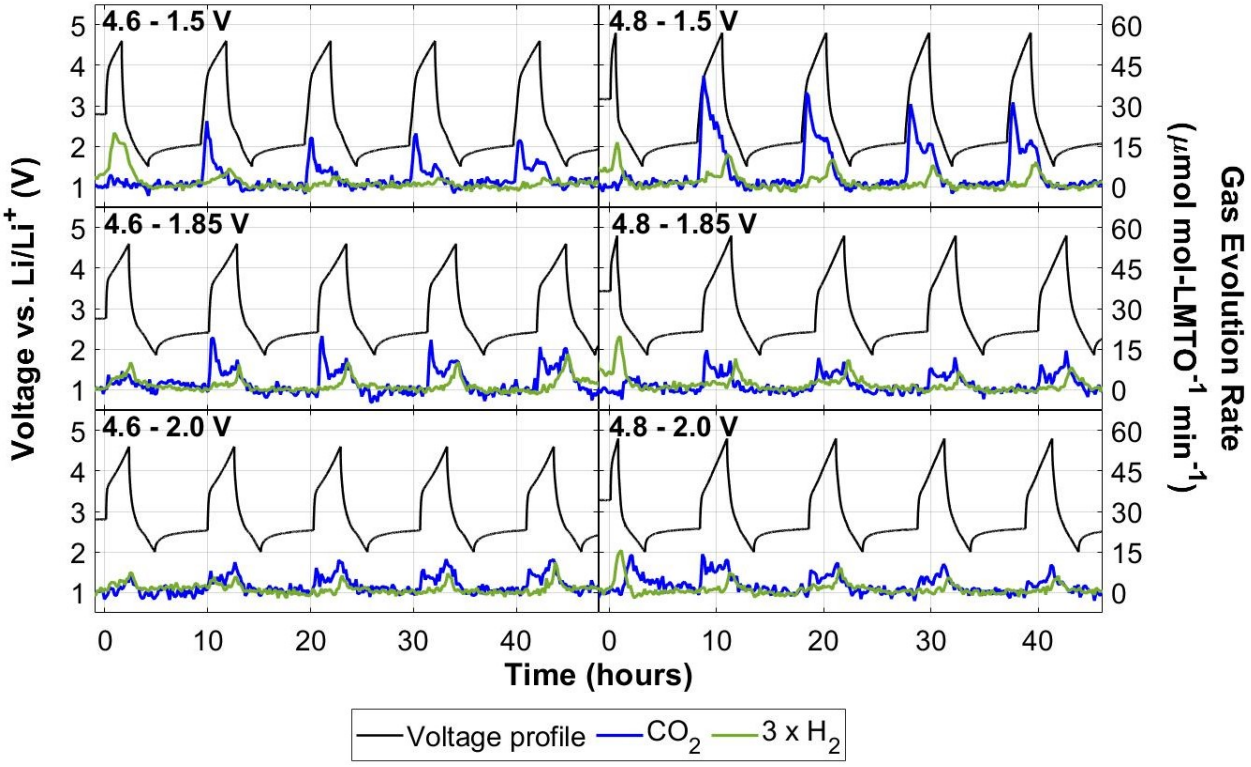

Figure 4.5: CO_2 and H_2 (multiplied by a factor of three for ease of comparison) evolution results from post-mortem DEMS experiments conducted on LMTO electrodes after long-term cycling. Cycling during DEMS experiments was conducted at a constant rate of 0.1 Li hr^{-1} (32.9 mA g-LMTO^{-1}, based on the initial cathode loading before long-term cycling) with a 5 hour rest after each discharge. For all post-mortem DEMS cells, the counter-electrode was Li metal and the electrolyte was 1M $LiPF_6$ in 3:7 EC:EMC.

capacities achieved during initial cycling of the LMTO cathodes, indicating that something besides the supply of active Li limits the capacity of the LMTO cathodes from increasing any further. Other possible factors that may limit the capacity of the LMTO cathodes during post-mortem cycling include kinetic barriers due to the high impedance of the cycled LMTO cathodes or simple loss of LMTO material through extensive dissolution of transition metals during long-term cycling. The latter possibility will be addressed in a later section using ICP-OES to examine Mn/Ti dissolution in the full-cells.

During the post-mortem DEMS experiments, significant and persistent evolution of both CO_2 and H_2 was observed. As discussed previously, CO_2 evolution arises due to decomposition of both native carbonates and the carbonate solvents in the electrolyte. Given that the cathodes have already undergone long-term cycling, the CO_2 evolution observed in the post-mortem DEMS experiments must be related to electrolyte degradation. The CO_2 evolution

observed during post-mortem DEMS shows many similarities to that observed during initial cycling of LMTO cathodes in Section 4.4.1. Specifically, like the outgassing observed during initial cycling, the CO_2 evolution appears to arise in two main categories: mid-voltage CO_2 that evolves early during each charge, and high-voltage CO_2 that evolves at the end of charge. The mid-voltage CO_2 evolution is exacerbated by low-voltage discharging on the previous cycle, whereas the high-voltage CO_2 evolution appears to originate from purely oxidative electrolyte degradation on the cathode surface. As explained previously, the dependence of mid-voltage CO_2 evolution on low-voltage discharging on the previous cycle indicates that some sort of reductive interfacial reaction occurs at low voltages during discharging.

Because the LMTO cathodes were unable to reach a low-voltage in the full-cells towards the end of the long-term cycling experiment due to a lack of active Li, the first charge in the post-mortem DEMS cell shows very little mid-voltage CO_2. After the first discharge against a Li metal counter-electrode, the mid-voltage CO_2 evolution resumes on the second charge for each cell. Interestingly, the mid-voltage CO_2 evolution is observed for all six cells during post-mortem DEMS, whereas it was not observed to a significant extent for the cells with a 1.85/2.0 V lower cut-off voltage during initial cycling DEMS. The elevated mid-voltage CO_2 evolution for LMTO cathodes discharged to 1.85/2.0 V after long-term cycling indicates that the reductive interfacial reaction that precedes mid-voltage CO_2 begins to occur at slightly higher voltages (>2.0 V) after extended cycling. Furthermore, the mid-voltage CO_2 evolution peaks observed during post-mortem DEMS appear much sharper than those observed during initial cycling. We attribute this difference to the transformation in the cell voltage profile over long term cycling. After long-term cycling, the LMTO cathode spends much less time below 4 V during charging, causing the gas evolution processes occurring early during charging to crowd together and thereby sharpening the mid-voltage CO_2 evolution peak.

For all cells, the high-voltage CO_2 evolution appears fairly similar when compared to the outgassing observed during initial cycling. The values of the gas evolution rates at the end of charge for the same voltage window in initial and post-mortem DEMS values are quite close, indicating similar rates of electrolyte degradation. Although the high-voltage CO_2 evolution peaks during post-mortem cycling stand out less distinctly than those observed during initial cycling for the cells charged to 4.8 V, we ascribe this to a convolution of the high-voltage CO_2 evolution peak with the larger mid-voltage CO_2 evolution peak during post-mortem cycling due to the shortened charging times.

H_2 evolution is also observed for all six cells during charging of the LMTO cathodes above $\sim$4 V. High-voltage H_2 evolution arises from an electrode crosstalk process involving oxidative electrolyte degradation producing soluble protic species at the LMTO surface coupled with reduction of the protic species to form H_2 at the Li metal surface. Consequently, the H_2 evolution detected by DEMS is a downstream product of electrolyte degradation at the LMTO surface. Interestingly, H_2 evolution was not detected the during initial cycling DEMS experiment, indicating that LMTO reactivity towards the electrolyte degradation process yielding protic species increases during long-term cycling.

We observe little to no dependence of the H_2 evolution on the upper cut-off voltage

employed during cycling. While the 4.6 - 1.5 V cell shows little H_2 evolution after the first charge, the remaining cells show comparable amounts of H_2 evolution during post-mortem cycling. In fact, the 4.6 - 1.85 V cell shows the largest H_2 evolution peaks, which is unexpected based on its relatively moderate voltage window. This lack of dependence of H_2 evolution indicates that the electrolyte degradation process that precedes H_2 evolution readily occurs well below 4.6 V, which is consistent with the onset of H_2 evolution observed at roughly $\sim$4 V. Additionally, given the small amount of capacity between 4.6 V and 4.8 V during post-mortem DEMS, the cells charged to 4.8 V spend very little time above 4.6 V. Therefore, these two factors, the onset of H_2 evolution around 4 V and the small amount of time spent above 4.6 V during charging to 4.8 V, combine to make the extent of H_2 evolution appear rather independent of the upper cut-off voltage.

The CO_2 and H_2 evolution observed during post-mortem DEMS highlights the unpassivated reactivity at the LMTO-electrolyte interface after extended cycling. The electrolyte degradation processes that underlie CO_2 and H_2 evolution must form additional organic electrolyte degradation products from the remaining portion of the carbonate solvent molecules, which may deposit on the electrode surface or react with the electrolyte salt to consume Li. Furthermore, the protic species that are ultimately reduced to form H_2 at the anode are likely to be reactive in their transit across the electrolyte. Protic species, such as H_2O and alcohols, react with $LiPF_6$ to yield HF and PF_5. HF can subsequently react with several cell components, driving transition metal dissolution from the LMTO material and decomposing interfacial species such as Li_2CO_3 on both electrodes to produce H_2O, CO_2, and LiF.[102,104] In addition to feeding back into the reaction with $LiPF_6$, H_2O can also drive solvent hydrolysis to form CO_2 along with alcohols.[42,43] Similar to H_2O, these alcohols may feed back into the degradation cascade via reaction with $LiPF_6$. At the anode surface, meanwhile, the reduction of protic species (HF, H_2O, alcohols) to form H_2 is likely to draw Li out of the anode and deposit Li-containing insulating species. This network of chemical reactions resulting from electrolyte degradation is depicted in the schematic shown in Figure 4.6. Over extended cycling, these degradation reactions would drive the deposition of insulating, Li-containing, electrochemically-inactive species on the surfaces of each electrode. This process would cause both a loss of active Li and an increase in cell impedance, consistent with the decay in cell performance observed during long-term cycling in full-cells.

Post-Mortem Analysis of Graphite Electrodes

The graphite electrodes extracted from the full-cells after long-term cycling were cycled in graphite-Li coin cells to isolate their electrochemical performance. The voltage profiles for the graphite electrodes during post-mortem cycling are plotted in Figure 4.7, with each plot label indicating the voltage window that was used for the full-cell in which the graphite electrode was previously cycled.

The first delithiation reveals the state of lithiation for each graphite electrode at the end of long-term cycling in full-cells (after the 204th discharge). For the graphite electrodes cycled in full-cells with an upper cut-off voltage of 4.8 V, the first delithiation is very short, such

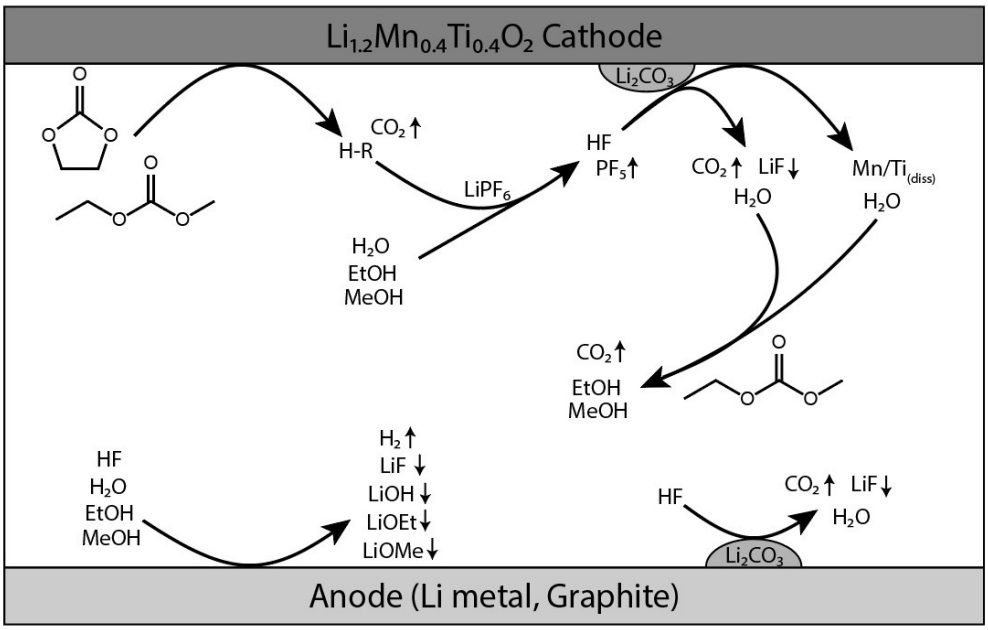

Figure 4.6: Schematic depicting the network of chemical reactivity initiated by electrolyte degradation at the LMTO-electrolyte interface. Reactions span the entire cell, including the LMTO surface, the electrolyte, and the anode surface. Upward pointing arrows next to species indicate gaseous species that may evolve from the cell, whereas downward pointing arrows indicate solid species that may deposit on electrode surfaces. The carbonate solvents depicted are ethylene carbonate and ethyl methyl carbonate, which are the electrolyte solvents used in this work.

that it is hard to see on the scale of the other voltage profiles. Although the first delithiation is longer for the graphite electrodes cycled in full-cells with an upper cut-off voltage of 4.6 V, it is still rather short compared to the graphite pre-lithiation capacity. Furthermore, the capacity associated with the first delithiation for the graphite electrodes cycled in full-cells with an upper cut-off voltage of 4.6 V decreases with decreasing lower cut-off voltage.

The capacity results from the first delithiation of the graphite electrodes indicate that the graphite electrodes become gradually delithiated over extended cycling, which is consistent with the observation that the full-cells suffer from a loss of active Li during extended cycling. Furthermore, the graphite lithiation is closely correlated with the amount of capacity lost during cycling. As shown in Figure 4.2, all three cells charged to 4.8 V experience a similar loss in discharge capacity during long term cycling. After long-term cycling, the graphite from these electrodes are found to be nearly fully delithiated after long-term cycling. In the case of the three cells charged to 4.6 V, the 4.6 - 1.5 V cell loses significantly more capacity than the 4.6 - 1.85 V/4.6 - 2.0 V cells. Correspondingly, the graphite electrode from the 4.6 - 1.5 V cell is significantly more delithiated than the graphite electrodes from the 4.6 - 1.85

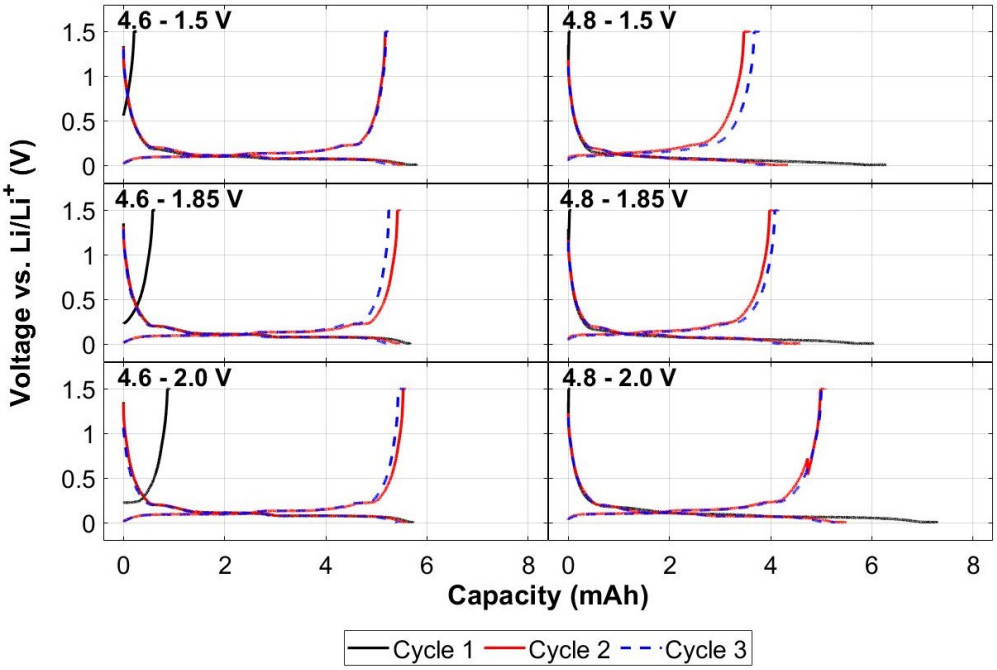

Figure 4.7: Voltage profiles during post-mortem cycling of graphite electrodes after long-term cycling in full-cells. Graphite electrodes were cycled in the voltage window of 1.5 - 0.01 V vs. Li/Li^+, with delithiation occurring first. Each delithiation and lithiation consisted of a constant current portion at a rate of 100 μA until the cut-off voltage was reached followed by a potentiostatic hold at the cut-off voltage for 5 hours. The electrolyte was 1M $LiPF_6$ in 3:7 EC:EMC. Each plot label indicates the voltage window that was used for the full-cell in which the graphite electrode was previously cycled.

V/4.6 - 2.0 V cells.

Referring to the voltage profiles for the remainder of the experiment, a large recovery in capacity is observed for all six graphite electrodes during cycling against Li metal. For the graphite electrodes from cells charged to 4.6 V, the capacities observed on the second and third cycles are nearly identical to those measured for the same electrodes in the pristine state, indicating that the graphite remains largely unharmed by the cycling-induced degradation. In the case of the graphite electrodes from the cells charged to 4.8 V, the capacities on the second and third cycle do not fully recover to the value from the pristine state, indicating that some loss in bulk graphite occurs due to cycling-induced degradation. The loss in graphite capacity increases with decreasing lower cut-off voltage, consistent with the trend in interfacial degradation across voltage windows. Nevertheless, this recovery in capacity confirms that the supply of active Li was a limiting factor for full-cell capacity.

Of note, for the graphite electrodes cycled in full-cells with an upper cut-off voltage of 4.8 V, the capacity associated with the first lithiation shows a large irreversible capacity.

This excess capacity is likely due to irreversible reduction processes on the graphite surface. Since the electrodes have undergone pre-formation as well as extended cycling, it is unlikely that these irreversible formation processes are conventional reduction processes associated with graphite-electrolyte interfacial formation. Furthermore, given that the electrodes on which these irreversible processes occur are those which were cycled in full-cells with an upper cut-off voltage of 4.8 V, it is likely that the additional degradation brought about by charging to 4.8 V during long-term cycling caused a change to the graphite surface that drives additional interfacial reactions at low voltages. One possible explanation is that transition metal dissolution occurs to a greater extent for the cells charged to 4.8 V during long-term cycling, leading to deposition of transition metals on the graphite surface. These deposited transition metals may then catalyze electrolyte reduction at the graphite surface during post-mortem cycling. This hypothesis will be explored further in a later section, in which transition metal dissolution will be quantified for each full-cell.

After post-mortem cycling, the graphite electrodes were extracted from their coin cells and prepared for acid titration with TiMS. The graphite titration results are given in Table 4.2. Importantly, the titrations reveal that the amount of carbonate on the surface of the graphite electrode after cycling increases with increasing upper cut-off voltage and decreasing lower cut-off voltage used during full-cell cycling. Given the correlation of electrolyte degradation observed via DEMS and graphite surface carbonate quantities observed via TiMS across voltage windows, these results suggest that the heightened electrolyte degradation at the LMTO surface brought about by cycling to the extreme ends of the voltage window elevates the deposition of carbonate species on the anode surface. This finding is consistent with the cell degradation observed throughout this work, demonstrating the role of electrolyte degradation in depleting active Li and depositing insulating species on the electrode surfaces. Interestingly, this process also necessitates some form of cross-talk process wherein degradation at the LMTO surface drives deposition of carbonate at the graphite surface. A more detailed analysis of the graphite titration experiments, including an analysis of the H_2 observed during TiMS and possible explanations for the titration results, are provided in Section 4.6.5.

ICP-OES Analysis of Transition Metal Dissolution

ICP-OES was used to determine the extent to which transition metal (Mn and Ti) dissolution occurs in each full-cell. Upon disassembly of the full-cells, the separator from each cell was extracted and dried under vacuum. After post-mortem DEMS, the LMTO cathodes were extracted, rinsed in DMC, and dried under vacuum. After aqueous titration of each graphite electrodes, 1.9 mL of the titration solution was collected from the titration vessel. For the dry samples (LMTO cathode, separator), each sample was soaked in 20 mL of an ICP matrix solution (2wt% HNO_3 and 0.1wt% $H_2C_2O_4$ in H_2O). For the samples of graphite titration solution, each sample was dissolved into 18.1 mL of the ICP matrix solution to yield a total solution volume of 20 mL. The concentrations of Mn and Ti in each resulting solution were then quantified using ICP-OES, and the results were used to determine the amount of each

transition metal in each phase. The amounts of Mn and Ti in each phase of the cell were then subtracted from the amounts of each metal in the pristine cathode, and the balance was categorized as unaccounted. Lastly, for each category (cathode, graphite, electrolyte, unaccounted), the amounts of Mn and Ti were normalized by the amount of each metal in the pristine cathode, providing the fraction of LMTO-originating Mn and Ti in each category. The results of this analysis are displayed in Figure 4.8.

The amounts of Mn and Ti found in the LMTO cathode samples reflect the amounts of each transition metal that remain undissolved after long-term cycling, whereas the amounts of Mn and Ti found in the electrolyte and graphite samples reflect the amounts of each transition metal that have dissolved from the LMTO cathodes. The Mn/Ti found in the electrolyte sample were likely to have remained dissolved in the electrolyte, whereas those found in the graphite sample were likely to have deposited on the graphite surface. Astoundingly, for all three cells charged to 4.8 V, ∼20-25% of the Mn/Ti is found on the graphite electrode after long-term cycling, and another ∼5% is found in the electrolyte. Mn/Ti dissolution appears to be less extensive, though still quite significant, for the three cells charged to 4.6 V. Of these, the 4.6 - 1.5 V cell shows the most Mn/Ti dissolution. For this cell, the graphite sample contained ∼10% of the Mn and ∼5% of the Ti, while the electrolyte sample contained another ∼4% of the Mn and Ti. For the 4.6 - 1.85 V and 4.6 - 2.0 V cells, the graphite samples ∼0-4% of the Mn/Ti, while electrolyte samples contained another ∼3-5% of the Mn/Ti. Lastly, for all six cells, the value for the unaccounted category was in the range of ∼15-25% of the Mn/Ti contained in the pristine cathode. We conjecture that the unaccounted transition metals likely were rinsed away by the DMC washes during the post mortem analysis, as discussed in more detail below.

Comparing the Mn/Ti dissolution results for each cell, the extent of transition metal dissolution shows a clear dependence on the voltage window used during cycling. The cells with an upper cut-off voltage of 4.8 V all display significantly more Mn/Ti dissolution than the cells with an upper cut-off voltage of 4.6 V, indicating that high-voltage charging is the primary driver of Mn/Ti dissolution. For a given charging cut-off voltage, increasing Mn/Ti dissolution is observed with decreasing lower cut-off voltage, indicating that low-voltage discharging increases the extent of Mn/Ti dissolution as well.

Rather than driving electrochemical processes that directly involve Mn/Ti dissolution, it is likely that high-voltage charging and low-voltage discharging have indirect effects on transition metal dissolution. One possible explanation is that the elevated electrolyte degradation brought about by these cycling parameters leads to the formation of reactive degradation products (i.e. HF) which drive transition metal dissolution. Another explanation is that, since high-voltage charging and low-voltage discharging are known to accelerate the loss of active Li, the cells with an upper cut-off voltage of 4.8 V and/or a lower cut-off voltage of 1.5 V may experience effects of anode slippage which lead to heightened high-voltage degradation. As the graphite electrode becomes gradually delithiated over cycling, the graphite electrode potential will rise. A rising graphite potential will require the LMTO cathode to charge to higher voltages for the cell to reach its upper cut-off voltage, driving elevated high-voltage degradation. Therefore, the cathodes cycled in cells with an upper cut-off voltage of

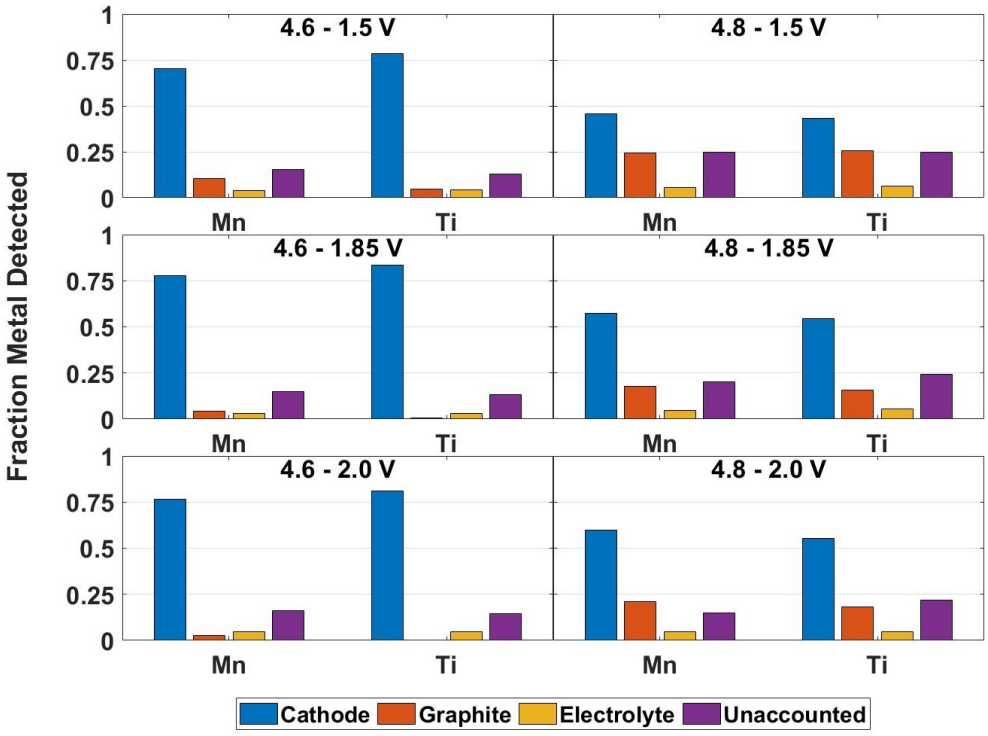

Figure 4.8: ICP-OES analysis of Mn and Ti dissolution after long-term cycling of full-cells. The cathode, graphite, and electrolyte categories represent the amounts of Mn/Ti that were found in the LMTO cathode, the graphite counter-electrode, and the separator after extended cycling. The unaccounted category represents the difference between the amounts of Mn/Ti in the pristine cathode and the sum of the amounts of Mn/Ti found in each cell phase after long-term cycling. All values are reported as a fraction of the amounts of Mn and Ti in the pristine cathode.

4.8 V and/or lower cut-off voltage of 1.5 V may reach voltages appreciably higher than those expected before significant loss of active Li. This upward migration of the LMTO potential over cycling will drive increasing degradation at the LMTO-electrolyte interface at the end of charge, leading to the formation of reactive degradation products that may subsequently cause transition metal dissolution via reaction with the LMTO surface.

Interestingly, regardless of the amount of Mn/Ti found in the graphite sample, the amount of Mn/Ti found in the electrolyte samples was always in the range of 3-6%. For instance, in the case of the 4.6 - 2.0 V cell, 0-2% of the Mn/Ti is found on the graphite electrode while 5% is found in the electrolyte. Meanwhile, for the 4.8 - 1.5 V cell, 18-21% of the Mn/Ti is found on the graphite electrode while still 5% is found in the electrolyte. This observation may indicate both a preference for the transition metals to reside in the electrolyte as well as a maximum solubility of the Mn/Ti in the electrolyte. These factors would explain the

widely varying distribution of Mn/Ti between the electrolyte and graphite samples for the different cells. During the early stages of Mn/Ti dissolution, the concentration of Mn/Ti in the electrolyte would remain low and allow the metals to remain dissolved in the electrolyte. However, as Mn/Ti dissolution proceeds and the concentration of Mn/Ti in the electrolyte reaches the solubility limit, further Mn/Ti dissolution from the LMTO surface would require deposition on the graphite surface.

Considering the unaccounted category, it is likely that the unaccounted Mn/Ti are lost during rinsing or post-mortem cycling of the electrodes. In either case, it is unclear whether these Mn/Ti would have been dissolved prior to full-cell disassembly. Loss of Mn/Ti during rinsing of the electrodes could occur due to washing of dissolved Mn/Ti species or, in the case of the cathode, physical dislodging of LMTO particles. Additionally, post-mortem cycling of the LMTO electrode in the DEMS cell could lead to the dissolution of additional Mn/Ti or the loss of LMTO particles that get stuck on the separator. Likewise, post-mortem cycling of the graphite electrode in the coin cell could lead to dissolution of deposited Mn/Ti or loss of Mn/Ti species that get stuck on the separator. Consequently, it is impossible to determine the extent to which the Mn/Ti in the unaccounted category should be considered as either dissolved or undissolved prior to full-cell disassembly, so we omit the unaccounted category when evaluating Mn/Ti dissolution.

The extensive Mn/Ti dissolution observed, especially in the case of the cells charged to 4.8 V, is certain to cause significant performance decay during cycling because a large portion of the cathode active material is lost. Along with providing direct evidence of the downstream consequences of interfacial degradation, the Mn/Ti dissolution results can be used to further evaluate the role of Mn/Ti dissolution in phenomena observed during the other post-mortem experiments. During post-mortem DEMS, all six LMTO cathodes displayed a partial recovery in capacity, with each cathode settling in the range of 75-90 mAh g-LMTO^{-1} after several cycles in the DEMS half-cell. Given the strong differences in Mn/Ti dissolution for the different LMTO cathodes, relative to the comparable recoveries in capacity, it is unlikely that Mn/Ti dissolution is the primary determining factor for the extent of capacity recovery. Additionally, during post-mortem cycling the graphite electrodes, a large irreversible capacity was observed during the first lithiation of the graphite electrodes from the full-cells cycled with an upper cut-off voltage of 4.8 V. This irreversible capacity coincides closely with high levels of transition metals deposited on the graphite surface, supporting the hypothesis that the irreversible capacity comes from electrolyte reduction processes catalyzed by the Mn/Ti species deposited on the graphite surface.

4.5 Conclusions

In this work, comparison across voltage windows was employed for LMTO to reconcile the interfacial degradation observed using DEMS with performance decay observed during long-term cycling. After long-term cycling, a thorough post-mortem analysis of the different cell components was used to evaluate the nature of the performance decay observed. It

was shown that high voltage charging (>4.6 V) and low voltage discharging (<2.0 V) each uniquely exacerbate interfacial degradation at the LMTO-electrolyte interface, leading to elevated rates of electrolyte degradation. These interfacial processes cause the formation of reactive electrolyte degradation products which subsequently react with several different cell components, including the LMTO cathode, the electrolyte, and the anode. The downstream reactions of these reactive degradation products cause Mn/Ti dissolution from the LMTO cathode and the deposition of insulating, Li-containing, electrochemically-inactive species on the surfaces of both electrodes. Ultimately, the interfacial degradation leads to both a loss of active Li and a rise in cell impedance. The findings discussed herein demonstrate the necessity for stabilization of the DRX-electrolyte interface, either through moderation of voltage window, stabilization of the DRX surface, or the development of a more stable electrolyte. As shown, narrower voltage windows like 4.6 - 1.85 V and 4.6 - 2.0 V avoid much of the performance decay brought about by cycling to extreme voltages, but they also come with the cost of reduced initial energy density. Alternatively, material stabilization techniques (such as washing and coating) or the development of a more stable electrolyte would enable the use of a broader voltage window to achieve higher energy densities, further unlocking the potential of DRX materials.

This work also highlights the importance of tailoring the cell design to the experiment for which it is used. The cells used for DEMS and those used for long-term cycling are quite different from one another, in terms of the electrolyte quantity and the counter-electrode used, and each was selected because its characteristics complemented the goals of the experiment. For the DEMS experiments, an electrolyte-flooded half-cell is needed to allow for the evaluation of interfacial degradation at the LMTO-electrolyte interface without complications brought about by solvent evaporation or migrating counter-electrode potential. For the long-term cycling experiments, a customized electrolyte-lean full-cell was selected to properly expose the effects of interfacial degradation on performance decay during cycling. These design choices each provided clearer results for their respective experiments, allowing for a more comprehensive reconciliation of interfacial degradation and performance decay.

4.6 Supplementary Information

4.6.1 Cumulative Gas Evolution Quantities during Early Cycling

Table 4.1: Cumulative O_2 and CO_2 evolution quantities during first four cycles of LMTO cathodes in different voltage windows, as measured by DEMS. Cycling consisted of constant current charging and discharging at 0.1 Li hr^{-1} (32.9 mA g-LMTO^{-1}) to the listed upper and lower cut-off voltages, respectively. After each discharge, the cell was allowed to rest on open circuit for 2 hours. For all experiments, the electrolyte was 1M $LiPF_6$ in 3:7 EC:EMC. For reference, a typical pristine cathode contained approximately 80 μmol-LMTO.

Voltage Window	Cumulative Gas Evolved (mmol-gas mol-LMTO^{-1})			
	Cycle 1	Cycle 2	Cycle 3	Cycle 4
O_2				
4.6 - 1.5 V	~ 0	~ 0	~ 0	~ 0
4.6 - 1.85 V	~ 0	~ 0	~ 0	~ 0
4.6 - 2.0 V	~ 0	~ 0	~ 0	~ 0
4.8 - 1.5 V	0.71	~ 0	~ 0	~ 0
4.8 - 1.85 V	0.48	~ 0	~ 0	~ 0
4.8 - 2.0 V	0.66	~ 0	~ 0	~ 0
CO_2				
4.6 - 1.5 V	5.7	7.1	5.7	5.5
4.6 - 1.85 V	4.4	3.0	2.3	2.7
4.6 - 2.0 V	5.2	2.1	1.3	1.5
4.8 - 1.5 V	10.2	9.5	8.4	7.5
4.8 - 1.85 V	8.8	5.0	2.5	2.2
4.8 - 2.0 V	5.9	2.9	1.9	2.2

4.6.2 Graphite Formation and Pre-lithiation

Prior to full-cell cycling, pristine graphite electrodes (15 mm diameter disks) underwent formation cycling and pre-lithiation in graphite-Li coin cells. The formation cycling consisted of three full cycles in the voltage window of 1.5 - 0.01 V, with lithiation and delithiation occurring at constant rates of 0.56 mA and 1.12 mA, respectively. After formation cycling, the graphite electrodes were lithiated to a state of lithiation of 40% at a rate of 0.56 mA, with the state of lithiation estimated using the capacity of the final formation cycle. The voltage profiles for each graphite electrode during formation cycling and pre-lithiation are shown in Figures 4.9 and 4.10, respectively. For both figures, the labels on each plot corresponding to the voltage windows used for the full-cells in which the graphite electrodes were subsequently cycled.

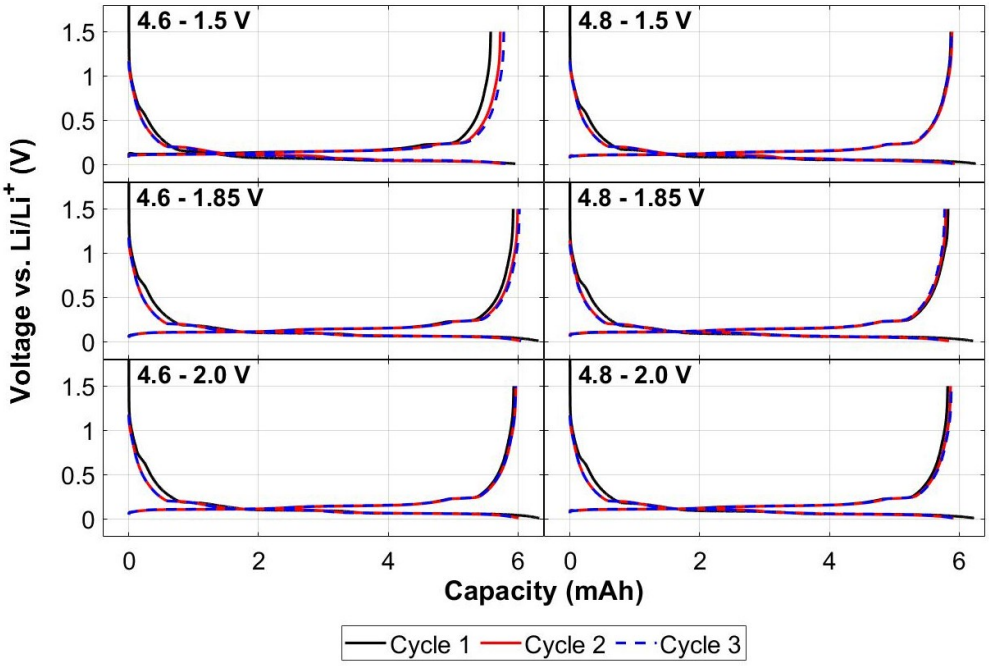

Figure 4.9: Formation cycling of pristine graphite electrodes in graphite-Li cells. Formation cycling consisted of three full cycles in the voltage window of 1.5 - 0.01 V, with lithiation and delithiation occurring at constant rates of 0.56 mA and 1.12 mA, respectively.

As shown in Figure 4.9, the graphite voltage profiles during formation cycling are nearly identical for all six electrodes, indicating reproducible electrode performance. Furthermore, a small irreversible capacity is observed on the first cycle, which is expected due to interfacial formation consisting primarily of electrolyte reduction occurring on the graphite surface. After the first cycle, the graphite cycling is quite reversible, indicating the formation of a

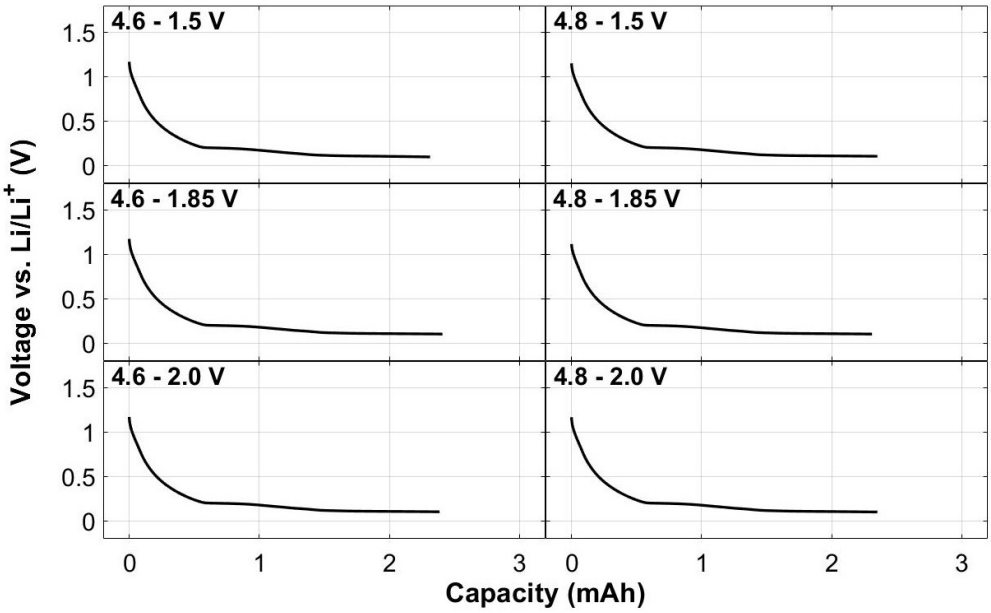

Figure 4.10: Pre-lithiation of graphite electrodes after formation cycling in graphite-Li cells. Graphite electrodes were lithiated to 40% state of lithiation, with the state of lithiation estimated based on the capacity of the final formation cycle.

passivating interfacial layer. The capacities observed for the final graphite formation cycles were approximately ∼5.9 mAh. The pre-lithiation of the graphite electrodes after formation cycling shows similar voltage profiles for all six electrodes (Figure 4.10), as expected based on the similar performance observed for the graphite electrodes during formation cycling. Based on the capacity of the final formation cycle (∼5.9 mAh), the capacity associated with the 40% pre-lithiation was ∼2.35 mAh.

4.6.3 EIS Measurements of Full-Cells in Discharged State

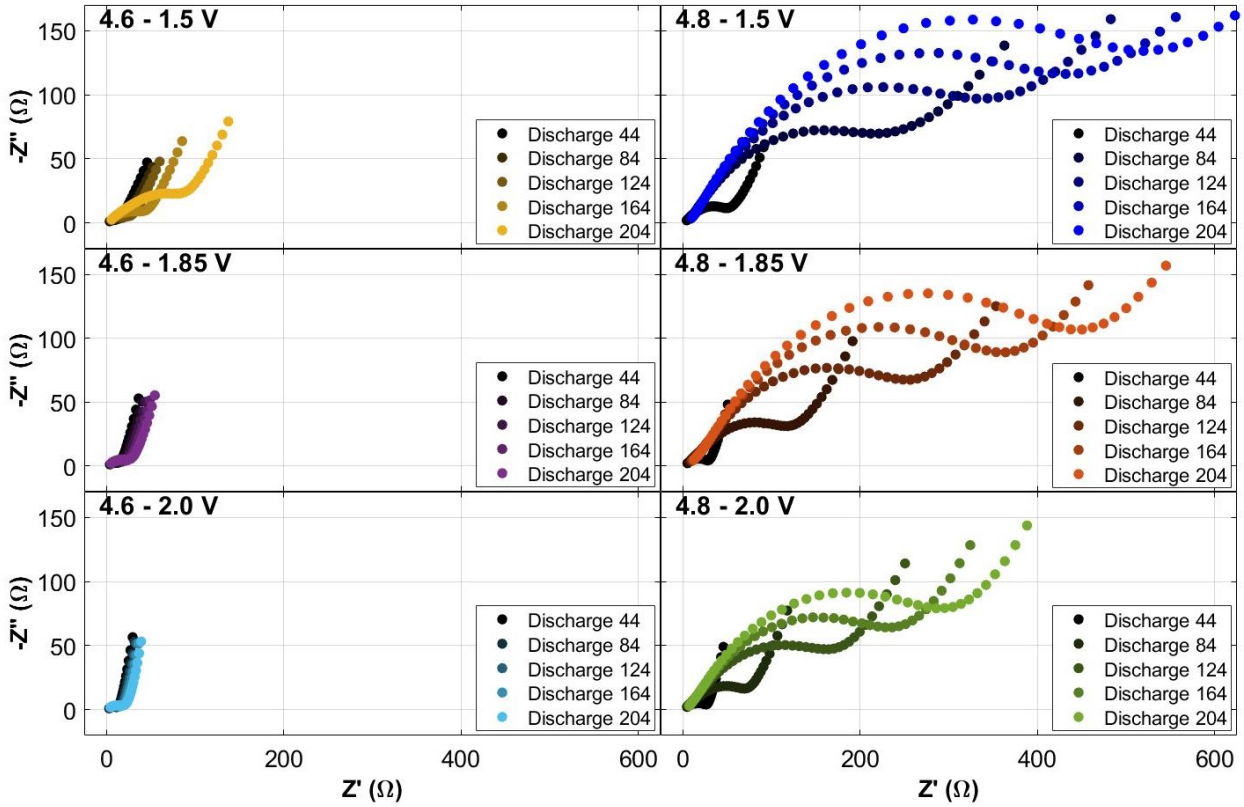

Figure 4.11: Nyquist plots obtained from EIS measurements of each cell on selected cycles, taken in the discharged state. EIS spectra were collected with a voltage amplitude of 5 mV in the frequency range of 20 kHz to 100 mHz. For each cycle, three scans were taken and averaged together to minimize error. The electrolyte used in all experiments was 1M $LiPF_6$ in 3:7 EC:EMC.

4.6.4 Voltage Profiles of Post-Mortem DEMS Cells

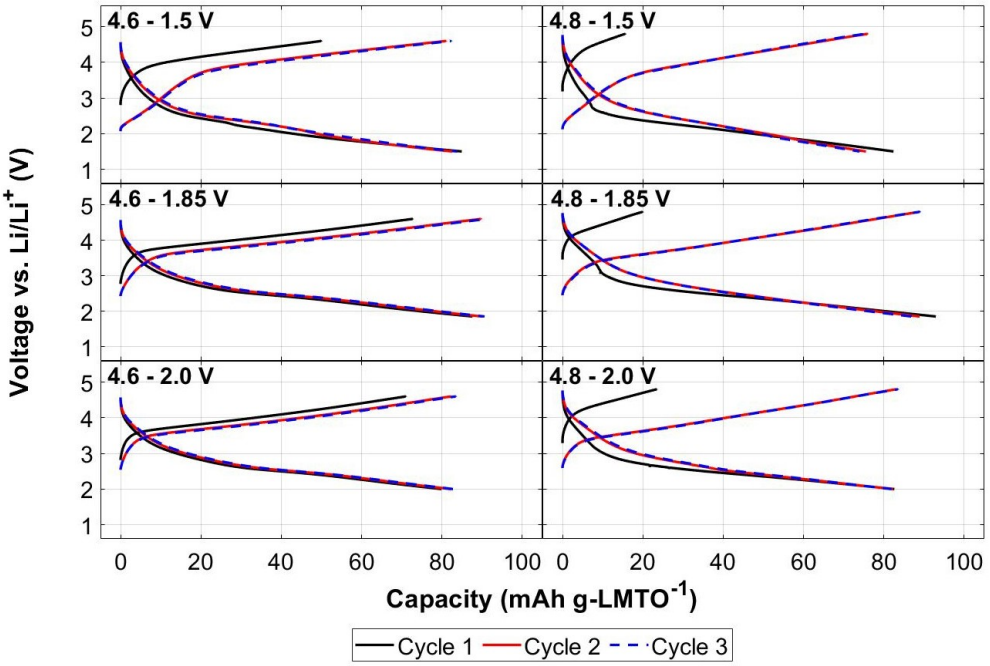

Figure 4.12: Voltage profiles from first three cycles of LMTO electrodes during post-mortem DEMS. Each LMTO electrode was charged in the same voltage windows that was used during full-cell cycling. Cycling was conducted at a constant current of 0.1 Li hr^{-1} (32.9 mA g-$LMTO^{-1}$), and the cells were allowed to rest for 5 hours after each discharge. The electrolyte was 1M $LiPF_6$ in 3:7 EC:EMC.

4.6.5 Titration Mass Spectrometry Analysis of Cycled Electrodes

After post-mortem cycling in graphite-Li half-cells, the graphite electrodes were analyzed using titration mass spectrometry (TiMS). During acid titration, any carbonate species deposited on the graphite surface will decompose to evolve CO_2, which can be detected and quantified using the TiMS apparatus. The reaction chemistry underlying CO_2 evolution during TiMS is shown in Equation 4.1. Additionally, any species that are highly reducing towards the acidic titration solution may react with the solution to evolve H_2. A generic redox reaction for the chemistry underlying H_2 evolution is given in Equation 4.2, where Red and Ox represent the reduced and oxidized forms of the reactive species, respectively.

$$CO^{2-}_{3\,(s)} + 2H^{+}_{(aq)} \rightarrow CO_{2\,(g)} + H_2O_{(l)} \tag{4.1}$$

$$Red + 2H^{+}_{(aq)} \rightarrow Ox + H_{2\,(g)} \tag{4.2}$$

To estimate the extent to which the initial graphite formation and pre-lithiation contributes to the CO_2 and H_2 evolution observed via TiMS, an additional two graphite electrodes were titrated after undergoing the same formation and pre-lithiation procedure as the graphite electrodes cycled in full-cells. After the formation and pre-lithiation procedure, the graphite electrodes were slowly delithiated, with the slow delithiation consisting of a constant current delithiation at a rate of 100 μA until the graphite potential reached a cut-off voltage of 1.5 V vs. Li/Li^+ followed by a potentiostatic hold at the cut-off voltage for 5 hours. The electrochemical performance observed from these two graphite electrodes during formation and pre-lithiation was very similar to that of the graphite electrodes that were subsequently used in full-cells, indicating that the graphite electrodes serve as suitable control samples. Furthermore, given that the electrodes underwent the same cycling procedure, the variation between the gas evolution quantities for the two control samples provides an estimate for the approximate error in the gas evolution measurement.

The cumulative CO_2 and H_2 evolution quantities measured during titration of the graphite electrodes are given in Table 4.2. Significant amounts of CO_2 and H_2 are evolved from the graphite electrodes cycled in full-cells. In contrast, much less CO_2 and very little H_2 is evolved from the graphite electrodes serving as control samples. The titration results for the control samples serve as an estimate for the amount of gas evolution that can be expected due to decomposition of the interfacial layer that forms during formation cycling, which likely consists of solid carbonates formed by electrolyte reduction. The additional gas evolution measured during titration of the graphite electrodes cycled in full-cells must therefore originate from decomposition of species deposited during long-term cycling.

The amounts of CO_2 evolved during titration of the graphite electrodes from the full-cells show a clear dependence on the voltage window used during cycling. Both increasing upper cut-off voltage and decreasing lower cut-off voltage lead to an increased amount of CO_2 evolved during titration, indicating a greater amount of carbonate on the graphite surface. The only exception to this trend is found in comparing the graphite electrodes

Table 4.2: Cumulative gas evolution quantities for CO_2 and H_2 during acid titration of delithiated graphite electrodes. The control electrodes only underwent the formation and pre-lithiation procedure, such that the differences between the control electrodes and the electrodes from the full-cells isolate the effects of long-term cycling in the different voltage windows. All graphite electrodes were titrated with 2 mL of N_2-sparged 3.5M H_2SO_4.

Sample	CO_2 Evolved (nmol)	H_2 Evolved (nmol)
4.8 - 1.5 V	13.4	12.7
4.8 - 1.85 V	11.3	10.1
4.8 - 2.0 V	11.3	11.1
4.6 - 1.5 V	12.7	3.6
4.6 - 1.85 V	10.6	5.0
4.6 - 2.0 V	9.5	5.8
Control 1	3.0	0.2
Control 2	2.6	0.4

from the 4.8 - 1.85 V and 4.8 - 2.0 V cells, which show the same amounts of carbonate. This finding suggests that the elevated interfacial degradation brought about by cycling to extreme voltages on either end of the voltage window leads to the increased deposition of lithium-containing carbonate species, consistent with all of the results observed throughout this report.

The manner in which electrolyte decomposition at the LMTO surface induces carbonate build-up at the graphite electrode also implies that some sort of crosstalk process occurs, as some reactive species formed at the LMTO surface must migrate over to the graphite surface to form the carbonate species. One possible explanation for this reactivity is that CO_2 formed at the LMTO surface diffuses through the electrolyte to the graphite surface, where it is reduced to form a carbonate-like deposit. Another potential explanation is that the elevated electrolyte degradation at the LMTO surface increases the concentration of water in the electrolyte through reaction of acidic electrolyte degradation products with cell components like the cathode, resulting in elevated rates of partial solvent hydrolysis which precipitates carbonates on the electrode surface.[42,43]

The amount of H_2 evolved during titration of the graphite electrodes extracted from the full-cells possesses a strong dependence on the upper cut-off voltage used during cycling, but it appears to lack any dependence on lower cut-off voltage. Titration of the graphite electrodes cycled in cells with an upper cut-off voltage of 4.8 V evolved roughly twice as much H_2 as titration of the graphite electrodes cycled in cells with an upper cut-off voltage of 4.6 V, indicating that some degradation process taking place during charging above 4.6 V leads to the formation of species within the graphite electrode that are reducing towards the aqueous titration solution.

The chemistry underlying H_2 evolution is unclear. One potential explanation is that LMTO-originating Mn/Ti species deposited on the graphite surface may reduce the aqueous titration solution. This hypothesis would explain the effect of the upper cut-off voltage

used during full-cell cycling on the amount of H_2 evolved during titration, as the amount of Mn/Ti deposition on the graphite surface increases with increasing upper cut-off voltage (as shown in Figure 4.8). However, this hypothesis does not explain the lack of dependence of H_2 evolution on the lower cut-off voltage used during cycling, as the amount of Mn/Ti deposition on the graphite surface also appears to increase with decreasing lower cut-off voltage. An alternative explanation is that lithiated graphite species become electrically isolated during cycling and cannot be oxidized during graphite delithiation, causing them to remain within the bulk of the electrode and react with the acidic solution during titration. The amount of lithiated graphite that would produce the observed H_2 evolution would account for less than 1 μAh of capacity for all six graphite electrodes, such that electrical isolation of lithiated graphite would not have a noticeable effect on the graphite capacity during post-mortem cycling. Consequently, the chemistry underlying H_2 evolution remains uncertain, motivating further investigation into the transformations that graphite electrodes undergo during cycling in full-cells with DRX cathodes.

Chapter 5

Conclusions

This dissertation examined the electrochemistry of lithium-excess, cation-disordered rock-salt (DRX) cathode materials, including both bulk redox processes and interfacial reactivity. The previous chapters presented investigations into the effects of DRX material composition and cycling conditions on electrochemical performance and interfacial degradation during initial and long-term cycling. These investigations relied heavily on the use of gas evolution measurement techniques, which revealed crucial information about bulk redox and interfacial degradation processes. In each study, these gas evolution measurements were paired with complementary characterization techniques to provide further insight into the complex processes occurring during electrochemical cycling of DRX cathode materials. Collectively, these investigations thoroughly deciphered the electrochemistry of DRX materials, demonstrating how the bulk redox and interfacial degradation processes determine the initial and long-term performance of DRX cathode materials.

The first study, presented in Chapter 2, investigated the effect of fluorine substitution on DRX material reactivity. The reactivities of two DRX materials, $Li_{1.2}Mn_{0.6}Nb_{0.2}O_2$ (LMNO) and $Li_{1.2}Mn_{0.625}Nb_{0.175}O_{1.95}F_{0.05}$ (LMNOF), were compared using differential electrochemical mass spectrometry (DEMS) and titration mass spectrometry (TiMS). Given that the only difference between LMNO and LMNOF is the incorporation of 2.5% fluorine and the accompanying shift in Mn/Nb composition, any differences in reactivity observed between the two materials were attributed to this difference in composition. It was shown that fluorination delays the onset and suppresses the extent of O_2 evolution during the first charge. Additionally, based on an accounting of the capacity during the first charge of each material, it was revealed that the fluorination and the accompanying change in Mn/Nb content increased the amount of $Mn^{3+/4+}$ redox and reduced the amount of oxygen redox. This change shifted the balance between $Mn^{3+/4+}$ redox and oxygen redox without strongly affecting the total charge capacity. Furthermore, CO_2 evolution arising due to electrolyte degradation was observed to a diminishing extent over the first four cycles for both materials. Lastly, lattice fluorine dissolution was shown to occur from the LMNOF surface during charging, with the extent of dissolution gradually attenuating over the first four cycles. These results highlighted the multiple ways in which DRX composition affects material reactivity, motivating

a more thorough exploration of the DRX compositional space to enable rational design of improved DRX materials.

In Chapter 3, the reactivities of three different highly-fluorinated Mn/Nb-based DRX materials with widely varying compositions were assessed using DEMS, TiMS, and a suite of complementary spectroscopy techniques. The three materials were $Li_{1.2}Mn_{0.45}Nb_{0.35}O_{1.85}F_{0.15}$ (LMNOF-4515, 7.5% F), $Li_{1.2}Mn_{0.60}Nb_{0.20}O_{1.40}F_{0.60}$ (LMNOF-6060, 30% F), and $Li_{1.2}Mn_{0.625}Nb_{0.175}O_{1.325}F_{0.675}$ (LMNOF-6368, 33.75% F). In order to achieve these extremely high levels of fluorination, high-energy mechanochemical synthesis was required. Owing to their high levels of fluorination, these materials are able to achieve the highly desirable 2-electron $Mn^{2+/4+}$ redox couple. It was shown that the degree of fluorination and accompanying shift in Mn/Nb content drastically tunes the balance between $Mn^{2+/4+}$ and oxygen redox, with LMNOF-4515 undergoing a significant amount of oxygen redox and LMNOF-6368 relying exclusively on $Mn^{2+/4+}$ redox. In addition to this bulk redox analysis, unusual modes of electrolyte degradation were observed for all three materials, resulting in multiple peaks of CO_2 evolution within a single cycle and the high-voltage formation of acidic species. Lastly, lattice fluorine dissolution was shown to occur from the LMNOF surface during charging for all three materials, with the extent of fluorine dissolution increasing with increasing fluorination. This study demonstrated that the redox processes in DRX materials can be tuned using fluorination to promote desirable redox couples such as $Mn^{2+/4+}$, but it also revealed that high levels of fluorination and the mechanochemical synthesis necessary to access them leads to elevated interfacial reactivity that is likely to compromise long-term cycling performance.

The final study, presented in Chapter 4, examined how the voltage window used during cycling affects the interfacial reactivity and long-term cycling performance of $Li_{1.2}Mn0.4Ti_{0.4}O_2$ (LMTO). DEMS was used to examine the interfacial degradation that occurs during initial cycling of LMTO in a set of voltage windows (4.6/4.8 - 1.5/1.85/2.0 V vs. Li/Li^+), and extended cycling experiments using customized full-cells were used to examine the long-term cycling performance of LMTO in the same set of voltage windows. It was revealed that charging above 4.6 V and discharging below 2.0 V each lead to elevated electrolyte degradation, driving performance decay through a loss of active Li and a rise in cell impedance. In contrast, less electrolyte degradation and more stable cell performance was observed from the cell charged to 4.6 V and discharged to 2.0 V. After each long-term cycling experiment, a post-mortem analysis of each full-cell revealed that the elevated electrolyte degradation brought about cycling to the extreme ends of the voltage window leads to the deposition of insulating, Li-containing degradation products, consistent with the observed loss of active Li and rise in cell impedance. The post-mortem analysis also demonstrated that extensive Mn/Ti dissolution occurs from the LMTO cathodes during extended cycling, with the amount of Mn/Ti dissolution increasing with increasing upper cut-off voltage and decreasing lower cut-off voltage. The findings of this study highlighted the trade-off between initial and long-term cycling performance, as cycling to extreme ends of the voltage window boosts initial capacity at the expense of long-term cycling stability. Furthermore, this study established a clear connection between interfacial degradation and cycling stability, motivating

the development of methods of interfacial stabilization to improve long-term cycling performance.

Collectively, these results highlight the strengths and weaknesses of DRX materials. The promise lies in the bulk redox processes, which can provide high energy densities using low-cost, resource-friendly transition metals. The challenge lies in the interfacial reactivity, as the broad voltage windows required to achieve high capacities drive extensive electrolyte degradation which compromises long-term cycling stability. In order to unlock the potential of DRX materials, the DRX-electrolyte interface must be stabilized. Alongside voltage window moderation, promising potential routes towards stabilization include the development of an electrolyte with improved stability or the modification of the DRX surface by methods such as washing or coating.

Bibliography

[1] Matthew Li et al. "30 Years of Lithium-Ion Batteries". In: *Advanced Materials* 30.33 (Aug. 2018). Publisher: John Wiley & Sons, Ltd, p. 1800561. ISSN: 0935-9648. DOI: 10.1002/adma.201800561. URL: https://doi.org/10.1002/adma.201800561 (visited on 06/08/2023).

[2] Bryan D McCloskey. "Expanding the Ragone Plot: Pushing the Limits of Energy Storage". In: *The Journal of Physical Chemistry Letters* 6.18 (Sept. 2015). Publisher: American Chemical Society, pp. 3592–3593. DOI: 10.1021/acs.jpclett.5b01813. URL: https://doi.org/10.1021/acs.jpclett.5b01813.

[3] John B. Goodenough and Kyu Sung Park. "The Li-ion rechargeable battery: A perspective". In: *Journal of the American Chemical Society* 135.4 (2013), pp. 1167–1176. ISSN: 00027863. DOI: 10.1021/ja3091438.

[4] Naoki Nitta et al. "Li-ion battery materials: Present and future". In: *Materials Today* 18.5 (2015). Publisher: Elsevier Ltd., pp. 252–264. ISSN: 18734103. DOI: 10.1016/j.mattod.2014.10.040. URL: http://www.sciencedirect.com/science/article/pii/S1369702114004118.

[5] Thomas Marks et al. "A Guide to Li-Ion Coin-Cell Electrode Making for Academic Researchers". In: *Journal of The Electrochemical Society* 158.1 (2011). Publisher: The Electrochemical Society, A51. ISSN: 0013-4651. DOI: 10.1149/1.3515072. URL: http://dx.doi.org/10.1149/1.3515072.

[6] M. Stanley Whittingham. "Lithium batteries and cathode materials". In: *Chemical Reviews* 104.10 (2004), pp. 4271–4301. ISSN: 00092665. DOI: 10.1021/cr020731c.

[7] Calvin D. Quilty et al. "Electron and Ion Transport in Lithium and Lithium-Ion Battery Negative and Positive Composite Electrodes". In: *Chemical Reviews* 123.4 (Feb. 2023). Publisher: American Chemical Society, pp. 1327–1363. ISSN: 0009-2665. DOI: 10.1021/acs.chemrev.2c00214. URL: https://doi.org/10.1021/acs.chemrev.2c00214.

[8] Hao Chen et al. "Exploring Chemical, Mechanical, and Electrical Functionalities of Binders for Advanced Energy-Storage Devices". In: *Chemical Reviews* 118.18 (Sept. 2018). Publisher: American Chemical Society, pp. 8936–8982. ISSN: 0009-2665. DOI:

10.1021/acs.chemrev.8b00241. URL: https://doi.org/10.1021/acs.chemrev.8b00241.

[9] Pengcheng Zhu et al. "A review of current collectors for lithium-ion batteries". In: *Journal of Power Sources* 485 (Feb. 2021), p. 229321. ISSN: 0378-7753. DOI: 10.1016/j.jpowsour.2020.229321. URL: https://www.sciencedirect.com/science/article/pii/S0378775320316098.

[10] Jakob Asenbauer et al. "The success story of graphite as a lithium-ion anode material – fundamentals, remaining challenges, and recent developments including silicon (oxide) composites". In: *Sustainable Energy & Fuels* 4.11 (2020). Publisher: The Royal Society of Chemistry, pp. 5387–5416. DOI: 10.1039/D0SE00175A. URL: http://dx.doi.org/10.1039/D0SE00175A.

[11] John B. Goodenough and Youngsik Kim. "Challenges for rechargeable Li batteries". In: *Chemistry of Materials* 22.3 (2010), pp. 587–603. ISSN: 08974756. DOI: 10.1021/cm901452z.

[12] Kang Xu. "Nonaqueous liquid electrolytes for lithium-based rechargeable batteries". In: *Chemical Reviews* 104.10 (Oct. 2004). Publisher: American Chemical Society, pp. 4303–4417. ISSN: 00092665. DOI: 10.1021/cr030203g. URL: https://doi.org/10.1021/cr030203g.

[13] Zachary P. Cano et al. "Batteries and fuel cells for emerging electric vehicle markets". In: *Nature Energy* 3.4 (Apr. 2018), pp. 279–289. ISSN: 2058-7546. DOI: 10.1038/s41560-018-0108-1. URL: https://doi.org/10.1038/s41560-018-0108-1.

[14] P Wolfram and N Lutsey. "Electric vehicles: Literature review of technology costs and carbon emissions. International Council on Clean Transportation". In: (2016). Publisher: Working Paper 2019-14. 2016. Available online: www. theicct. org (accessed ...

[15] Kostiantyn Turcheniuk et al. "Ten years left to redesign lithium-ion batteries". In: *Nature* 559.7715 (2018), pp. 467–470. ISSN: 14764687. DOI: 10.1038/d41586-018-05752-3.

[16] Maxwell D. Radin et al. "Narrowing the Gap between Theoretical and Practical Capacities in Li-Ion Layered Oxide Cathode Materials". In: *Advanced Energy Materials* 7.20 (2017), p. 1602888. ISSN: 16146840. DOI: 10.1002/aenm.201602888.

[17] Eric J Wu, Patrick D Tepesch, and Gerbrand Ceder. "Size and charge effects on the structural stability of LiMO2 (M = transition metal) compounds". In: *Philosophical Magazine B* 77.4 (Apr. 1998). Publisher: Taylor & Francis, pp. 1039–1047. ISSN: 1364-2812. DOI: 10.1080/13642819808206403. URL: https://doi.org/10.1080/13642819808206403.

[18] John Reed and Gerbrand Ceder. "Role of Electronic Structure in the Susceptibility of Metastable Transition-Metal Oxide Structures to Transformation". In: *Chemical Reviews* 104.10 (Oct. 2004). Publisher: American Chemical Society, pp. 4513–4534. ISSN: 0009-2665. DOI: 10.1021/cr020733x. URL: https://doi.org/10.1021/cr020733x.

[19] Benjamin K. Sovacool. "When subterranean slavery supports sustainability transitions? power, patriarchy, and child labor in artisanal Congolese cobalt mining". In: *The Extractive Industries and Society* 8.1 (Mar. 2021), pp. 271–293. ISSN: 2214-790X. DOI: 10.1016/j.exis.2020.11.018. URL: https://www.sciencedirect.com/science/article/pii/S2214790X20303154.

[20] Marc Wentker, Matthew Greenwood, and Jens Leker. "A Bottom-Up Approach to Lithium-Ion Battery Cost Modeling with a Focus on Cathode Active Materials". In: *Energies* 12.3 (2019). ISSN: 1996-1073. DOI: 10.3390/en12030504.

[21] Evan M. Erickson et al. "Review—Recent Advances and Remaining Challenges for Lithium Ion Battery Cathodes". In: *Journal of The Electrochemical Society* 164.1 (Jan. 2017). Publisher: The Electrochemical Society, A6341. ISSN: 1945-7111. DOI: 10.1149/2.0461701jes. URL: https://dx.doi.org/10.1149/2.0461701jes.

[22] Wenhua Zuo et al. "Li-rich cathodes for rechargeable Li-based batteries: reaction mechanisms and advanced characterization techniques". In: *Energy & Environmental Science* 13.12 (2020). Publisher: The Royal Society of Chemistry, pp. 4450–4497. ISSN: 1754-5692. DOI: 10.1039/D0EE01694B. URL: http://dx.doi.org/10.1039/D0EE01694B.

[23] Dong Hwa Seo et al. "The structural and chemical origin of the oxygen redox activity in layered and cation-disordered Li-excess cathode materials". In: *Nature Chemistry* 8.7 (2016). Publisher: Nature Publishing Group, pp. 692–697. ISSN: 17554349. DOI: 10.1038/nchem.2524.

[24] Gaurav Assat et al. "Decoupling Cationic–Anionic Redox Processes in a Model Li-Rich Cathode via Operando X-ray Absorption Spectroscopy". In: *Chemistry of Materials* 29.22 (Nov. 2017). Publisher: American Chemical Society, pp. 9714–9724. ISSN: 0897-4756. DOI: 10.1021/acs.chemmater.7b03434. URL: https://doi.org/10.1021/acs.chemmater.7b03434.

[25] Srinivasan Ramakrishnan et al. "Extended Interfacial Stability through Simple Acid Rinsing in a Li-Rich Oxide Cathode Material". In: *Journal of the American Chemical Society* 142.18 (Apr. 2020), pp. 8522–8531. ISSN: 15205126. DOI: 10.1021/jacs.0c02859.

[26] Joshua J. Zak et al. "Irreversible Anion Oxidation Leads to Dynamic Charge Compensation in the Ru-Poor, Li-Rich Cathode Li2Ru0.3Mn0.7O3". In: *ACS Energy Letters* (Dec. 2022). Publisher: American Chemical Society, pp. 722–730. DOI: 10.1021/acsenergylett.2c02537. URL: https://doi.org/10.1021/acsenergylett.2c02537.

[27] Sara E Renfrew and Bryan D McCloskey. "Residual Lithium Carbonate Predominantly Accounts for First Cycle CO2 and CO Outgassing of Li-Stoichiometric and Li-Rich Layered Transition-Metal Oxides". In: *Journal of the American Chemical Society* 139.49 (Dec. 2017). Publisher: American Chemical Society, pp. 17853–17860. ISSN: 0002-7863. DOI: 10.1021/jacs.7b08461. URL: https://doi.org/10.1021/jacs.7b08461.

[28] Yongwoo Shin et al. "Alleviating oxygen evolution from Li-excess oxide materials through theory-guided surface protection". In: *Nature Communications* 9.1 (2018), p. 4597. ISSN: 2041-1723. DOI: 10.1038/s41467-018-07080-6. URL: https://doi.org/10.1038/s41467-018-07080-6.

[29] Cécile Genevois et al. "Insight into the Atomic Structure of Cycled Lithium-Rich Layered Oxide Li1.20Mn0.54Co0.13Ni0.13O2 Using HAADF STEM and Electron Nanodiffraction". In: *The Journal of Physical Chemistry C* 119.1 (Jan. 2015). Publisher: American Chemical Society, pp. 75–83. ISSN: 1932-7447. DOI: 10.1021/jp509388j. URL: https://doi.org/10.1021/jp509388j.

[30] Hideyuki Koga et al. "Different oxygen redox participation for bulk and surface: A possible global explanation for the cycling mechanism of Li1.20Mn0.54Co0.13Ni0.13O2". In: *Journal of Power Sources* 236 (Aug. 2013), pp. 250–258. ISSN: 0378-7753. DOI: 10.1016/j.jpowsour.2013.02.075. URL: https://www.sciencedirect.com/science/article/pii/S0378775313003601.

[31] Hideyuki Koga et al. "Reversible Oxygen Participation to the Redox Processes Revealed for Li1.20Mn0.54Co0.13Ni0.13O2". In: *Journal of The Electrochemical Society* 160.6 (Mar. 2013). Publisher: The Electrochemical Society, A786. ISSN: 1945-7111. DOI: 10.1149/2.038306jes. URL: https://dx.doi.org/10.1149/2.038306jes.

[32] Yuan Yue et al. "Redox Behaviors in a Li-Excess Cation-Disordered Mn–Nb–O–F Rocksalt Cathode". In: *Chemistry of Materials* 32.11 (2020), pp. 4490–4498. ISSN: 0897-4756. DOI: 10.1021/acs.chemmater.9b05221.

[33] Kun Luo et al. "Charge-compensation in 3d-transition-metal-oxide intercalation cathodes through the generation of localized electron holes on oxygen". In: *Nature Chemistry* 8.7 (2016). Publisher: Nature Publishing Group ISBN: 1755-4349, pp. 684–691. ISSN: 17554349. DOI: 10.1038/nchem.2471. URL: http://dx.doi.org/10.1038/nchem.2471.

[34] Zhengyan Lun et al. "Improved Cycling Performance of Li-Excess Cation-Disordered Cathode Materials upon Fluorine Substitution". In: *Advanced Energy Materials* 9.2 (Jan. 2019). Publisher: John Wiley & Sons, Ltd, p. 1802959. ISSN: 16146840. DOI: 10.1002/aenm.201802959. URL: https://doi.org/10.1002/aenm.201802959.

[35] Matthew J. Crafton et al. "Tuning Bulk Redox and Altering Interfacial Reactivity in Highly Fluorinated Cation-Disordered Rocksalt Cathodes". In: *ACS Applied Materials & Interfaces* 15.15 (Apr. 2023). Publisher: American Chemical Society, pp. 18747–18762. ISSN: 1944-8244. DOI: 10.1021/acsami.2c16974. URL: https://doi.org/10.1021/acsami.2c16974.

[36] Michael Metzger et al. "Origin of H2Evolution in LIBs: H2O Reduction vs. Electrolyte Oxidation". In: *Journal of The Electrochemical Society* 163.5 (2016). Publisher: The Electrochemical Society, A798–A809. ISSN: 0013-4651. DOI: 10.1149/2.1151605jes. URL: http://dx.doi.org/10.1149/2.1151605jes.

[37] Matthew J. Crafton et al. "Anion Reactivity in Cation-Disordered Rocksalt Cathode Materials: The Influence of Fluorine Substitution". In: *Advanced Energy Materials* 10.35 (2020), pp. 1–12. ISSN: 16146840. DOI: 10.1002/aenm.202001500.

[38] Magali Gauthier et al. "Electrode–Electrolyte Interface in Li-Ion Batteries: Current Understanding and New Insights". In: *The Journal of Physical Chemistry Letters* 6.22 (Nov. 2015). Publisher: American Chemical Society, pp. 4653–4672. DOI: 10.1021/acs.jpclett.5b01727. URL: https://doi.org/10.1021/acs.jpclett.5b01727.

[39] Wesley M. Dose et al. "Effect of Anode Slippage on Cathode Cutoff Potential and Degradation Mechanisms in Ni-Rich Li-Ion Batteries". In: *Cell Reports Physical Science* 1.11 (Nov. 2020), p. 100253. ISSN: 2666-3864. DOI: 10.1016/j.xcrp.2020.100253. URL: https://www.sciencedirect.com/science/article/pii/S2666386420302757.

[40] Jing Li et al. "The Impact of Electrolyte Additives and Upper Cut-off Voltage on the Formation of a Rocksalt Surface Layer in LiNi0.8Mn0.1Co0.1O2 Electrodes". In: *Journal of The Electrochemical Society* 164.4 (Feb. 2017). Publisher: The Electrochemical Society, A655. ISSN: 1945-7111. DOI: 10.1149/2.0651704jes. URL: https://dx.doi.org/10.1149/2.0651704jes.

[41] Irmgard Buchberger et al. "Aging Analysis of Graphite/LiNi1/3Mn1/3Co1/3O2 Cells Using XRD, PGAA, and AC Impedance". In: *Journal of The Electrochemical Society* 162.14 (Oct. 2015). Publisher: The Electrochemical Society, A2737. ISSN: 1945-7111. DOI: 10.1149/2.0721514jes. URL: https://dx.doi.org/10.1149/2.0721514jes.

[42] Bernardine L D Rinkel et al. "Two electrolyte decomposition pathways at nickel-rich cathode surfaces in lithium-ion batteries". In: *Energy & Environmental Science* (2022). Publisher: The Royal Society of Chemistry. ISSN: 1754-5692. DOI: 10.1039/D1EE04053G. URL: http://dx.doi.org/10.1039/D1EE04053G.

[43] Bernardine L D Rinkel et al. "Electrolyte Oxidation Pathways in Lithium-Ion Batteries". In: *Journal of the American Chemical Society* 142.35 (Sept. 2020). Publisher: American Chemical Society, pp. 15058–15074. ISSN: 0002-7863. DOI: 10.1021/jacs.0c06363. URL: https://doi.org/10.1021/jacs.0c06363.

[44] R J Clément, Z Lun, and G Ceder. "Cation-disordered rocksalt transition metal oxides and oxyfluorides for high energy lithium-ion cathodes". In: *Energy & Environmental Science* 13.2 (2020). Publisher: The Royal Society of Chemistry, pp. 345–373. ISSN: 1754-5692. DOI: drd. URL: http://dx.doi.org/10.1039/C9EE02803J.

[45] Arumugam Manthiram. "A reflection on lithium-ion battery cathode chemistry". In: *Nature Communications* 11.1 (Mar. 2020), p. 1550. ISSN: 2041-1723. DOI: 10.1038/s41467-020-15355-0. URL: https://doi.org/10.1038/s41467-020-15355-0.

[46] Arumugam Manthiram. "An Outlook on Lithium Ion Battery Technology". In: *ACS Central Science* 3.10 (2017), pp. 1063–1069. ISSN: 23747951. DOI: 10.1021/acscentsci.7b00288.

[47] Dongchang Chen, Juhyeon Ahn, and Guoying Chen. "An Overview of Cation-Disordered Lithium-Excess Rocksalt Cathodes". In: *ACS Energy Letters* (Mar. 2021). Publisher: American Chemical Society, pp. 1358–1376. DOI: 10.1021/acsenergylett.1c00203. URL: https://doi.org/10.1021/acsenergylett.1c00203.

[48] Zhengyan Lun et al. "Cation-disordered rocksalt-type high-entropy cathodes for Li-ion batteries". In: *Nature Materials* (2020). ISSN: 1476-4660. DOI: 10.1038/s41563-020-00816-0. URL: https://doi.org/10.1038/s41563-020-00816-0.

[49] Tzu Yang Huang et al. "Deconvolution of intermixed redox processes in Ni-based cation-disordered Li-excess cathodes". In: *Energy and Environmental Science* 14.3 (2021). Publisher: The Royal Society of Chemistry, pp. 1553–1562. ISSN: 17545706. DOI: 10.1039/d0ee03526b. URL: http://dx.doi.org/10.1039/D0EE03526B.

[50] Jinhyuk Lee et al. "A new class of high capacity cation-disordered oxides for rechargeable lithium batteries: Li-Ni-Ti-Mo oxides". In: *Energy and Environmental Science* 8.11 (2015). ISBN: 1754-5692\r1754-5706, pp. 3255–3265. ISSN: 17545706. DOI: 10.1039/c5ee02329g.

[51] Jianping Huang et al. "Non-topotactic reactions enable high rate capability in Li-rich cathode materials". In: *Nature Energy* 6.7 (2021), pp. 706–714. ISSN: 2058-7546. DOI: 10.1038/s41560-021-00817-6. URL: https://doi.org/10.1038/s41560-021-00817-6.

[52] Yuan Yue et al. "Tailoring the Redox Reactions for High-Capacity Cycling of Cation-Disordered Rocksalt Cathodes". In: *Advanced Functional Materials* 31.14 (Jan. 2021). Publisher: John Wiley & Sons, Ltd, p. 2008696. ISSN: 16163028. DOI: 10.1002/adfm.202008696. URL: https://doi.org/10.1002/adfm.202008696.

[53] Yuan Yue et al. "High-Voltage Reactivity and Long-Term Stability of Cation-Disordered Rocksalt Cathodes". In: *Chemistry of Materials* (Feb. 2022). Publisher: American Chemical Society. ISSN: 0897-4756. DOI: 10.1021/acs.chemmater.1c03115. URL: https://doi.org/10.1021/acs.chemmater.1c03115.

[54] Rohit Satish et al. "Exposure History and its Effect Towards Stabilizing Li Exchange Across Disordered Rock Salt Interfaces". In: *ChemElectroChem* 8.20 (Sept. 2021). Publisher: John Wiley & Sons, Ltd, pp. 3982–3991. ISSN: 2196-0216. DOI: 10.1002/celc.202100891. URL: https://doi.org/10.1002/celc.202100891.

[55] Tzu-Yang Huang et al. "Quantitative Decoupling of Oxygen-Redox and Manganese-Redox Voltage Hysteresis in a Cation-Disordered Rock Salt Cathode". In: *Advanced Energy Materials* n/a.n/a (Apr. 2023). Publisher: John Wiley & Sons, Ltd, p. 2300241. ISSN: 1614-6832. DOI: 10.1002/aenm.202300241. URL: https://doi.org/10.1002/aenm.202300241 (visited on 05/18/2023).

[56] Yuan Yue et al. "Interplay between Cation and Anion Redox in Ni-Based Disordered Rocksalt Cathodes". In: *ACS Nano* (Aug. 2021). Publisher: American Chemical Society. ISSN: 1936-0851. DOI: 10.1021/acsnano.1c03289. URL: https://doi.org/10.1021/acsnano.1c03289.

[57] Elsa A Olivetti et al. "Lithium-Ion Battery Supply Chain Considerations: Analysis of Potential Bottlenecks in Critical Metals". In: *Joule* 1.2 (2017), pp. 229–243. ISSN: 2542-4351. DOI: https://doi.org/10.1016/j.joule.2017.08.019. URL: http://www.sciencedirect.com/science/article/pii/S2542435117300442.

[58] Prasant Kumar Nayak et al. "Review on Challenges and Recent Advances in the Electrochemical Performance of High Capacity Li- and Mn-Rich Cathode Materials for Li-Ion Batteries". In: *Advanced Energy Materials* 8.8 (2018), pp. 1–16. ISSN: 16146840. DOI: 10.1002/aenm.201702397.

[59] Alexander Kraytsberg et al. "Higher, stronger, better ... A review of 5 volt cathode materials for advanced lithium-ion batteries". In: *Advanced Energy Materials* 2.8 (2012), pp. 922–939. ISSN: 16146832. DOI: 10.1002/aenm.201200068.

[60] Yang Kook Sun et al. "High-energy cathode material for long-life and safe lithium batteries". In: *Nature Materials* 8.4 (2009). Publisher: Nature Publishing Group, pp. 320–324. ISSN: 14764660. DOI: 10.1038/nmat2418.

[61] Jinhyuk Lee et al. "Reversible Mn2+/Mn4+ double redox in lithium-excess cathode materials". In: *Nature* 556.7700 (2018), pp. 185–190. ISSN: 1476-4687. DOI: 10.1038/s41586-018-0015-4. URL: https://doi.org/10.1038/s41586-018-0015-4.

[62] Robert A. House et al. "Lithium manganese oxyfluoride as a new cathode material exhibiting oxygen redox". In: *Energy and Environmental Science* 11.4 (2018). Publisher: Royal Society of Chemistry, pp. 926–932. ISSN: 17545706. DOI: 10.1039/c7ee03195e.

[63] Wang Hay Kan et al. "Unravelling Solid-State Redox Chemistry in Li1.3Nb0.3Mn0.4O2 Single-Crystal Cathode Material". In: *Chemistry of Materials* 30.5 (2018), pp. 1655–1666. ISSN: 15205002. DOI: 10.1021/acs.chemmater.7b05036.

[64] Jinhyuk Lee et al. "Unlocking the potential of cation-disordered oxides for rechargeable lithium batteries". In: *Science* 343.6170 (Jan. 2014), pp. 519–522. ISSN: 10959203. DOI: 10.1126/science.1246432. URL: http://science.sciencemag.org/content/343/6170/519.abstract.

[65] Jinhyuk Lee et al. "Mitigating oxygen loss to improve the cycling performance of high capacity cation-disordered cathode materials". In: *Nature Communications* 8.1 (2017), p. 981. ISSN: 20411723. DOI: 10.1038/s41467-017-01115-0. URL: https://doi.org/10.1038/s41467-017-01115-0.

[66] Daniil A Kitchaev et al. "Design principles for high transition metal capacity in disordered rocksalt Li-ion cathodes". In: *Energy & Environmental Science* 11.8 (2018). Publisher: The Royal Society of Chemistry, pp. 2159–2171. ISSN: 1754-5692. DOI: 10.1039/C8EE00816G. URL: http://dx.doi.org/10.1039/C8EE00816G.

[67] Claude Delmas. "Battery materials: Operating through oxygen". In: *Nature Chemistry* 8.7 (2016). Publisher: Nature Publishing Group, pp. 641–643. ISSN: 17554349. DOI: 10.1038/nchem.2558. URL: http://dx.doi.org/10.1038/nchem.2558.

[68] Jihyun Hong et al. "Metal–oxygen decoordination stabilizes anion redox in Li-rich oxides". In: *Nature Materials* 18.3 (2019). Publisher: Springer US ISBN: 4156301802761, pp. 256–265. ISSN: 14764660. DOI: 10.1038/s41563-018-0276-1. URL: https://doi.org/10.1038/s41563-018-0276-1.

[69] William E. Gent et al. "Coupling between oxygen redox and cation migration explains unusual electrochemistry in lithium-rich layered oxides". In: *Nature Communications* 8.1 (2017). Publisher: Springer US ISBN: 2041-1723, p. 2091. ISSN: 20411723. DOI: 10.1038/s41467-017-02041-x. URL: https://doi.org/10.1038/s41467-017-02041-x.

[70] Gaurav Assat et al. "Fundamental interplay between anionic/cationic redox governing the kinetics and thermodynamics of lithium-rich cathodes". In: *Nature Communications* 8.1 (2017). Publisher: Springer US ISBN: 2041-1723. ISSN: 20411723. DOI: 10.1038/s41467-017-02291-9. URL: http://dx.doi.org/10.1038/s41467-017-02291-9.

[71] M Sathiya et al. "Reversible anionic redox chemistry in high-capacity layered-oxide electrodes". In: *Nature Materials* 12.9 (2013), pp. 827–835. ISSN: 1476-4660. DOI: 10.1038/nmat3699. URL: https://doi.org/10.1038/nmat3699.

[72] A. Grimaud et al. "Anionic redox processes for electrochemical devices". In: *Nature Materials* 15.2 (2016), pp. 121–126. ISSN: 14764660. DOI: 10.1038/nmat4551. URL: https://doi.org/10.1038/nmat4551.

[73] Jing Xu et al. "Elucidating anionic oxygen activity in lithium-rich layered oxides". In: *Nature Communications* 9.1 (2018), p. 947. ISSN: 2041-1723. DOI: 10.1038/s41467-018-03403-9. URL: https://doi.org/10.1038/s41467-018-03403-9.

[74] Alexis Grimaud et al. "Activating lattice oxygen redox reactions in metal oxides to catalyse oxygen evolution". In: *Nature Chemistry* 9.5 (2017), pp. 457–465. ISSN: 1755-4349. DOI: 10.1038/nchem.2695. URL: https://doi.org/10.1038/nchem.2695.

[75] Christoph Bolli et al. "Operando Monitoring of F– Formation in Lithium Ion Batteries". In: *Chemistry of Materials* 31.4 (Jan. 2019), pp. 1258–1267. DOI: 10.1021/acs.chemmater.8b03810.

[76] Aurélie Guéguen et al. "Elucidating the Reactivity of Tris(trimethylsilyl)phosphite and Tris(trimethylsilyl)phosphate Additives in Carbonate Electrolytes - A Comparative Online Electrochemical Mass Spectrometry Study". In: *ACS Applied Energy Materials* 3.1 (2020), pp. 290–299. ISSN: 25740962. DOI: 10.1021/acsaem.9b01551.

[77] Grégory Gachot et al. "Gas chromatography/mass spectrometry as a suitable tool for the li-ion battery electrolyte degradation mechanisms study". In: *Analytical Chemistry* 83.2 (2011), pp. 478–485. ISSN: 00032700. DOI: 10.1021/ac101948u.

[78] Sophie Solchenbach et al. "Quantification of PF 5 and POF 3 from Side Reactions of LiPF 6 in Li-Ion Batteries". In: *Journal of The Electrochemical Society* 165.13 (2018), A3022–A3028. ISSN: 0013-4651. DOI: 10.1149/2.0481813jes.

[79] Andriy V Plakhotnyk, Ludger Ernst, and Reinhard Schmutzler. "Hydrolysis in the system LiPF6—propylene carbonate—dimethyl carbonate—H2O". In: *Journal of Fluorine Chemistry* 126.1 (2005), pp. 27–31. ISSN: 0022-1139. DOI: https://doi.org/10.1016/j.jfluchem.2004.09.027. URL: https://www.sciencedirect.com/science/article/pii/S0022113904002714.

[80] Bryan D. Mccloskey et al. "Combining accurate O2 and Li2O2 assays to separate discharge and charge stability limitations in nonaqueous Li-O 2 Batteries". In: *Journal of Physical Chemistry Letters* 4.17 (Aug. 2013), pp. 2989–2993. ISSN: 19487185. DOI: 10.1021/jz401659f.

[81] B. D. McCloskey et al. "Solvents' Critical Role in Nonaqueous Lithium–Oxygen Battery Electrochemistry". In: *The Journal of Physical Chemistry Letters* 2.10 (Apr. 2011), pp. 1161–1166. DOI: 10.1021/jz200352v.

[82] B. D. McCloskey et al. "Twin problems of interfacial carbonate formation in nonaqueous Li-O 2 batteries". In: *Journal of Physical Chemistry Letters* 3.8 (2012), pp. 997–1001. ISSN: 19487185. DOI: 10.1021/jz300243r.

[83] Sara E. Renfrew and Bryan D. McCloskey. "Quantification of Surface Oxygen Depletion and Solid Carbonate Evolution on the First Cycle of LiNi0.6Mn0.2Co0.2O2 Electrodes". In: *ACS Applied Energy Materials* 2.5 (2019). Publisher: American Chemical Society Genre: research-article, pp. 3762–3772. ISSN: 25740962. DOI: 10.1021/acsaem.9b00459.

[84] Nika Mahne et al. "Electrochemical Oxidation of Lithium Carbonate Generates Singlet Oxygen". In: *Angewandte Chemie - International Edition* 57.19 (2018). ISBN: 0304-4017, pp. 5529–5533. ISSN: 15213773. DOI: 10.1002/anie.201802277.

[85] Simon Franz Lux et al. "HF formation in LiPF6-based organic carbonate electrolytes". In: *ECS Electrochemistry Letters* 2.12 (2013), pp. 121–123. ISSN: 21628726. DOI: 10.1149/2.005312eel.

[86] Jihyun Hong et al. "Review—Lithium-Excess Layered Cathodes for Lithium Rechargeable Batteries". In: *Journal of The Electrochemical Society* 162.14 (2015), A2447–A2467. ISSN: 0013-4651. DOI: 10.1149/2.0071514jes.

[87] Satishkumar B. Chikkannanavar, Dawn M. Bernardi, and Lingyun Liu. "A review of blended cathode materials for use in Li-ion batteries". In: *Journal of Power Sources* 248 (2014). Publisher: Elsevier B.V, pp. 91–100. ISSN: 03787753. DOI: 10.1016/j.jpowsour.2013.09.052. URL: http://dx.doi.org/10.1016/j.jpowsour.2013.09.052.

[88] Bin Ouyang et al. "Effect of Fluorination on Lithium Transport and Short-Range Order in Disordered-Rocksalt-Type Lithium-Ion Battery Cathodes". In: *Advanced Energy Materials* 10.10 (2020), pp. 1–11. ISSN: 16146840. DOI: 10.1002/aenm.201903240.

[89] Aziz Abdellahi et al. "Understanding the Effect of Cation Disorder on the Voltage Profile of Lithium Transition-Metal Oxides". In: *Chemistry of Materials* 28.15 (Aug. 2016). Publisher: American Chemical Society, pp. 5373–5383. ISSN: 15205002. DOI: 10.1021/acs.chemmater.6b01438. URL: https://doi.org/10.1021/acs.chemmater.6b01438.

[90] Raphaële J Clément et al. "Short-Range Order and Unusual Modes of Nickel Redox in a Fluorine-Substituted Disordered Rocksalt Oxide Lithium-Ion Cathode". In: *Chemistry of Materials* 30.19 (Oct. 2018). Publisher: American Chemical Society, pp. 6945–6956. ISSN: 0897-4756. DOI: 10.1021/acs.chemmater.8b03794. URL: https://doi.org/10.1021/acs.chemmater.8b03794.

[91] William D Richards et al. "Fluorination of Lithium-Excess Transition Metal Oxide Cathode Materials". In: *Advanced Energy Materials* 8.5 (Feb. 2018). Publisher: John Wiley & Sons, Ltd, p. 1701533. ISSN: 1614-6832. DOI: 10.1002/aenm.201701533. URL: https://doi.org/10.1002/aenm.201701533.

[92] M Ménétrier et al. "NMR evidence of LiF coating rather than fluorine substitution in Li(Ni0.425Mn0.425Co0.15)O2". In: *Journal of Solid State Chemistry* 181.12 (2008), pp. 3303–3307. ISSN: 0022-4596. DOI: https://doi.org/10.1016/j.jssc.2008.09.002. URL: https://www.sciencedirect.com/science/article/pii/S0022459608004751.

[93] Linze Li et al. "Fluorination-Enhanced Surface Stability of Cation-Disordered Rocksalt Cathodes for Li-Ion Batteries". In: *Advanced Functional Materials* n/a.n/a (Apr. 2021). Publisher: John Wiley & Sons, Ltd, p. 2101888. ISSN: 1616-301X. DOI: https://doi.org/10.1002/adfm.202101888. URL: https://doi.org/10.1002/adfm.202101888.

[94] Zhengyan Lun et al. "Design Principles for High-Capacity Mn-Based Cation-Disordered Rocksalt Cathodes". In: *Chem* 6.1 (2020), pp. 153–168. ISSN: 2451-9294. DOI: https://doi.org/10.1016/j.chempr.2019.10.001. URL: http://www.sciencedirect.com/science/article/pii/S2451929419304322.

[95] Young-Kyu Han, Jaeik Yoo, and Taeeun Yim. "Distinct Reaction Characteristics of Electrolyte Additives for High-Voltage Lithium-Ion Batteries: Tris(trimethylsilyl) Phosphite, Borate, and Phosphate". In: *Electrochimica Acta* 215 (2016), pp. 455–465. ISSN: 0013-4686. DOI: https://doi.org/10.1016/j.electacta.2016.08.131. URL: https://www.sciencedirect.com/science/article/pii/S0013468616318667.

[96] Ivan Hung et al. "Isotropic High Field NMR Spectra of Li-Ion Battery Materials with Anisotropy ¿1 MHz". In: *Journal of the American Chemical Society* 134.4 (Feb. 2012). Publisher: American Chemical Society, pp. 1898–1901. ISSN: 0002-7863. DOI: 10.1021/ja209600m. URL: https://doi.org/10.1021/ja209600m.

[97] Z Gan and R R Ernst. "An Improved 2D Magic-Angle-Turning Pulse Sequence for the Measurement of Chemical-Shift Anisotropy." eng. In: *Journal of magnetic resonance. Series A* 123.1 (Nov. 1996). Place: United States, pp. 140–143. ISSN: 1064-1858 (Print). DOI: 10.1006/jmra.1996.0227.

[98] Dominique Massiot et al. "Modelling one- and two-dimensional solid-state NMR spectra". In: *Magnetic Resonance in Chemistry* 40.1 (Jan. 2002). Publisher: John Wiley & Sons, Ltd, pp. 70–76. ISSN: 0749-1581. DOI: https://doi.org/10.1002/mrc.984. URL: https://doi.org/10.1002/mrc.984.

[99] Jinhyuk Lee et al. "Determining the Criticality of Li-Excess for Disordered-Rocksalt Li-Ion Battery Cathodes". In: *Advanced Energy Materials* 11.24 (June 2021). Publisher: John Wiley & Sons, Ltd, p. 2100204. ISSN: 1614-6832. DOI: https://doi.org/10.1002/aenm.202100204. URL: https://doi.org/10.1002/aenm.202100204.

[100] Xuelong Wang et al. "The Role of Electron Localization in Covalency and Electrochemical Properties of Lithium-Ion Battery Cathode Materials". In: *Advanced Functional Materials* 31.2 (Jan. 2021). Publisher: John Wiley & Sons, Ltd, p. 2001633. ISSN: 1616-301X. DOI: https://doi.org/10.1002/adfm.202001633. URL: https://doi.org/10.1002/adfm.202001633.

[101] Yang Yu et al. "Coupled LiPF6 Decomposition and Carbonate Dehydrogenation Enhanced by Highly Covalent Metal Oxides in High-Energy Li-Ion Batteries". In: *Journal of Physical Chemistry C* 122.48 (Oct. 2018). Publisher: American Chemical Society, pp. 27368–27382. ISSN: 19327455. DOI: 10.1021/acs.jpcc.8b07848.

[102] Anna T.S. Freiberg et al. "Li2CO3 decomposition in Li-ion batteries induced by the electrochemical oxidation of the electrolyte and of electrolyte impurities". In: *Electrochimica Acta* 346 (2020). Publisher: Elsevier Ltd, p. 136271. ISSN: 00134686. DOI: 10.1016/j.electacta.2020.136271. URL: https://doi.org/10.1016/j.electacta.2020.136271.

[103] Yirui Zhang et al. "Revealing electrolyte oxidation via carbonate dehydrogenation on Ni-based oxides in Li-ion batteries by in situ Fourier transform infrared spectroscopy". In: *Energy & Environmental Science* 13.1 (2020). Publisher: The Royal Society of Chemistry, pp. 183–199. ISSN: 1754-5692. DOI: 10.1039/C9EE02543J. URL: http://dx.doi.org/10.1039/C9EE02543J.

[104] Chun Zhan et al. "Dissolution, migration, and deposition of transition metal ions in Li-ion batteries exemplified by Mn-based cathodes – a critical review". In: *Energy & Environmental Science* 11.2 (2018). Publisher: The Royal Society of Chemistry, pp. 243–257. ISSN: 1754-5692. DOI: 10.1039/C7EE03122J. URL: http://dx.doi.org/10.1039/C7EE03122J.

[105] Nan Xin et al. "Solubilities of six lithium salts in five non-aqueous solvents and in a few of their binary mixtures". In: *Fluid Phase Equilibria* 461 (2018), pp. 1–7. ISSN: 0378-3812. DOI: https://doi.org/10.1016/j.fluid.2017.12.034. URL: https://www.sciencedirect.com/science/article/pii/S0378381217305186.

[106] Takayuki Aoshima et al. "Mechanisms of manganese spinels dissolution and capacity fade at high temperature". In: *Journal of Power Sources* 97-98 (2001), pp. 377–380. ISSN: 0378-7753. DOI: https://doi.org/10.1016/S0378-7753(01)00551-1. URL: https://www.sciencedirect.com/science/article/pii/S0378775301005511.

[107] Dong H Jang and Seung M Oh. "Electrolyte Effects on Spinel Dissolution and Cathodic Capacity Losses in 4 V Li / Li x Mn2 O 4 Rechargeable Cells". In: *Journal of The Electrochemical Society* 144.10 (1997). Publisher: The Electrochemical Society, pp. 3342–3348. ISSN: 0013-4651. DOI: 10.1149/1.1838016. URL: http://dx.doi.org/10.1149/1.1838016.

[108] Dong H Jang, Young J Shin, and Seung M Oh. "Dissolution of Spinel Oxides and Capacity Losses in 4 V Li / Li x Mn2 O 4 Cells". In: *Journal of The Electrochemical Society* 143.7 (1996). Publisher: The Electrochemical Society, pp. 2204–2211. ISSN: 0013-4651. DOI: 10.1149/1.1836981. URL: http://dx.doi.org/10.1149/1.1836981.

[109] K. Edström, T. Gustafsson, and J. O. Thomas. "The cathode-electrolyte interface in the Li-ion battery". In: *Electrochimica Acta* 50.2-3 SPEC. ISS. (2004), pp. 397–403. ISSN: 00134686. DOI: 10.1016/j.electacta.2004.03.049.

[110] Won Jong Lee et al. "Depth profile studies on nickel rich cathode material surfaces after cycling with an electrolyte containing vinylene carbonate at elevated temperature". In: *Physical Chemistry Chemical Physics* 16.32 (2014). Publisher: The Royal Society of Chemistry, pp. 17062–17071. ISSN: 1463-9076. DOI: 10.1039/C4CP02075H. URL: http://dx.doi.org/10.1039/C4CP02075H.

[111] Ting Liu et al. "Surface phenomena of high energy Li(Ni1/3Co1/3Mn1/3)O2/graphite cells at high temperature and high cutoff voltages". In: *Journal of Power Sources* 269 (2014), pp. 920–926. ISSN: 0378-7753. DOI: https://doi.org/10.1016/j.jpowsour.2014.07.051. URL: https://www.sciencedirect.com/science/article/pii/S0378775314010957.

[112] Judith Alvarado et al. "A carbonate-free, sulfone-based electrolyte for high-voltage Li-ion batteries". In: *Materials Today* 21.4 (2018), pp. 341–353. ISSN: 1369-7021. DOI: https://doi.org/10.1016/j.mattod.2018.02.005. URL: http://www.sciencedirect.com/science/article/pii/S1369702118301731.

[113] Bharathy S Parimalam and Brett L Lucht. "Reduction Reactions of Electrolyte Salts for Lithium Ion Batteries: LiPF6, LiBF4, LiDFOB, LiBOB, and LiTFSI". In: *Journal of The Electrochemical Society* 165.2 (2018). Publisher: The Electrochemical Society, A251–A255. ISSN: 0013-4651. DOI: 10.1149/2.0901802jes. URL: http://dx.doi.org/10.1149/2.0901802jes.

[114] Peter Holstein, Robin K Harris, and Barry J Say. "Solid-state 19F NMR investigation of poly(vinylidene fluoride) with high-power proton decoupling". In: *Solid State Nuclear Magnetic Resonance* 8.4 (1997), pp. 201–206. ISSN: 0926-2040. DOI: https://doi.org/10.1016/S0926-2040(97)00014-3. URL: https://www.sciencedirect.com/science/article/pii/S0926204097000143.

[115] Lori A Kaufman and Bryan D McCloskey. "Surface Lithium Carbonate Influences Electrolyte Degradation via Reactive Oxygen Attack in Lithium-Excess Cathode Materials". In: *Chemistry of Materials* 33.11 (June 2021). Publisher: American Chemical Society, pp. 4170–4176. ISSN: 0897-4756. DOI: 10.1021/acs.chemmater.1c00935. URL: https://doi.org/10.1021/acs.chemmater.1c00935.

[116] Sara E Renfrew and Bryan D McCloskey. "The Role of Electrolyte in the First-Cycle Transformations of LiNi0.6Mn0.2Co0.2O2". In: *Journal of The Electrochemical Society* 166.13 (2019). Publisher: The Electrochemical Society, A2762–A2768. ISSN: 0013-4651. DOI: 10.1149/2.1561912jes. URL: http://dx.doi.org/10.1149/2.1561912jes.

[117] Wesley M. Dose et al. "Electrolyte Reactivity at the Charged Ni-Rich Cathode Interface and Degradation in Li-Ion Batteries". In: *ACS Applied Materials & Interfaces* 14.11 (Mar. 2022). Publisher: American Chemical Society, pp. 13206–13222. ISSN: 1944-8244. DOI: 10.1021/acsami.1c22812. URL: https://doi.org/10.1021/acsami.1c22812.